University of Wollongong

Research Online

University of Wollongong Thesis Collection 1954-2016

University of Wollongong Thesis Collections

2015

A study of grain size effect on mechanical behaviour, fracture mechanism, texture evolution and springback in microforming process

Zhi Fang
University of Wollongong

Follow this and additional works at: https://ro.uow.edu.au/theses

University of Wollongong

Copyright Warning

You may print or download ONE copy of this document for the purpose of your own research or study. The University does not authorise you to copy, communicate or otherwise make available electronically to any other person any copyright material contained on this site.

You are reminded of the following: This work is copyright. Apart from any use permitted under the Copyright Act 1968, no part of this work may be reproduced by any process, nor may any other exclusive right be exercised, without the permission of the author. Copyright owners are entitled to take legal action against persons who infringe their copyright. A reproduction of material that is protected by copyright may be a copyright infringement. A court may impose penalties and award damages in relation to offences and infringements relating to copyright material. Higher penalties may apply, and higher damages may be awarded, for offences and infringements involving the conversion of material into digital or electronic form.

Unless otherwise indicated, the views expressed in this thesis are those of the author and do not necessarily represent the views of the University of Wollongong.

Recommended Citation

Fang, Zhi, A study of grain size effect on mechanical behaviour, fracture mechanism, texture evolution and springback in microforming process, Doctor of Philosophy thesis, School of Mechanical, Materials and Mechatronics Engineering, University of Wollongong, 2015. https://ro.uow.edu.au/theses/4380

Research Online is the open access institutional repository for the University of Wollongong. For further information contact the UOW Library: research-pubs@uow.edu.au

A STUDY OF GRAIN SIZE EFFECT ON MECHANICAL BEHAVIOUR, FRACTURE MECHANISM, TEXTURE EVOLUTION AND SPRINGBACK IN MICROFORMING PROCESS

A thesis submitted in fulfilment of the requirements

for the award of the degree of

Doctor of Philosophy

from

University of Wollongong

By

Zhi Fang

B. Eng., M. Eng.

School of Mechanical, Materials and Mechatronics Engineering

Faculty of Engineering and Information Sciences

March, 2015

Declaration

I, Zhi Fang, declare that this thesis, submitted in fulfilment of the requirements for award of Doctor of Philosophy, in the School of Mechanical, Materials and Mechatronics Engineering, University of Wollongong, Australia, is wholly my own work unless otherwise referenced or acknowledged. The document has not been submitted for qualifications at any other academic institution.

Zhi Fang

Signature:

March, 2015

Acknowledgement

I wish to express my sincere appreciation and gratitude to my supervisor, Professor Zhengyi Jiang, for the opportunity he offered, and for his valuable guidance, support, encouragement and friendship during my PhD candidature, especially during the period when I had my first child. It has been a great pleasure working with him.

I am deeply grateful to Dr. Dongbin Wei for their strong guidance, valuable discussion and close supervision.

I also wish to thank the staff and students within the Faculty of Engineering and Information Sciences who gave me enormous help and assistance.

I would like to appreciate the China Scholarship Council and the University of Wollongong for offering the scholarships to continue my study.

Last but not least, my warm appreciation and respect go to my wife Yan Ma, my son Dylan Fang, my parents and parents-in-laws for their sacrifice, love, patience, understanding and selfless dedication. They are all to me. Cheers for everything!

Abstract

Size effects play a significant role in microforming process, and any dimensional change on microstructure or specimens can have a great impact on materials' mechanical properties. In this research, the grain size effect on deformation behaviour, fracture and grain orientation of phosphor bronze foil are investigated in the form of the ratio of materials' thickness (T) to average grain size (D) by micro tensile tests. The ratio is designed to be greater than, less than and equal to 1 respectively. The results show that the amount of plastic deformation decreases with the decrease of the ratio T/D, which indicates the grain size plays a significant role in the deformation process and grain deformation modes differ when the ratio changes. It is also found that their fractograph reflect different features in terms of micro-dimples and cleavage planes, further demonstrating that when $T/D>1$, the material has a tendency to experience ductile fracture, while the material would like to conduct brittle fracture when $T/D<1$. So the ratio T/D can be regards as the divide of ductile fracture and brittle fracture when it is approximately equal to 1. Additionally, for $T/D<1$, a new constitutive model is proposed based on the classic composite model. The model's results are compared with the experimental ones and the efficiency of the developed models is verified.

In addition, grain size effects on texture evolution in annealing and micro V-bending process of phosphor bronze foil (face centred cubic structure) are investigated by

electron back-scattering diffraction (EBSD). Texture measurement results show that the intensities of α-fibre components vary with the ratio *T*/*D* which is achieved by different annealing schedules. The intensity of the A orientation increases with the increase of *T*/*D* value, while the intensities of the Goss and Brass components decrease. It is also found out that during micro V-bending process the grain rotation is correlative with the ratio *T*/*D*. When *T*/*D*>1, grains in the specimen are more likely to rotate due to the grain coordination deformation. Oppositely, grain orientations in the material are more stable because of the restriction from the material's lower and upper boundaries when *T*/*D* value is less than 1. Moreover, the crystallographic planes {110} are found increasingly stable during micro V-bending process with the decrease of *T*/*D*, and the corresponding reasons have been discussed.

The microstructure of materials plays a dominant role in their deformation behaviours, and has a great impact on the quality of the corresponding products. In general, the microstructural properties of polycrystalline metals include grain size, grain orientation, micro texture and density of dislocation etc. However, it is rare to find an appropriate method to adopt 'grain size' into numerical simulation for microforming study.

This research thoroughly illustrates the implementation of like-grain size structure: Voronoi tessellation and grain heterogeneity in the commercial FE software: ABAQUS with the help of another two sets of software: MATLAB and Python. Therefore, a finite element (FE) model of the micro V-bending has been established where the specimen's

microstructure is represented by 3D Voronoi tessellations to study springback phenomenon which is inevitable during metal forming process, and can cause unpredicted dimensional error. Since the previous research found that the springback value in microforming was difficult to be assessed as the size of tools and specimens downsize hundreds even thousands times, this research focuses on improving the prediction accuracy of springback during micro V-bending. With the consideration of the grain heterogeneity, each Voronoi cell has been employed with different grain mechanical properties based on micro tensile test results. Corresponding micro V-bending tests have been carried out, and a good agreement between the experimental and simulation results indicates that the developed FE model can predict springback in micro V-bending effectively.

This study provides a better understanding of grain size effect in micro tensile test and micro V-bending in terms of mechanical behaviour, fracture mechanism, texture evolution and springback. Furthermore, springback phenomenon is intensely investigated by FE simulation. These corresponding results can be utilised either as references to other research on microforming or information for micro parts manufacturing.

List of Figures

List of Tables

List of Abbreviations and Symbols

1. Abbreviations

2D	two dimensional
3D	three dimensional
CAE	computer aided engineering
CFD	computational fluid dynamics
CPFEM	crystal plasticity finite element method
EBSD	electron backscattered diffraction
f.c.c	face centred cubic
FE	finite element
FEM	finite element method
ND	normal direction
OM	optical microscope
SEM	scanning electron microscope
TD	transverse direction

2. Symbols

E	Young's modulus
E_{TAN}	tangent modulus
T	thickness
D	grain size
A_G	areal fraction of grain interior
A_{GB}	areal fraction of grain boundary
σ_{fG}	flow stress of grain interior
σ_{fGB}	flow stress of grain boundary
σ_y	material's flow stress
t	grain boundary thickness

Table of Contents

Chapter 1 Introduction

With the widespread application of metal micro-parts, their corresponding production technology-microforming has been paid close attention by many scholars. Consequently, the development of this cutting-edge technology has been greatly prompted. The popularity of microforming can be attributed to its outstanding characters, such as bulk production, high efficiency, high accuracy, short cycle, and low cost. Although the advance of microforming technology can benefit from the relatively mature scientific background of conventional macroforming, there is one issue that microforming cannot mechanically copy from macroforming, and that also clearly distinguish the former from the latter. This is so called “size effects”.

1.1 Size effects

1.1.1 Definition

In the end of the 19^{th} century, size effects were proposed to detect and describe for upscaling purposes. However, it is understood that size effects play a significant role in miniaturisation which is very frequent in microtechnology and nanotechnology nowadays. Generally speaking, size effects can be regarded as those deviations from the expected results which are obtained when the dimension of a specimen is changed.

However, Vollertsen [1] modified this statement in a more precise way: size effects are deviations from intensive or proportional extrapolated extensive values of a process which occur, when scaling the geometrical dimensions. This definition is applicable to a wide range of processes, as it not only predicts the influence that size effects could cause, but also takes the possibility that the dimensions of a wider range items, such as forces, specimen and tools could change into consideration.

Although this definition looks more sophisticated than “size effects” these two words, size effects in this thesis are mainly regarded to specimen size and grain size. Figure 1-1 illustrates how size effects work when the size of specimen is scaling down. From the figure, we can clearly observe that although average grain size remains constant, the miniaturisation of specimen’ dimension leads to the change of the ratio of volume grains and surface grains, which will result in a strong impact on the specimen’s mechanical property.

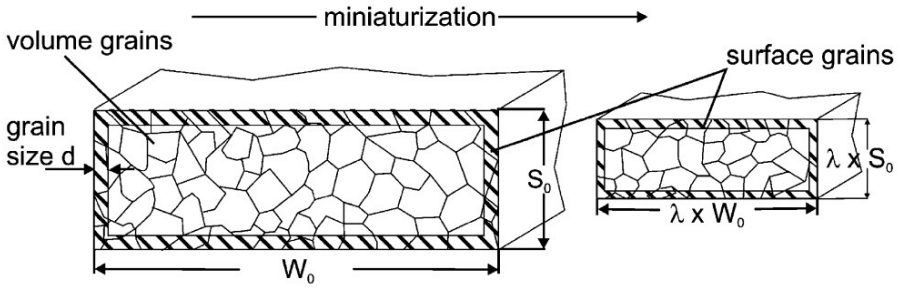

Figure 1-1 Relation of surface grains to volume grains [2].

1.1.2 Types of size effects

Vollertsen [1] also suggested that size effects can be categorised into three main parts in a systematic order. They are density size effects, shape size effects and microstructure size effects respectively illustrated in Figure 1-2. Density size effect normally occurs when the absolute value or internal value of a certain feature (i.e. the density) is a constant and independent on the size of the objective. Besides, if the shape of an objective is unchanged while the size of it does, the value of interest can happen to change. Shape size effect is applicable to describe this phenomenon and relationship. Moreover, the last size effect, which is named microstructure size effect, contains two conditions: one is the fact that the microstructural features are not scaled down with the macroscopic size of the objective reducing scale, and the other is that the macroscopic size of the objective remains while the characters of microstructure (i.e. grain size) experience changes.

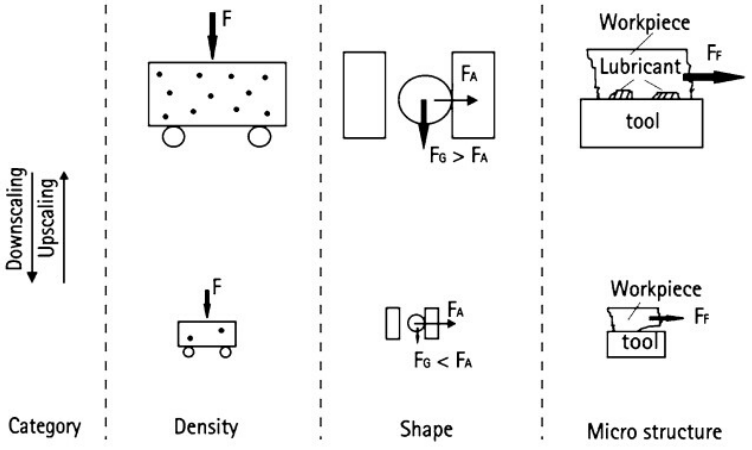

Figure 1-2 Schematic representations of the three main groups of size effects. F force, F_A adhesion force, F_F friction force, F_G gravity [1].

This PhD study concentrates on the third microstructure size effect, to be more exact, it mainly focuses on the research about the relationship of specimen's macroscopic geometry and its microscopic grain size and its effect on mechanical properties, deformation behaviour, texture evolution and springback thorough micro tensile tests and micro V-bending.

1.2 Significance of this research

According to the definition and the category of size effects, a better understanding on microforming process can be obtained: not only the external or internal geometrical changes are in the range of our consideration but also their corresponding influences which are size effects an extremely significant factor that cannot be ignored. These factors are the main roots of that the conventional and classical plastic theory cannot be applied directly on microforming process, and causing the inhomogeneous deformation phenomenon as well. Due to size effects, the experimental or numerical results from microforming become too uncertain to be accurately predicted and compensated. Therefore, it is essential to find out the influence of size effects on a variety of processing in microforming and the deep reasons behind their surface phenomena. On the whole, there are three points while either the current research has not conducted with or has done merely basic studies which will be discussed in detail in Chapter 2 which needs to be investigated further. These bullets are as follows:

(1) The influence of grain size effect on plastic deformation and fracture behaviour. Normally, the deformation of metal material will undergo elastic deformation, plastic deformation, and then fracture. Therefore when grain size effect works on specimens, whether materials' deformation behaviour and fracture behaviour will be the same as that in macroscopic deformation or have its own deformation features, and deformation law is worth investigating.

(2) The influence of grain size effect on texture evolution in mechanical processing and heat treatment. Texture is becoming a very popular research topic in recent years due to the rapid development of its corresponding detecting techniques and equipment. Plus, an increasing number of studies have found that grain orientation is closely correlated with materials' mechanical properties. So it is very important to make good use of the available technologies and scientific achievements to study the relationship between texture and microforming.

(3) An appropriated method to conduct microforming numerical simulation and obtain reliable outcomes. The wide application of finite element (FE) models in conventional industry is not applicable because in microforming specimens cannot be regarded as homogeneous materials and the grain heterogeneity should be taken into consideration. So proposing a proper modelling approach to satisfy the demand for microforming numerical simulation is necessary.

As mentioned above, it is not difficult to see that these points need to be intensively studied experimentally and numerically. Therefore, the role that grain size effect plays in microforming can be better understood, and its application can be better utilised.

1.3 Outline of the thesis

This thesis is composed by eight chapters and a bibliography of the cited references. The contents of each chapter are as listed below. In Chapter 1, the research target and the main meaning of study are stated.

Chapter 2 reviews previous research that is correlated with the current research work. It includes a variety of studies involving most of similar works that can reflect the relationship between grain size effect and various material property parameters, such as formability, inhomogeneity, mechanical behaviour and springback compensation. Numerical simulation is a powerful tool in the studies of microforming, and the relevant research is also reviewed in detail in this chapter.

In Chapter 3, experimental instruments and numerical software for the whole research objectives involved in this PhD program are illustrated. The matching methodologies are also introduced.

Chapter 4 presents the specimen materials, the equipment and devices used in micro tensile tests. The experiments comprise annealing, micro tensile tests and SEM observation. After the above introduction, this chapter primarily discusses the relationship between the ratio *T*/*D* and plastic deformation behaviour and fracture behaviour.

Chapter 5 delivers the correlation between the ratio *T*/*D* and texture evolution in annealing and micro V-bending. The experiments include micro V-bending and EBSD data acquisition and EBSD data interpretation. At the end of this chapter, the phenomena found in EBSD data analysis are discussed with the consideration of grain size effect.

Chapter 6 introduces the background of Voronoi tessellation and the generation of 2D and 3D Voronoi diagram in MATLAB. Furthermore, their corresponding implementation through Python script language in commercial FE software ABAQUS/CAE is stated in detail.

In Chapter 7, micro tensile tests are conducted to obtain the specimen's grain heterogeneity. The physical micro V-bending outcomes and the results of FE simulation modelled by combining 3D Voronoi diagram and the grain heterogeneity are compared. The good agreement demonstrates the feasibility of setting up the

bending model with Voronoi tessellation, which also provides a reliable approach to predict springback angles in micro V-bending.

Chapter 8 states the conclusions of the current study and recommendations for future work. This chapter involves the brief summary of the role that grain size effect plays in the above investigations. Furthermore, studying the relationship between grain orientation and springback, the optimisation of Voronoi tessellations geometrical features and applying crystal plasticity finite element method (CPFEM) are recommended for future work.

Chapter 2 Literature review

In this chapter, a detailed analysis of selected aspects of intensive literatures which are concerned with size effects, especially grain size effect, in microforming processes will be presented to assess the possible mechanisms and the important factors behind the phenomena in microforming. This chapter begins with the brief introduction of microforming and how size effects work in it. The second part introduces the impact of size effects on deformation behaviours and their influence on crystallographic orientation respectively in a variety of microforming technologies. The third part reviews the state of art of the numerical simulation in conventional forming and microforming, on bending particularly. Moreover, experimental methodologies employed to investigate springback phenomenon which is inevitable after bending have also been assessed in this chapter. The last part concludes the literature review and clarifies the research scope in the present study.

2.1 Microforming and size effects

The technology of microforming is attracting increasing attention in contemporary era, especially when metallic parts of submillimetre dimension which are made either from bulk or single sheet material are being required to be produced economically and precisely in large quantities. Considering the general trend towards higher integrated

functional elements and miniaturisation in electronic and micromechanical components, the huge demand for such microparts shown in Figure 2-1 is evident [3]. However, most of these parts are still manufactured by turning and milling such old-fashioned processing methods, and the reason for this is the knowledge of metal forming technology cannot simply downsize to the microscopic world because materials and processes are subjected to a particular phenomenon: it is so-called “size effect”.

Figure 2-1 Cold headed microparts [4].

In order to have a complete and in-depth understanding of this special phenomenon, relevant research on this problem has been conducted for nearly 20 years, and its worldwide popularity indicates the significance of this unique size effect featured technology [5]. Fundamental research intend to unveil the essence and mechanism of size effect by performing experiments which are directly scaled down according to the

similarity theory based on the works from Engel and Echstein [6], Pande et al. [7], Zhao et al. [8], Tiesler [9] and Sobis et al. [10]. Engle and Eckstein [6] proposed the surface layer model in which the specimen was divided into two portions: interior part and surface layer, to explain the reduction of flow stress in microforming process and to provide a mechanism principle that can be applied to explain the above microforming phenomena. Figure 2-2 illustrates how the share of surface grains changes with the change of grain size and specimen geometry.

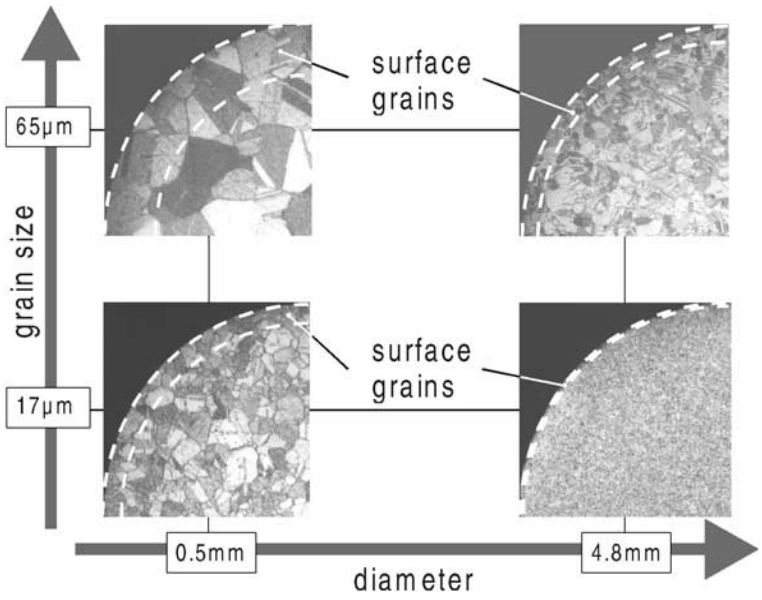

Figure 2-2 Share of surface grains [6].

Additionally, Sobis et al. [10] introduced a model of open and close lubricant pockets which also can be named as dynamic and static lubricant pockets to explain frictional

behaviour in microforming. Figures 2-3 and 2-4 illustrate the model and its effect with miniaturisation respectively.

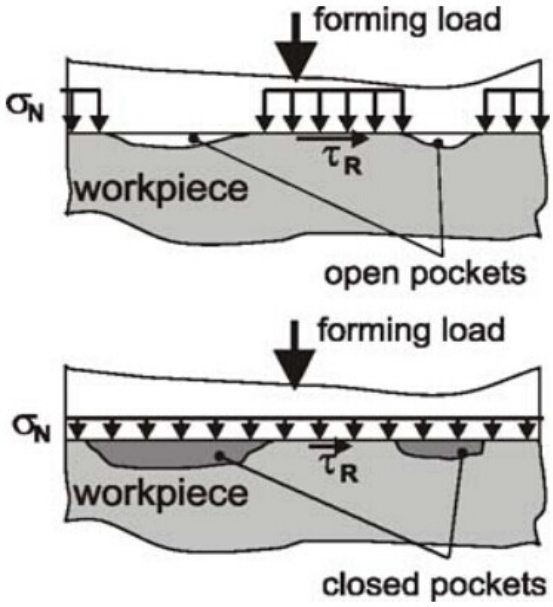

Figure 2-3 Open and closed lubricant pockets (LFT) [10].

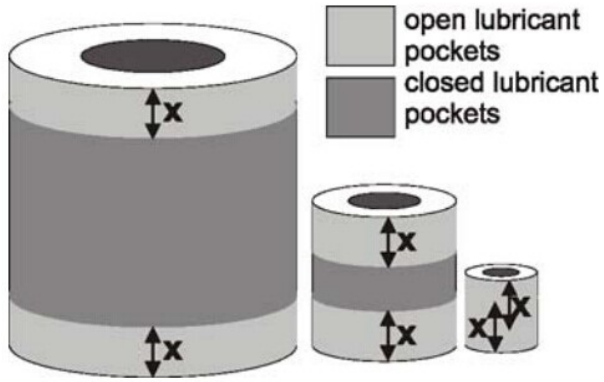

Figure 2-4 Effect of miniaturisation on areas with open and closed lubricant pockets (LFT) [10].

Geiger et al. [11] and Vollertsen et al. [12, 13] published papers with respect to microforming and carried out a comprehensive review of the state of the art of microforming technologies and size effects on material flow properties and on friction. Moreover, people nowadays are transferring their focus mainly on producing high accuracy and high performance microparts. This demands a better understanding on the impact that size effects have in microforming process. Consequently, plenty of meaningful and significant studies have been carried out in this field, and a large number of microforming technologies have been established to achieve this goal.

Sheet metal forming is a mainstream to conduct microforming [12], and unlike the conventional one, sheet metal forming can be classified as a special deformation process in which the thickness of workpiece being much smaller than other dimensions-. Sheet metal forming normally contains stretching, bending, flanging, punching, deep drawing and some other processes. In this thesis, stretching and bending are the processing methods that we chose to conduct our research.

2.2 Size effects on different microforming processes

2.2.1 Size effects in microforming mechanical behaviours

Several researches have been conducted to investigate size effects in micro deformation behaviours and mechanics. Ma et al. [14] researched size effects on fracture behaviour in deep drawing process. Their results illustrated that limit drawing ratio (LDR) is significantly decreased with grain size. Kals and Eckstein [15] investigated size effects in tensile tests and air bending of sheet metals by miniaturisation based on similarity theory. In tensile tests, they found that the flow stress generally decreases with miniaturising the specimen dimensions, and attributed this behaviour to an increasing share of surface grains as shown in Figure 2-5. They also obtained highly accurate bending force by considering the different behaviours and surface and volume grains (Figure 2-6).

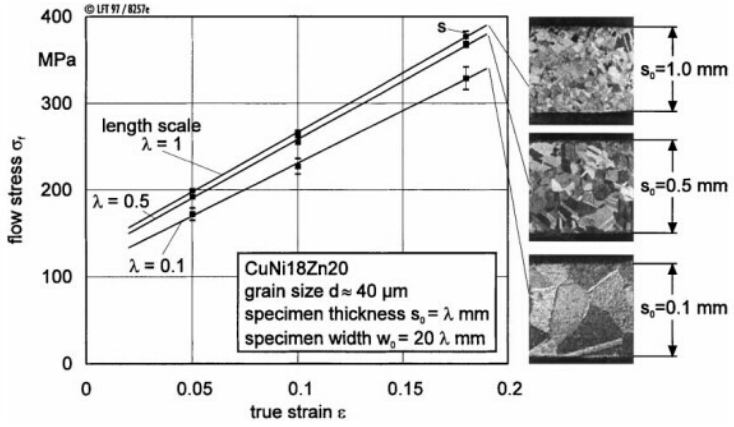

Figure 2-5 Flow curves of CuNi18Zn20 for different values of the length scale λ [15].

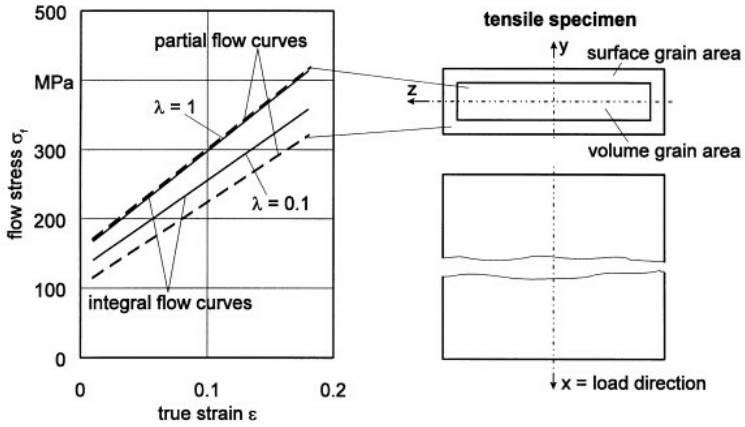

Figure 2-6 Determination of partial flow curves for the surface and the volume grain area. Material: CuNi18Zn20, grain size: $D \approx 25 \mu m$ [15].

Fu et al. [16] studied size effects on fracture behaviour of the annealed copper foils with different thicknesses and grain size by tensile tests displayed in Figure 2-7, and they found that the number of micro-voids as well as the fracture stress and strain decrease with the decrease of T/D as shown in Figure 2-8.

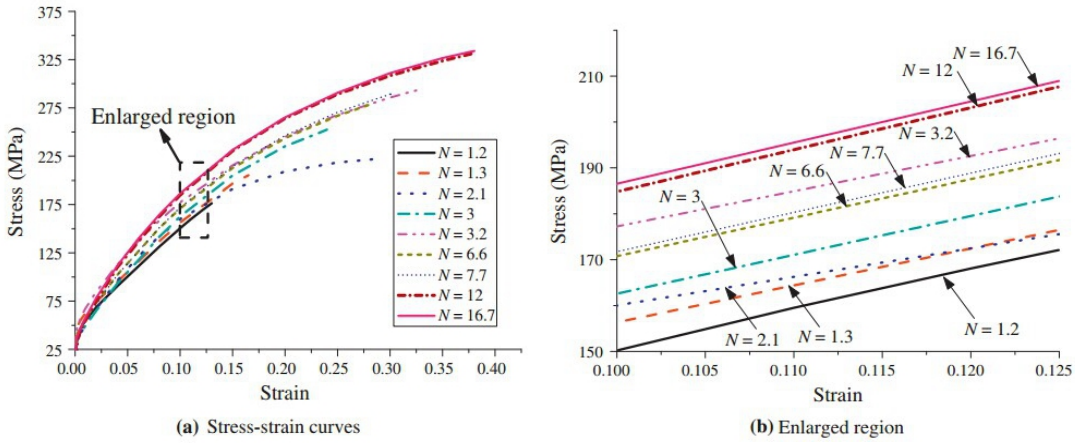

Figure 2-7 Tensile test results: (a) Stress-strain curves, (b) Enlarged region [16].

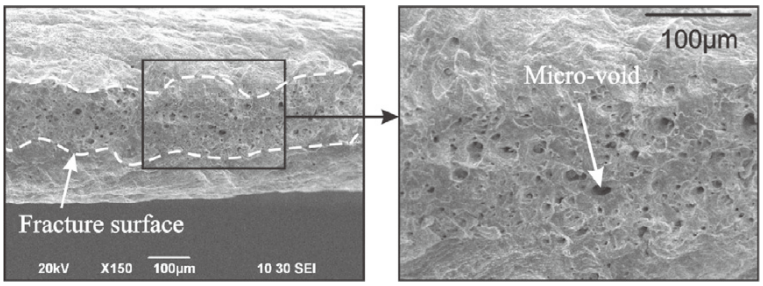

(a) t=600 μm, d=36 μm, N=16.7

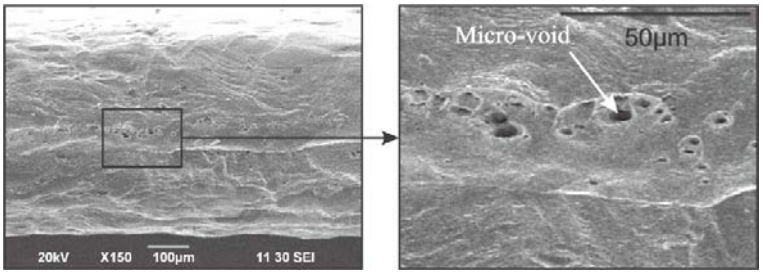

(b) t=600 μm, d=286 μm, N=2.1

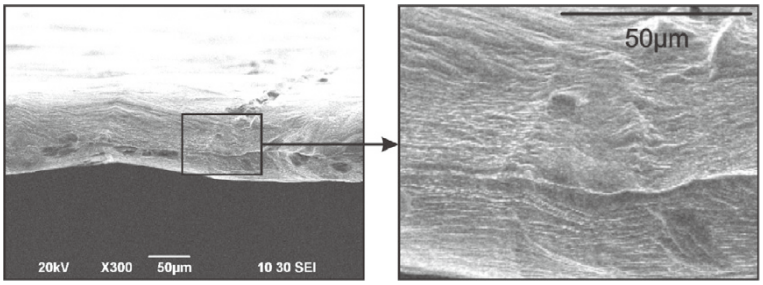

(c) t=100 μm, d=83 μm, N=1.2

Figure 2-8 Fractograph of the tested samples [16].

Further research from Raulea et al. [17] shows that the yield strength is related to the ratio between the grain size and specimen thickness, which is also demonstrated in a planar blanking and bending process. Chan et al. [18] investigated the scatter of grain mechanical properties with micro-compression process and proposed a finite element model with consideration of grain size and the scatter of flow stress, which provided a

basis for understanding and modelling of materials size effects in microforming process. Lu et al. [19] conducted micro cross wedge rolling and its corresponding modelling by implanting Voronoi tessellation algorithm into pre-processor of finite element software ANSYS. In their research, a bilinear isotropic hardening model illustrated in Figure 2-9 is used to achieve the grained heterogeneity.

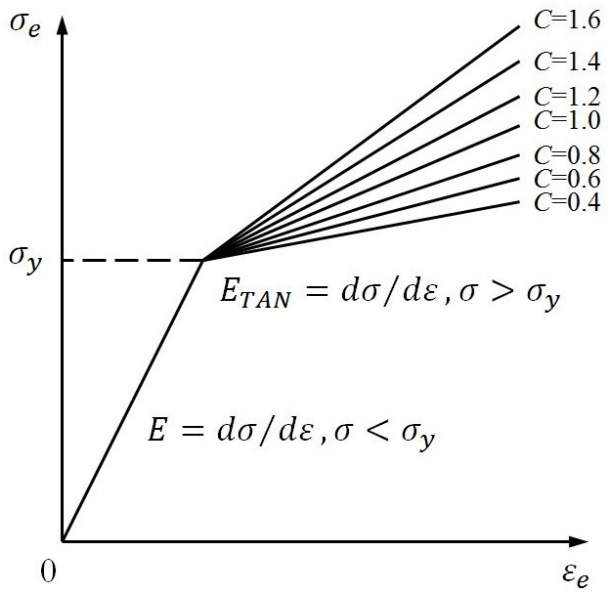

Figure 2-9 Bilinear kinetic hardening [19].

In here, E and E_{TAN} are Young's modulus and tangent modulus of homogenous material respectively. The variation of c value represents material heterogeneity. Moreover, Li et al. [20] carried out micro tensile tests with four different thickness specimens, and each specimen was annealed to obtain fine and coarse grains respectively. The outcomes are shown in Figure 2-10: the specimens with fine grain size exhibit a higher flow stress than those with coarse grain samples and the elongation of foils decreases

with the decrease of foil thickness. For the thinner foils, these fractures were penetrated across the entire foil thickness, but for the thicker foils the micro-cracks are stopped by inner grains. This study analysed that these results are most likely due to the higher strain gradient and more inhomogeneous deformation in thinner foils than those in thicker foils.

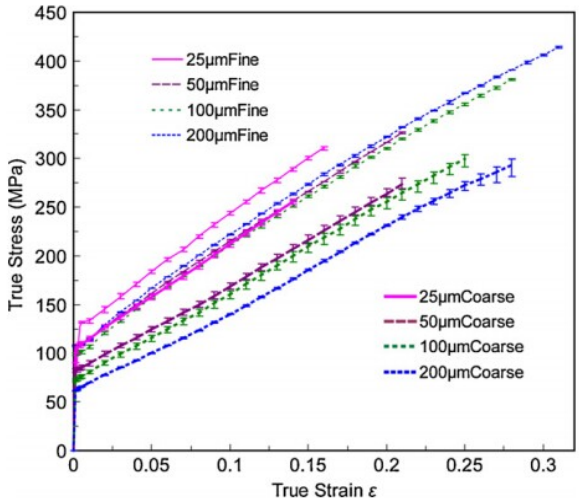

Figure 2-10 Tensile stress–strain curves of CuZn37 foils [20].

Xu et al. [21] studied size effects on deformation behaviour and fracture feature by micro-blanking by different ratios of different blanking clearances (C) to grain size (D): $C/D>1$, $C/D\approx1$ and $C/D<1$, and found that the ultimate shearing strength reaches an extreme value when blanking clearance to grain size ratio is equal to 1. There is a size effects model proposed in their research as illustrated in Figure 2-11.

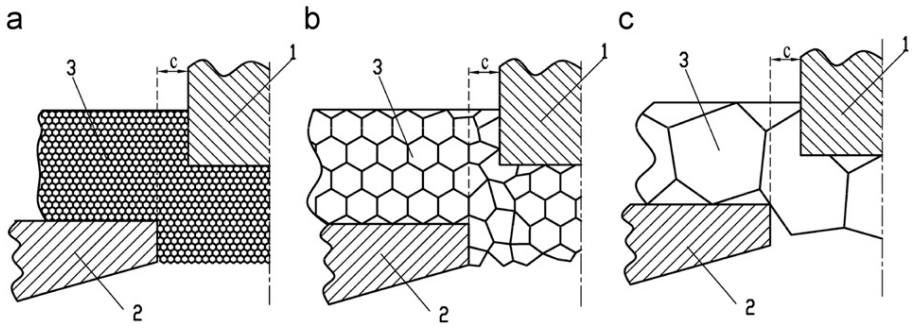

Figure 2-11 Size effect model of grain size in micro-punching: 1-micropunch; 2-microdie; 3-metalfoil. (a) $C/D>1$, (b) $C/D\approx1$ and (c) $C/D<1$ [21].

Liu et al. [22] carried out a serious of three-point bending with copper sheet foils (as displayed in Figure 2-12) to investigate springback behaviour, and they also developed a constitutive model considering the grain boundary strain hardening. Their study found that the springback angles decrease with the increase of the ratio of thickness (T)/average grain size (D).

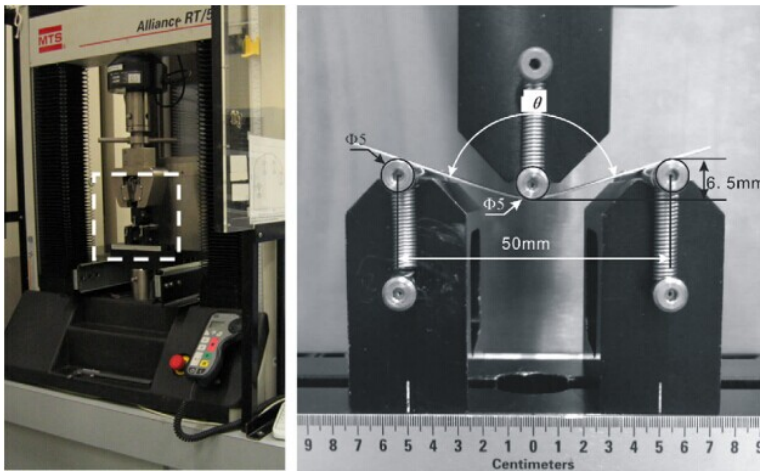

Figure 2-12 Three-point bending test device and tooling [22].

Wang et al. [23] investigated size effects of cavity dimension in coining process. They revealed that the micro-formability decreases with the increase of the ratio between grain sizes and die cavity width. Lau [24] also conducted micro three-point bending focusing on different *T*/*D* ratios. His results are consistent with the outcome from Liu et al. [22], while Diehl et al. [25] drawn a different conclusion through defining a scaling factor *T*/*D*. Hmida et al. [26] conducted the single point incremental forming process of copper foils with different grain sizes, and it was observed the formability decreases with the increase of ratio *T*/*D*.

2.2.2 Size effects on crystallographic orientation in microforming

Prior to this study, several researches have been carried out to investigate the role that size effects play in texture evolution in conventional and microforming process. Park et al. [27] studied the microstructural evolution of magnesium alloy AZ61 during friction stir welding (Figure 2-13), and they found out that tensile properties of the weld of this material (as shown in Figure 2-14) were strongly influenced by grain size and crystallographic orientation distribution which is illustrated in Figure 2-15.

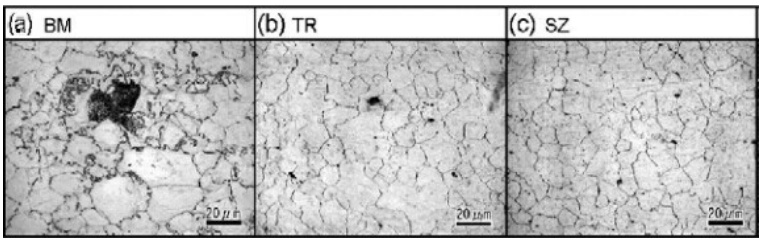

Figure 2-13 Microstructures in FS welded AZ61: (a) the base material region, (b) transition region and (c) stir zone [27].

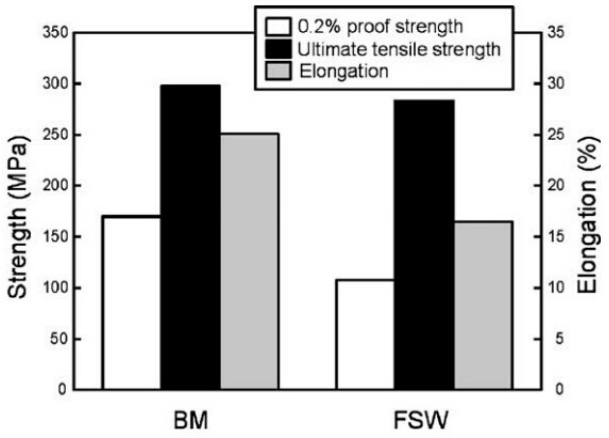

Figure 2-14 Transverse tensile properties of the base material (BM) and the AZ61 Mg FSW joint (FSW) [27].

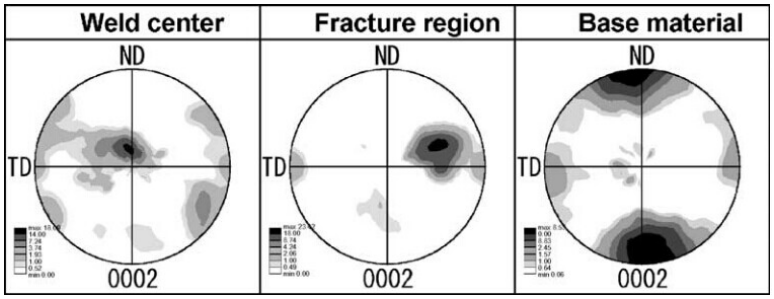

Figure 2-15 (0 0 0 2) pole figures in weld center, fracture region and base material by OIM [27].

Valle et al. [28, 29] conducted equal channel angular pressing (ECAP) and large-strain hot rolling experiment. They concluded that both texture and gran size have a great impact on work hardening as well as ductility, and analysed their contributions on the creep mechanisms in magnesium alloy. As shown in Figures 2-16 and 2-17, Llanes [30]

found a much more pronounced cyclic hardening and high saturation stresses is associated with <111>-<100> fibre texture in coarse-grained copper rather than fine-grained copper.

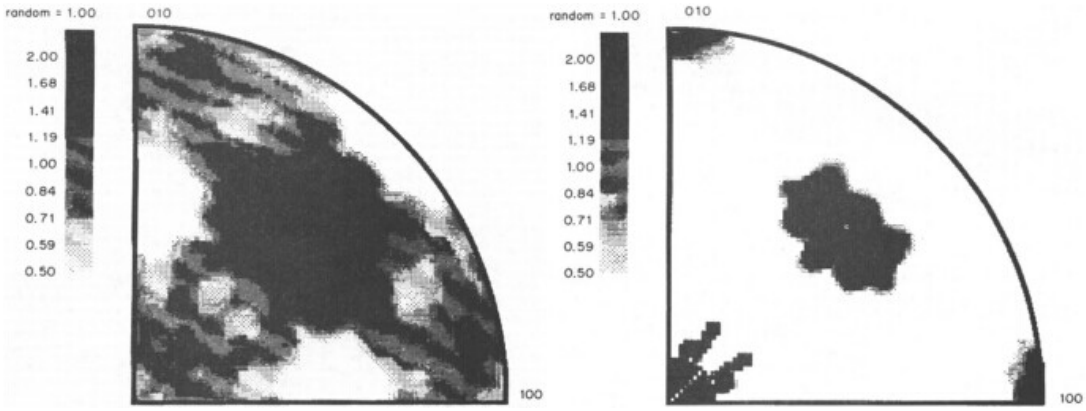

Figure 2-16 The inverse pole figures for small- and large-grained copper [30].

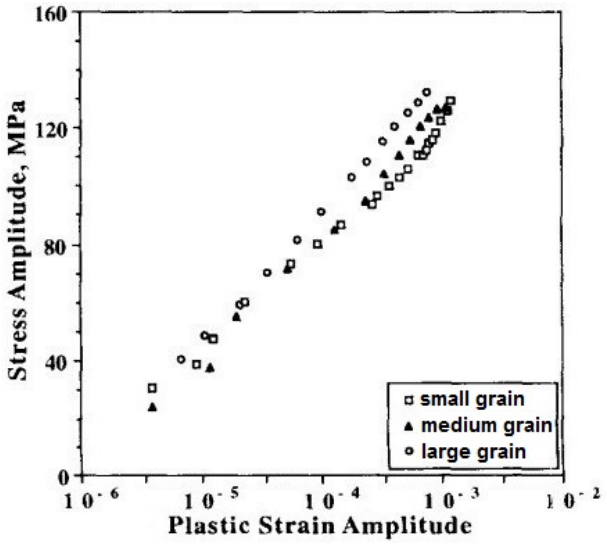

Figure 2-17 Saturation stress strain response (CSSC) of fine- and coarse-grained copper [30].

Janssen et al. [31] studied the mechanical behaviour of pure aluminium samples, and they concluded that the ratio of thickness to grain size can be regarded as an indicator for flow stress when texture in samples are similar (Figures 2-18 and 2-19).

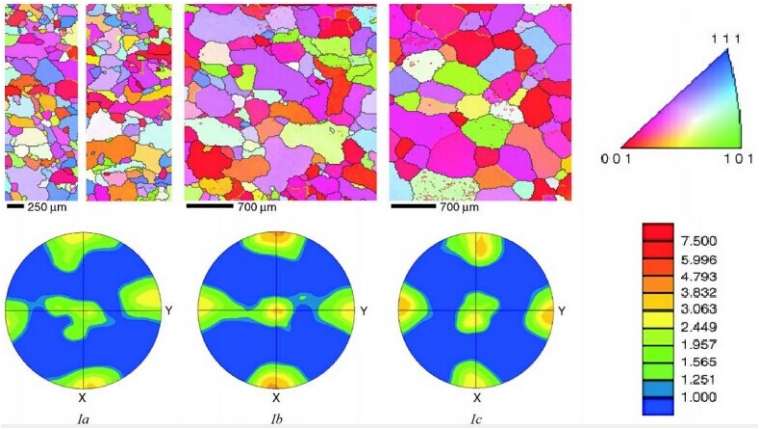

Figure 2-18 Microstructure and {001} pole figures of typical specimens from series I. Grains are coloured according to the indicated inverse pole figure for the tensile direction Y. The indicated colour bar shows the density levels (times random) for the pole figures [31].

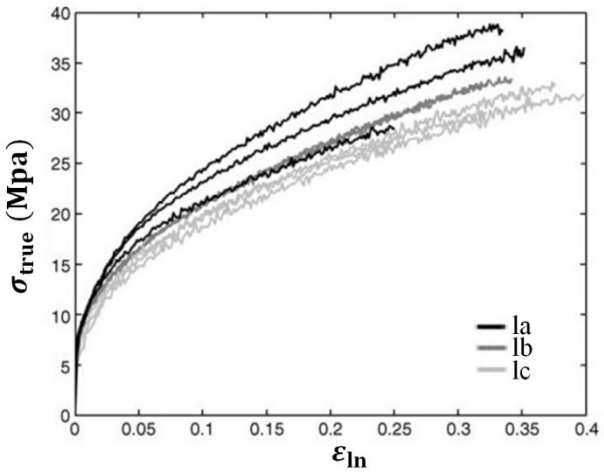

Figure 2-19 Stress–strain curves for all specimens of series I [31].

Hoseini et al. [32] proposed that pure titanium with the (0002) planes to the surface can deliver the highest corrosion resistance regardless of their grain size under ECAP. Yin et al. [33] performed tensile, compressive and ECAP tests on Mg AZ31 alloy to conclude that $\{10\bar{1}2\}$ tensile twinning can cause large yield asymmetry, and grain size 0.8μm or below can eliminate yield asymmetry. Guo et al. [34] also studied the work hardening rate of this materials. Their results indicated that the work hardening rate decreases as grain size decreases as shown in Figure 2-20, but (0002) pole intensity has little effect on work hardening rate displayed in Figure 2-21.

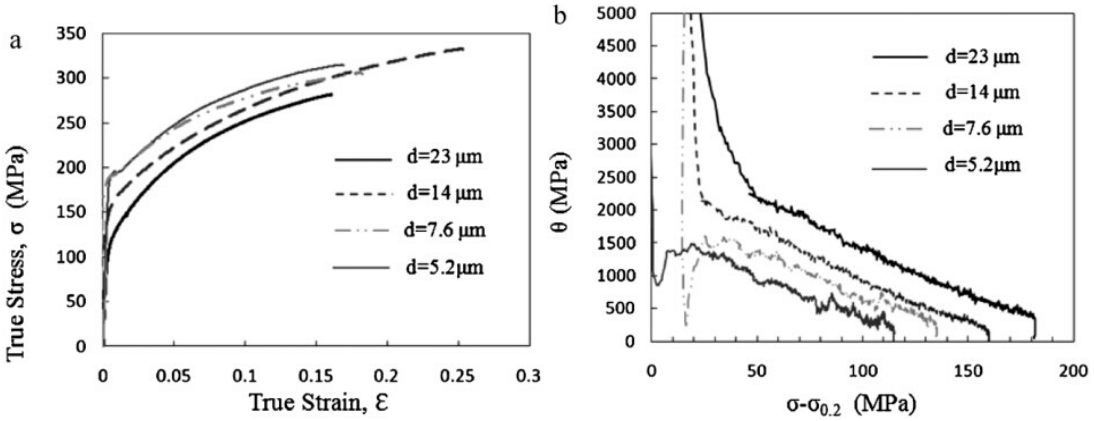

Figure 2-20 Influence of the grain size on the work hardening behaviour of AZ31sheets: (a) true stress–strain curves, (b) θ as a function of $\sigma - \sigma_{0.2}$ for different grain sizes [34].

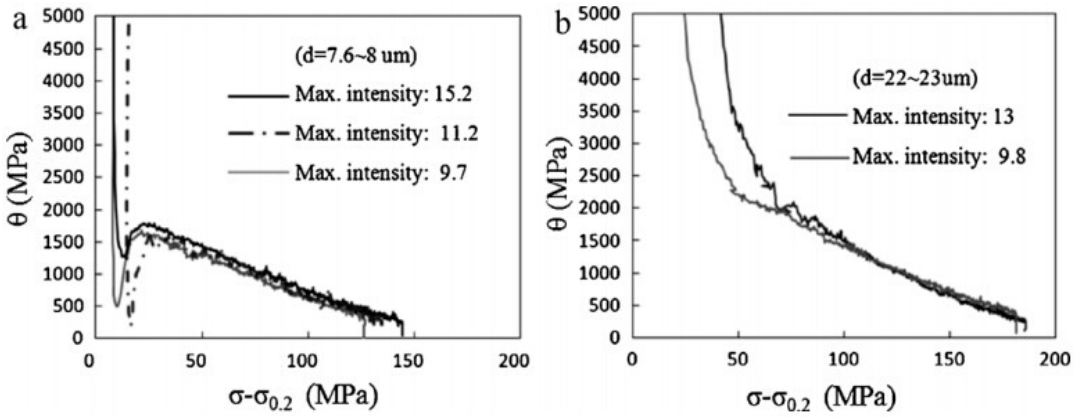

Figure 2-21 Influence of the (0002) pole intensity on the work hardening behaviour of AZ31 for two different grain sizes, (a) 7.6–8μm and (b) 22–23μm [34].

Zhang et al. [35] carried out repeated unidirectional bending process at different temperatures to improve the texture of AZ31B Mg alloy. The results showed in Figures 2-22 and 2-23 that the texture control has more effect on bendability at lower temperature, and Kaneko and Eguchi [36] also verified the decisive effect of texture on bendability.

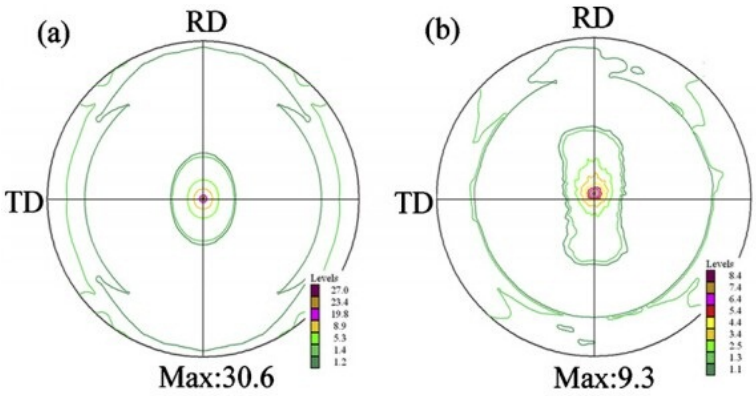

Figure 2-22 {0002} pole figures of (a) the as-received sheet and (b) the RUB processed sheet [35].

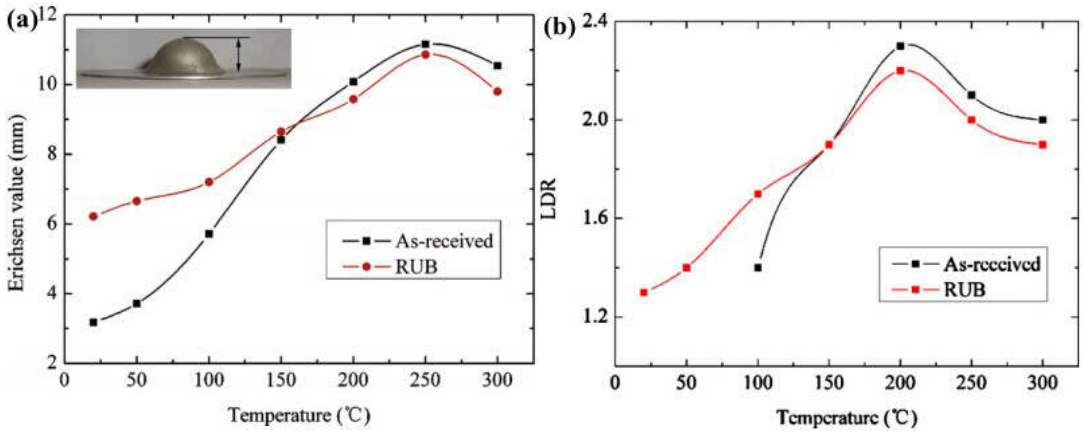

Figure 2-23 (a) The Erichsen values and (b) The limit drawing ratio (LDR) of the as-received sheets and the RUB processed sheets at different temperatures [35].

Mabuchi et al. [37] proposed that grain size dependence is related to the distribution of grain boundary misorientations by investigating and comparing the tensile properties of normal extruded Mg AZ91 alloys to ECA extruded ones. Leffers and Juul Jensen [38] described that both texture and microstructure changed dramatically when a brass plate was severely bent during rolling.

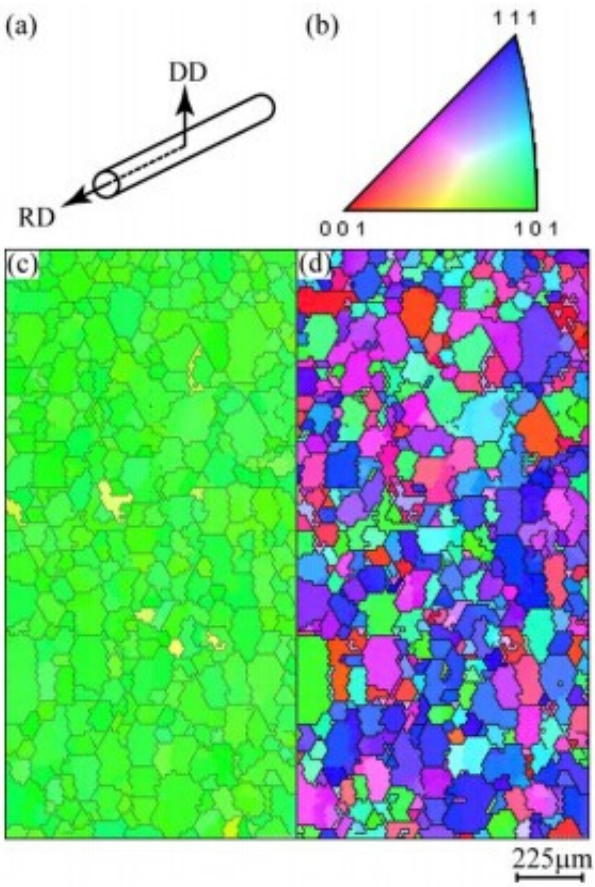

Figure 2-24 (a) Direction in the wire, (b) unit stereographic triangle, and quasi-coloured orientation mapping microstructures of (c) RD and (d) DD taken from the wire of CAM-NB cold-drawn by 76.6% and solution-treated at 900°C followed by water quenching [39].

Song et al. [40] further explained the abovementioned bendability results by investigating their texture evolution systematically. Sutou et al. investigated the effect of grain size and texture of Cu-Al-Mn-based shape memory alloys on damping properties [41] and on pseudoelasticity [39], finding that the development of texture

can enhance damping capacity, and the high tensile strength of damping materials can be achieved by controlling the relative grain size and texture (Figures 2-24 and 2-25).

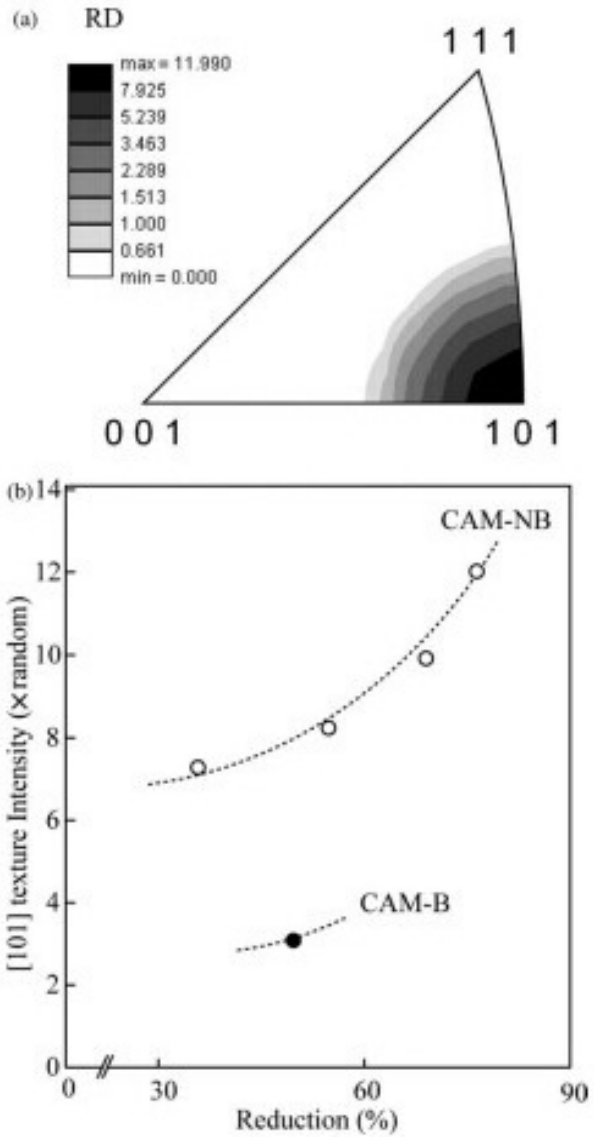

Figure 2-25 (a) Inverse pole figure in the RD for the wire indicated in Figure 2-24 (b) Plots of texture intensity of the {101}component in the RD for the solution-treated wire against the cold-drawing reduction for the CAM-NB and CAM-B wires [39].

Moreover, they discovered that the maximum pseudoelastic strain increases with increasing scale factor and wire alloys with a random texture have intermediate yield stress and transition strain. Barnett et al. [42] found that grain size can be decisive to identify twinning-slip transition by compressing extruded samples which were equipped with different gran size. Vaidya and Sinha [43] proposed a function of grain size and the degree of fibre texture to express the electronmigration response of thin film aluminium. Wang et al. [44] compared the grain size dependence of yield stress on Mg-Zn-Al alloy processed by hot extrusion and friction stir process as seen in Figure 2-26, and they analysed that high Schmid factor of 0.3 contributes to the weaker grain size dependence of friction stir processing (FSP) (Figure 2-27).

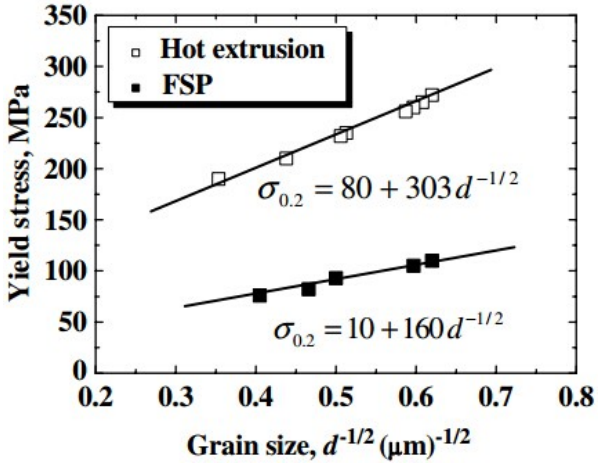

Figure 2-26 Hall–Petch relationship for the extruded and FSPed specimens at room temperature [44].

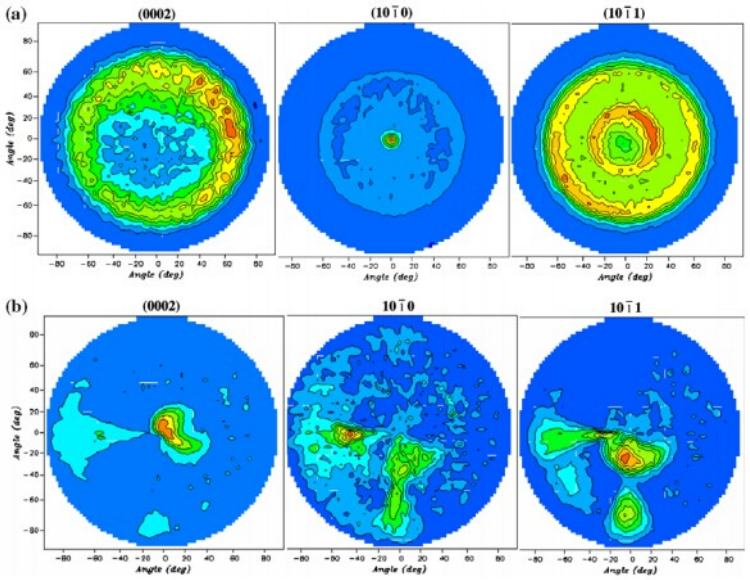

Figure 2-27 X-ray pole figures show the texture in: (a) hot extruded and (b) FSPed AZ31 samples seen from the transverse cross-sectional plane, namely, the working (extrusion or welding) direction of the specimen is parallel to the normal of the pole figures. For the FSP pole figures the ND and TD are vertical and horizontal, respectively [44].

2.3 Springback phenomenon

2.3.1 Mechanism

Springback phenomenon is a well-known characteristic of every process that involves plastic deformation, and in fact it theoretically exists in all kinds of sheet metal forming. Although it is likely to neglect its influence in most conventional manufacturing cases, there are many instances in which because of the shape or dimension of workpiece or due to the material property, this effect becomes more evident and causes adverse

consequences to be produced. Taking the automotive application field as an example, problems often occur when dealing with the deep drawing of complex and sizable pieces like B-pillars or anti-intrusion bars. Figure 2-28 shows a significant deformation which will result in a torsional effect on a B-pillar made in TRIP800. The maximum displacement measured between the nominal part and the resulting one is of the order of 10 mm, and that is far enough from being considered as negligible.

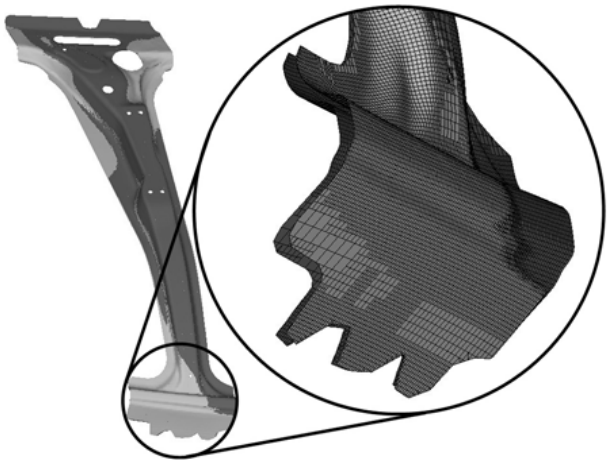

Figure 2-28 Example of a springback deformation on a B-pillar made of TRIP800 [45].

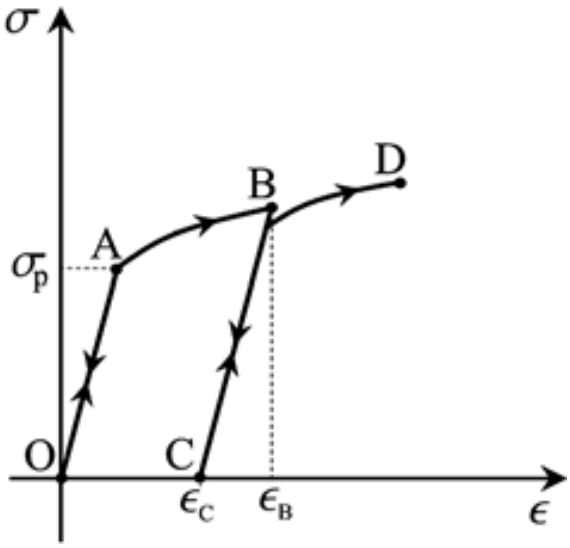

Figure 2-29 Stress-strain curve for an elasto-plastic material [45].

In order to depict the physical nature of springback phenomenon and to have a deep comprehension on how the springback amount and the material properties correlate, it is indispensable to resort to the classic elastic-plastic constitutive model for solid continua [46, 47]. Figure 2-29 illustrates the standard unidimensional behaviour for the load on a sample of a plastic material in terms of the stress σ and the strain ε. If the stress on the material overweighs the yield stress σ_p, the sample undergoes a plastic and non-reversible phase (the A-B path on the plot) that could virtually be carried on till fracture. If the stress is gradually released (from point B), the sample will "trace back" to a null tensional condition along an elastic path which obviously results in a status which differs from the original one (point C): this is the so called residual deformation. The integral of the elastic deformations from ε_B to ε_C (the B-C path on the plot) carried out over the whole volume of the sample impulses the springback effect. It now should be clear the reason why springback is so affected by the mechanical properties of the material: the higher the yield stress, the bigger the springback effect [48].

Most research has focused on reducing and compensating the springback effect without the consideration of grain inhomogeneity and has investigated micro bending with limited ratios of grain size effect when numerical and physical experiments were conducted. Therefore, it is motivated to find a method which can visually and internally reflect grain size effect in springback-related process - micro air bending and in its finite element simulation. Moreover, it is inspiring to concrete the full relationship between

the size effect and springback value. Through this relationship, some unsophisticated and feasible ways can be performed to control the springback with higher precision.

2.3.2 Experimental research on springback

Springback of sheet metals has been studied and characterised by developing various experimental techniques and procedures. The most popular and commonly used techniques are cylindrical bending [49], U-bending [50, 51], V-bending [51-54] (illustrated in Figure 2-30) and flanging [54, 55]. The high adoption rate of these methods is because the variation before and after springback is obvious, which means it can easily be observed and measured. Sensitivity of springback to basic parameters, such as R/t ratio (tool radius to sheet thickness), geometric parameters of the tools, mechanical properties of sheet material and friction parameters are usually investigated by means of these methodologies and related equipment.

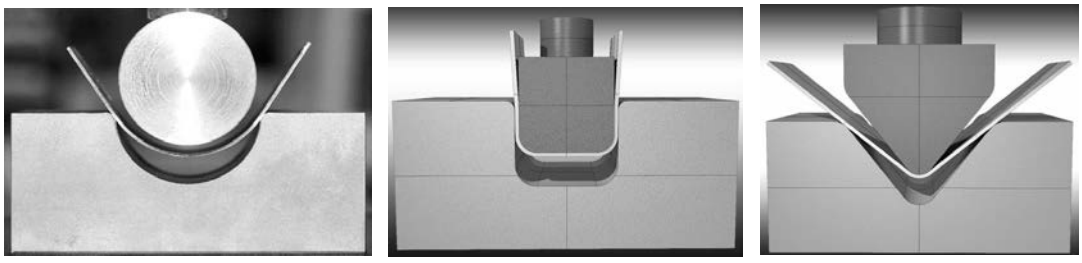

(a) Cylindrical bending (b) U-bending (c) V-bending

Figure 2-30 Most commonly adopted experimental techniques for researching springback.

Kuwabara et al. [56] conducted stretch bending tests to study the importance of tension in minimising and controlling springback (shown in Figure 2-31). During the application of the experimental procedure, the billet was largely sliding over the tools' surface to study the bending and unbending under tension at the drawbead region.

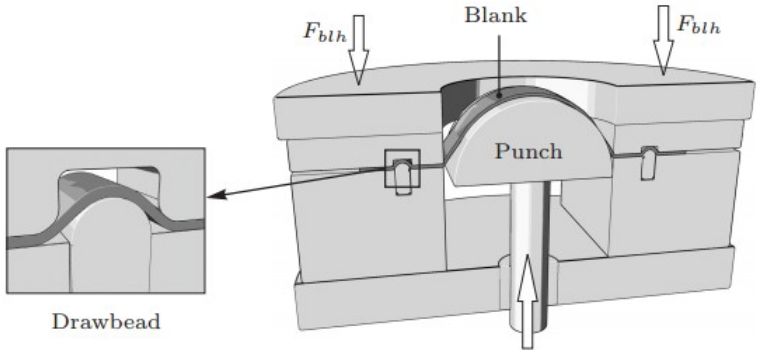

Figure 2-31 Schematic of stretch bending test [56].

The top-hat section test is often applied to assess springback in sheet metals under realistic forming conditions. During this experiment, the blank material will experience stretching, bending and unbending deformations when it passes the tool radius. This deformation path creates complex stress-strain states which will result in the formation of so-called sidewall curl (see Figure 2-32). Many researchers have carried out this experimental set-up to study springback and sidewall curl in particular [57-60], and it has been shown that the sidewall curl becomes more pronounced for small tool radii and smaller clearances between the tools [57].

(a) set- up schematic (b) springback and sidewall curl

Figure 2-32 Schematic of top-hat section test [58].

While the major shortage of the top-hat section test is the absence of effective control or direct measurement of sheet tension, which makes this experimental procedure less suitable for verifying the results of numerical simulations from [61-64]. In order to conquer this problem, Carden et al. in [61] proposed an alternative experimental method to investigate springback in sheet metal forming and its sensitivity to various parameters. The general schematic of the draw/bend test is shown in Figure 2-33.

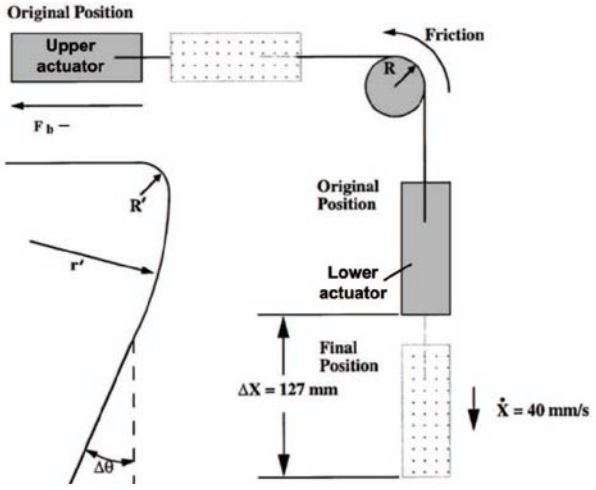

Figure 2-33 General scheme of the draw/bend test [61].

The experimental set-up consists of upper and lower actuators and there is a cylinder located at the intersection of their action lines, which represents the tooling radius. The upper actuator provides a constant restraining force, while the lower actuator is used to displace the blank at a constant speed. When drawn over the tool radius, the blank undergoes tensile loading, bending and unbending. The test is considered as a well characterised example of a forming operation that emulates real process conditions and has the advantage of simplicity [62].

It is known that the isotropic or kinematic work hardening material models are not efficient enough to describe an accurate stress state after combined stretching, bending and unbending have been conducted. The significance of taking into account the deformation history has been emphasised in references [57, 65], and several experimental procedures were advanced to study the impact of the Bauschinger effect on the sensitivity of springback.

The uniaxial tension-compression and compression-tension tests are the most common experimental procedures [66-68]. Firstly a tensile sample was prestrained to 6% in uniaxial tension, its uniform part was cut into 10 small equal segments (Figure 2-34(a)), which were then bonded together along the original tensile direction. After that the newly obtained sample was tested in compression, and the compressive loading would continue until about 1% of plastic strain was obtained (Figure 2-34(b)).

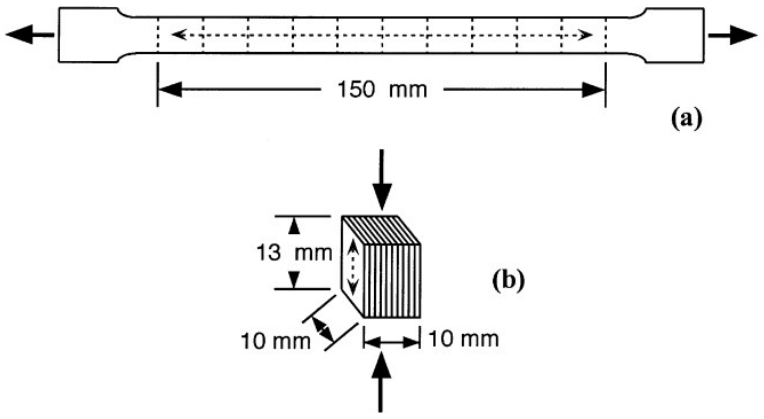

Figure 2-34 The schematic of the uniaxial tension-compression test [68].

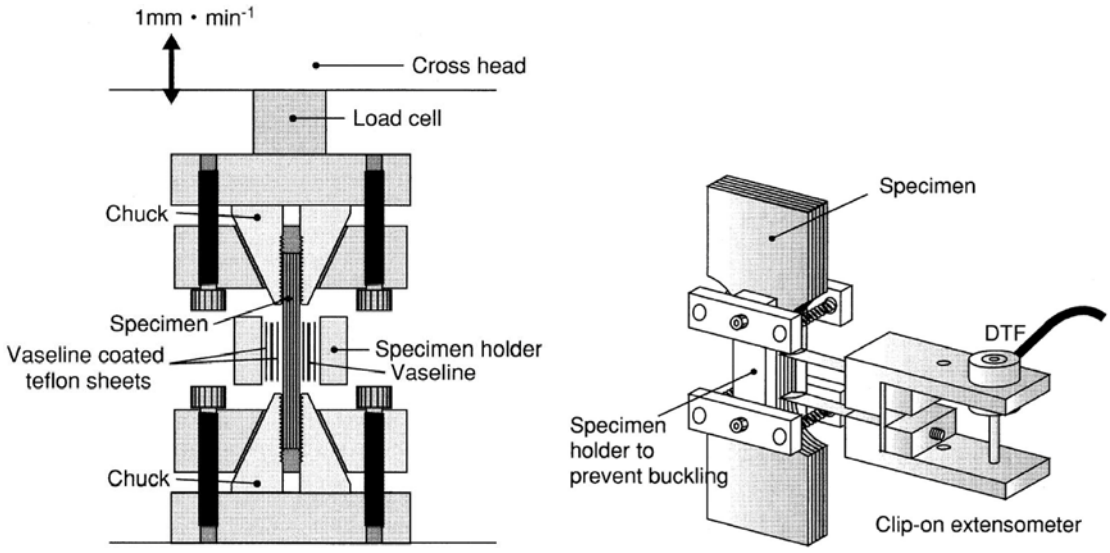

(a) set-up (b) anti-buckling device

Figure 2-35 Schematic of the in-plane cyclic tension-compression test [69].

Cyclic uniaxial compression-tension tests require special devises to be used to keep sheet materials from buckling under compression. Yoshida et al. [69] presented a set of experimental equipment, which can be used to study the elastic-plastic stress-strain

responses of sheet material. The schematic of the set-up is illustrated in Figure 2-35(a). Several pieces of sheet were bonded together to prevent buckling when compression was carried out. In addition, an anti-buckling device was attached to the specimen by coil-springs (see Figure 2-35(b)). Friction between the device and the sheet specimen was reduced by employing lubricator. It was observed that with the anti-buckling device it was possible to apply large strain reversals of about 10%.

In order to completely fix the buckling problem, pure bending and reverse bending tests as shown in Figure 2-36, were developed [66, 70, 71]. As it is shown that the punch consists of two aligned, non-rotating rods which clamp the blank to prevent any possible sliding. The lower fixture consists of two freely rotating bearings. Four rotatable rolls are fixed into each bearing. The position of the rods is adjustable to accommodate the material with various thicknesses. During the test, the punch performs vertical movement and the punch force and displacement were recorded.

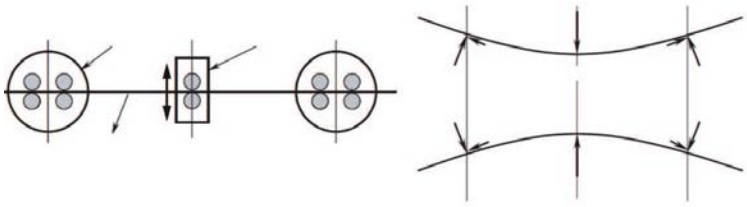

Figure 2-36 Schematic of cyclic three-point bending test [71].

A simple bending-reverse bending experimental method was proposed in references [72, 73]. As illustrated in Figure 2-37, the experimental procedure was divided into several steps: bending, turning the sheet specimen and bending in the opposite direction, turning the specimen again and bending it in the original direction, and so on. The angles after springback were measured by the coordinate measuring machine and the subordination of these angles on the deformation history can then be easily observed.

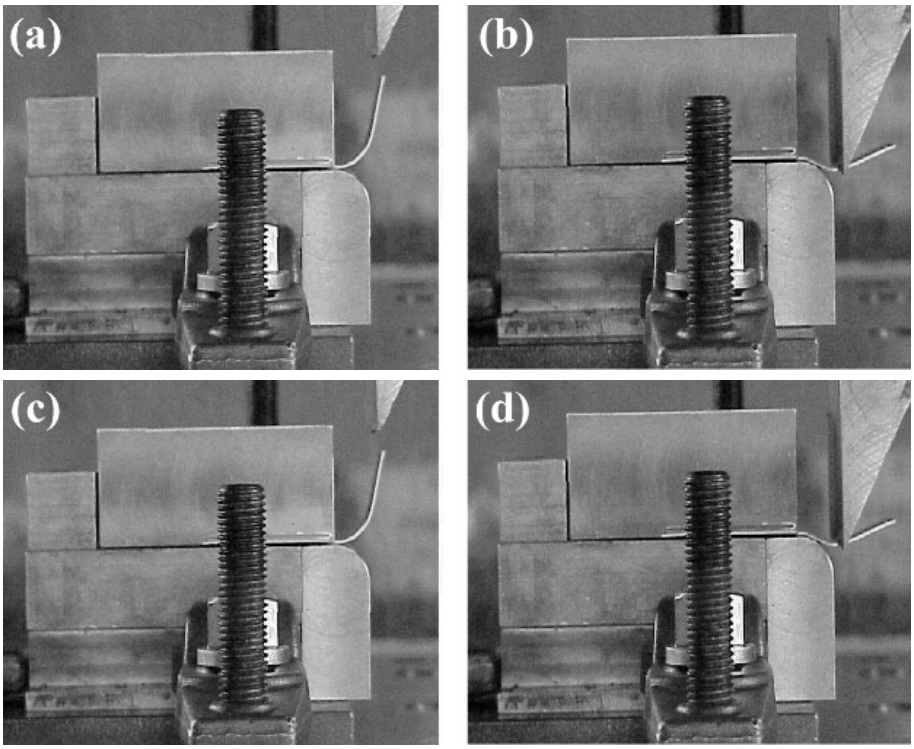

Figure 2-37 Some steps of deformation sequence during bending (a, b) and reverse bending (c, d) process [73].

There is a sufficient experimental literature dealing with understanding and characterising the springback phenomenon of sheet metals. However, the experimental methods that are capable of controlling the sliding over the tools' surfaces and that allow careful control of experimental parameters are less common. Gau et al. [24] conducted the micro three point bending with different sample thicknesses and different grain sizes, more importantly, different *T*/*D* (thickness/average grain size) ratios. The main focus of this research is to analyse the relationship between springback amount and *T*/*D* ratios, and a conclusion was made based on the results shown in Figure 2-38 that the springback of brass can be expressed as a function of *T*/*D* when its thickness is less than 350μm. Moreover, a free bending test was conducted by Diehl et al. [74] to study grain size effect on springback with foil thickness ranging from 25 to 200 microns.

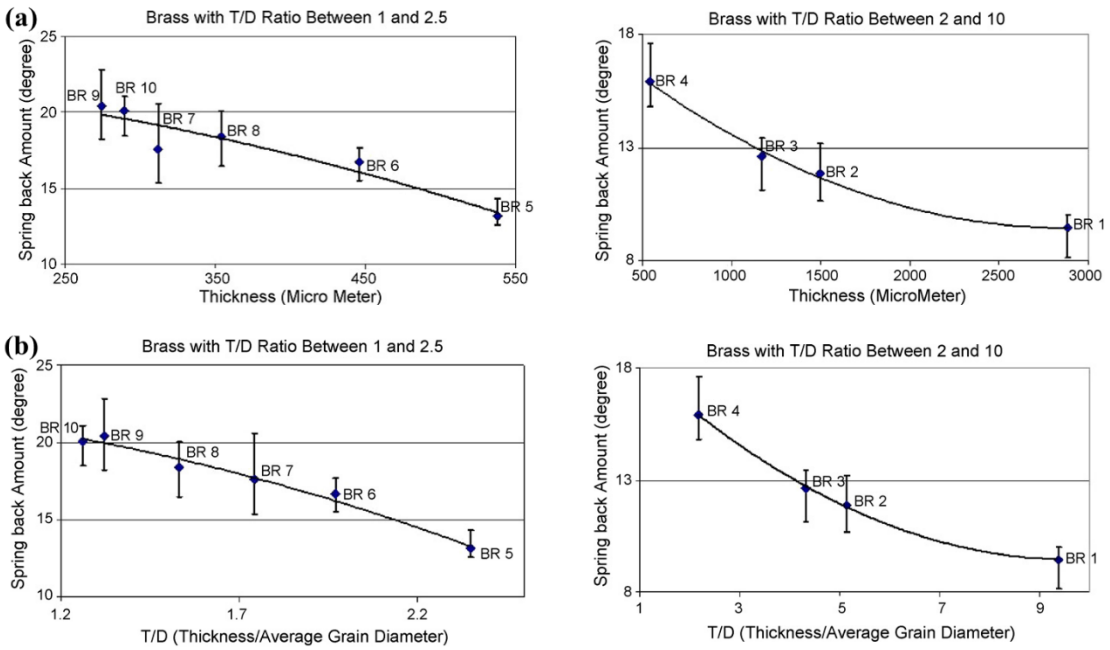

Figure 2-38 Springback vs. thickness (a) and springback vs. *T*/*D* (b) [24].

There are also other reasons could be influential to springback effect, and almost all the possible factors have been investigated in these years. Punch speed and temperature are the most frequent research objects among these researches, and they are slightly reviewed in the following.

Bruni et al. [75] investigated the springback effect of AZ31 magnesium alloy by performing air bending in the temperature range varying from 100 to 400°C, and with different values of the punch speed (0.45 and 4.5mm/s), from Figure 2-39(a) it can be seen that springback decreases with an increase of forming temperature, which is similar with results obtained from Chen et al. [76]. In addition, from Figure 2-39(b) it is obvious that a very small effect of the punch speed on springback can be observed with a trend featured by a slight drop in springback with enhancing punch speed.

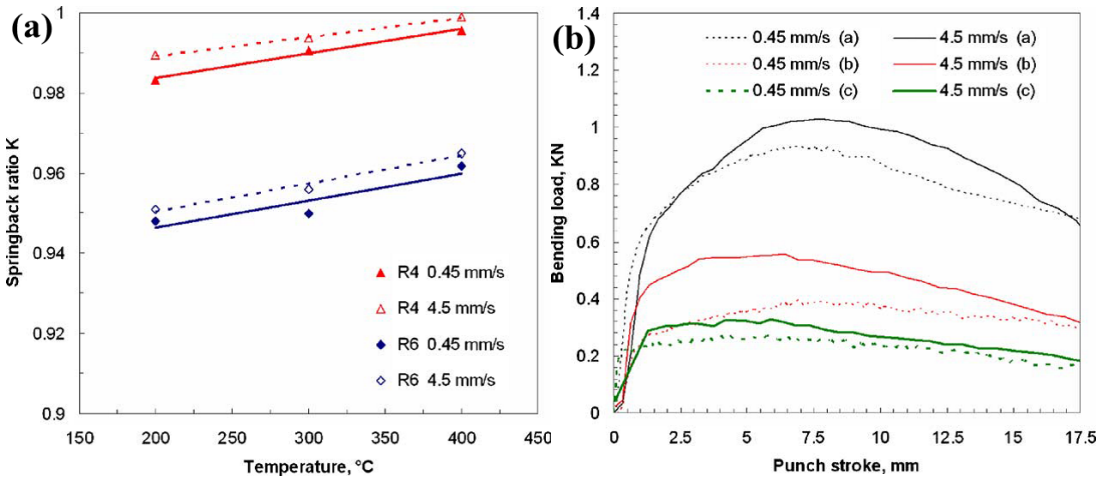

Figure 2-39 (a) Temperature effect on the springback ratio, (b) Influence of the punch speed on the load–punch stroke curves, R= 4 mm: (a)T= 200°C (b)T= 300°C and (c) T= 400°C [76].

The effect of forming temperature can be attributed to the decrease in flow stress with increasing temperature, and according to the load stroke curves, different punch speeds do not have an evident impact on the bending force, which explains the little effect of punch velocity on springback. Moon et al. [77] studied the effect of tool temperature on the reduction of springback value of aluminium of 1050 sheet with bending test equipment with special heat controller and air cooling device shown in Figure 2-40. The effect of different temperatures with different ram speeds (punch speeds) on springback is shown in Figure 2-41.

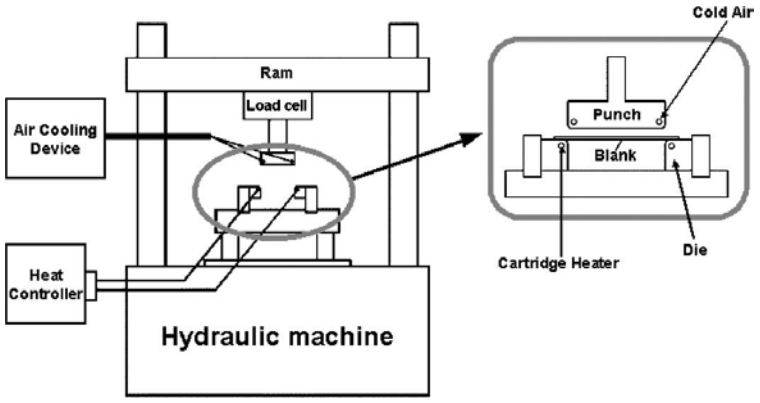

Figure 2-40 Schematic drawing of the bending test equipment [77].

The behaviour of metal sheets in press forming dies often appears to be affected by temperature [78-81], and the actual temperature is largely determined by the press speed, the metal thickness, temperature of the tools and lubrication. From the experimental outcome, it can be seen that with the increase of die temperature, the overall amount of springback dips due to the lower flow stress in high temperatures.

Besides, the sensitivity of springback on punch speed increases with die temperatures. The strain rate sensitivity of metal is quite low at room temperature [82], but it will still increase with temperature. Therefore, high die temperature with low punch speed is a justified condition for reducing springback effect.

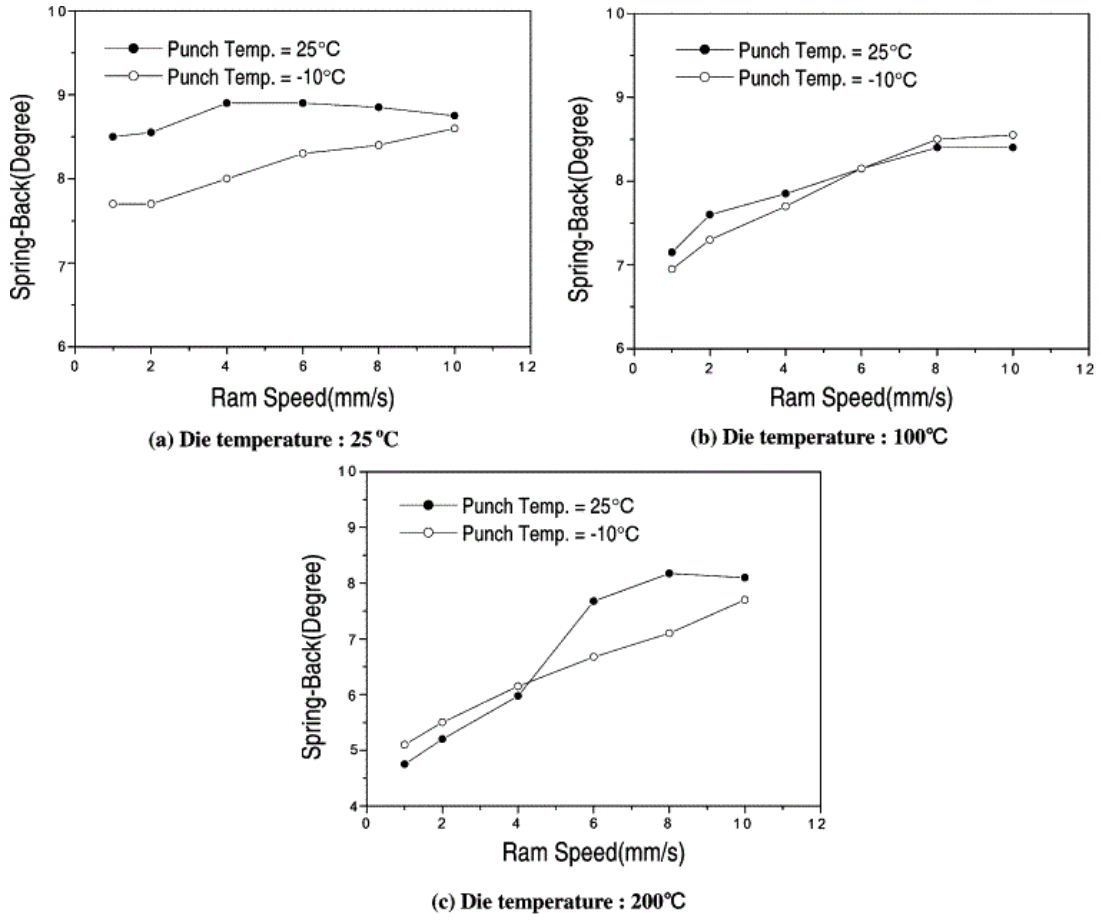

Figure 2-41 Effects of tool temperatures on the variation of springback amount at various die temperatures: (a) 25 °C; (b) 100 °C; (c) 200 °C [77].

2.3.3 Numerical simulation on springback

Like research in other metal processing fields, numerical simulation [83, 84] is a powerful tool to investigate grain size effect and springback phenomenon as well, and the research outcomes of this method will be intensively reviewed in this section. Choudhry and Lee [85] carried out a finite element model of sheet metal forming to account for the effect of inertia. Springback characteristics in plain strain U-bending process was studied by Cho et al. [86] with thermo-elastoplastic finite element model. Lei et al. [87] set up a finite element model to observe the stress distribution and predicted the springback in free bending as shown in Figure 2-42 and square cup deep drawing for stainless steel, and the results were compared with experimental data.

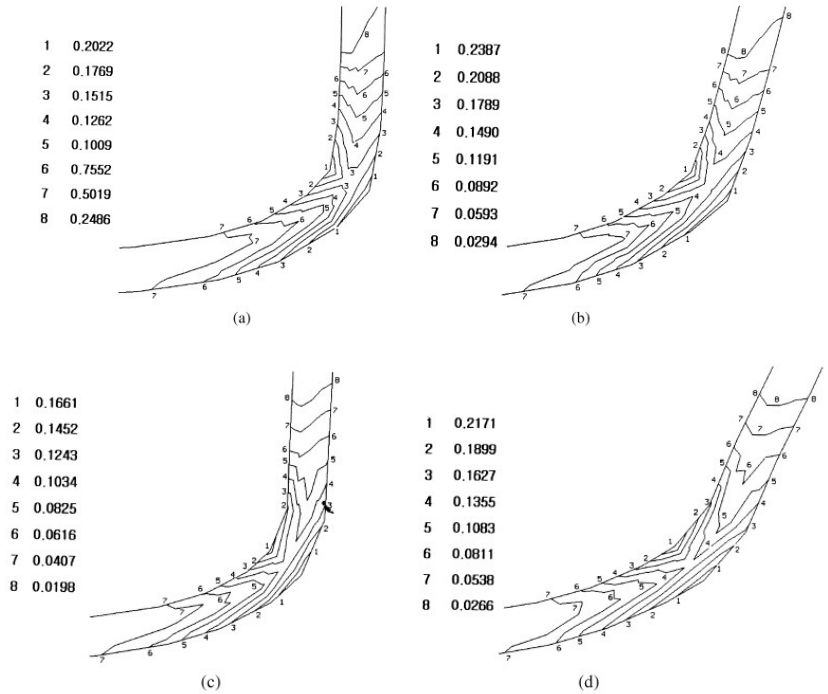

Figure 2-42 The total plastic strain distribution at the radius corner zone under different stages for STS430BA [87].

Mullan [88] studied experimentally the influence of material and loading factors on springback and derived an expression to predict springback. Papeleux and Ponthot [89] demonstrated numerically spatial integration, friction and the effect of blank holder force on the forming response. Math and Grizelj [90] adopted elastic plastic incremental finite element simulation to predict springback and analyse the residual stress in bent plates used in assembling of spherical tank, and the results were validated with experimental data. Chou and Hung [50] worked out on various springback reduction techniques in U-channel bending such as arc bottoming, over bending, punching die, spanking, stretching, movement (double bend) techniques. Chen et al. [91] investigated the effect of various materials and process parameters on the springback variation for an open channel shape part made of duel phase steel. Esat et al. [92] calculated springback of different aluminium sheets considering various thickness and simulation results were compared with empirical data.

Xu et al. [59] studied the influence of the damping value, integration point, blank mesh size and punch velocity on the accuracy and efficiency of springback simulation in U-bending process. Li et al. [93] found that the material hardening model and modulus directly affect the springback simulation accuracy in V-bending. Bui et al. [94] used the enhanced assumed strain technique in numerical simulation to predict springback. Sun et al. [95] evaluated springback in stamping using closed loop control system of a mini hydraulic press. Gomes et al. [96] investigated numerically and experimentally the variation of springback in U-bending due to material anisotropy. Ling et al. [97]

introduced step in the die to reduce springback in L-bending. Bahloul et al. [98] and Song et al. [99] used response surface methodology to optimise process parameters in sheet metal forming. Santos and Teixeira [100] proposed experimental benchmark for sheet metal forming with different materials and simulated some benchmarks numerically. Gan and Wagoner [101] proposed a new method (displacement adjustment) to design dies for sheet metal forming considering springback. Yanagimoto and Oyamada [102] explained the mechanism of the springback free phenomenon in V-bending test under warm forming condition. Oliveira et al. [103] investigated the influence of the different constitutive models on numerical simulation in a sheet metal component. Lee [104] carried out a strip drawing process with the elliptical tool to evaluate the bi-directional springback. The springback predictions in air and V-bending have been intensively researched in [52, 105-109], and Singh et al. [110] studied the effect of air bending tool geometry on springback. Panthi et al. [111] performed the bending simulation by finite element code RRL-FEM with a total-elastic-incremental-plastic (TEIP) algorithm to study the correlation between the springback and geometrical parameters, material properties and lubrication conditions.

Most of the literature reviews mentioned above are the numerical simulation on springback in macro metal forming, while the computational research on springback in microforming is limited.

2.4 Numerical simulation in microforming

Liu et al. [22] proposed a constitutive model with the consideration of grain boundary strain strengthening, and a finite element model was developed based on this condition and extreme orientations of each grain. The model shown in Figure 2-43 was run by the commercial finite element analysis software package ABAQUS/Standard, and the 4-node reduced integration element, CPS4R, was adopted.

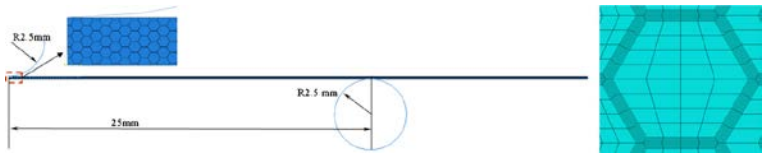

Figure 2-43 FE model of three-point bending [22].

It is found that springback angles increase with the decease of sheet thickness, and this is consistent with the conventional bending theory used in macro scale bending. Grain size effect was not expressed obviously in this research, however, it took the influence of grain boundaries into consideration but did not regard the material as homogenous one.

The grained heterogeneity was taken into account by Chan et al. [18] to investigate the scatter of flow stress and grain behaviours shown in Figures 2-44 and 2-45. It is illustrated that the scatter of flow stress is caused due to different grain sizes, grain

shapes and grain orientations unevenly distributed in the testing samples and the flow stress curves of grains is derived via evaluating the degree of the spread of testing samples' flow stress.

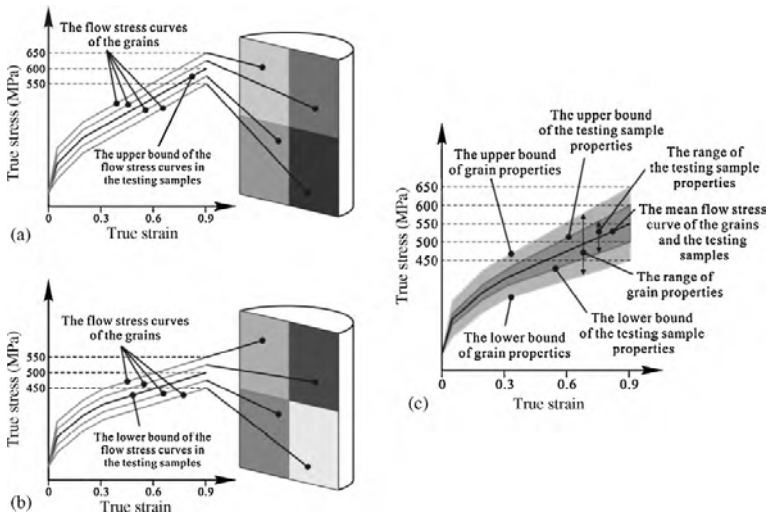

Figure 2-44 The upper and lower bounds of the grains and the testing sample properties [18].

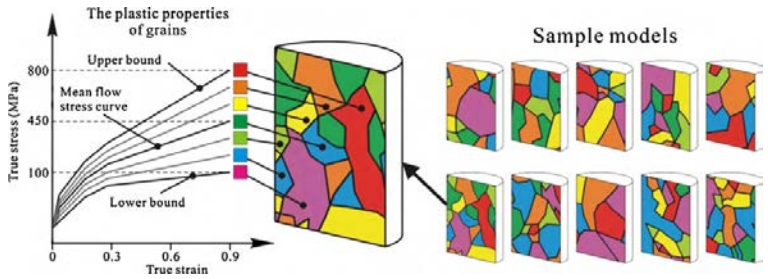

Figure 2-45 Grain properties randomly assigned on the metallographies of the sample models [18].

For the simulation part, firstly, the area fraction of each grain in each sample model was obtained with the aid of a CAD system, and then the metallography was represented by unit areas which were represented by grids shown in Figure 2-46.

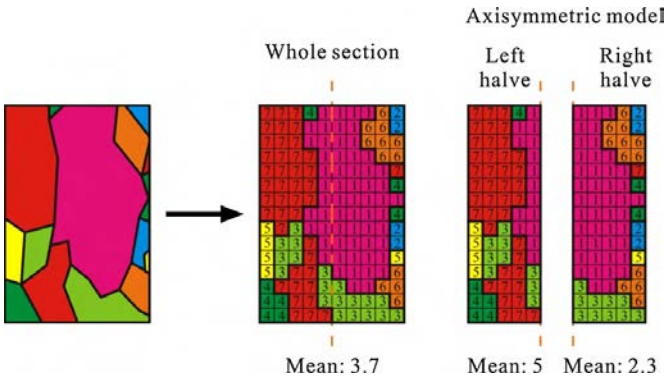

Figure 2-46 Influence on mean flow stress in an axisymmetric model [18].

The thick line represents the grain boundary, and different colours and numbers in the grids are used to differentiate the properties of grains. After this, the grain properties were assigned into the model's different colour areas to simulate the material deformation behaviour. Thus, this provides an avenue for understanding and modelling of grain size effect in microforming process.

In the research of Lu et al. [112], the authors investigated the scatter of grain properties via nanoindentation as illustrated in Figure 2-47(a), and then combined these grain properties with a 3D Voronoi tessellation model to simulate the micro-compression with ANSYS/LS-DYNA. According to the grain hardness, the deformability of

individual grain inside the micropart can be estimated. The ratio of the hardness at each class divided to the average hardness was defined by introducing an inhomogeneity coefficient α to make the grain properties curves vary following the statistical distribution which was divided into 7 classes as shown in Figure 2-47(b).

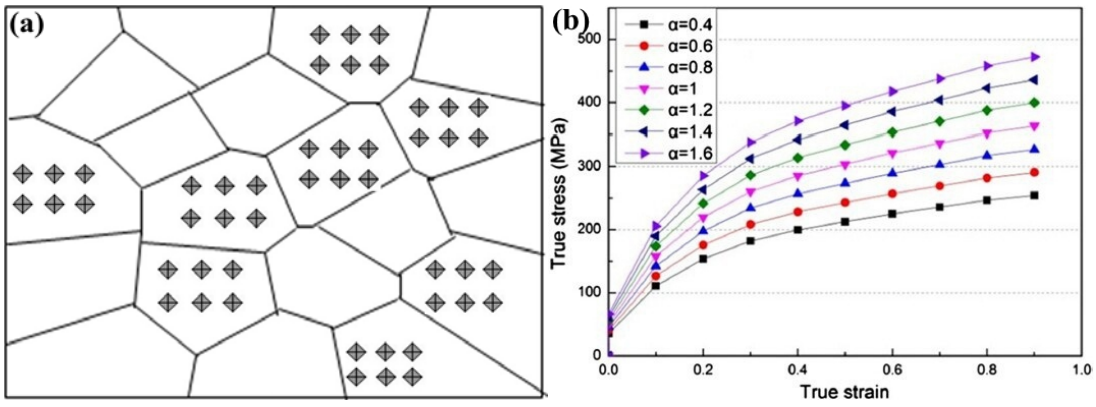

Figure 2-47 (a) Illustration of nanoindentation and (b) flow stress of inhomogeneous material [112].

In the simulation part, as mentioned before, the authors proposed a solid Voronoi diagram model to represent the deformed part, which can reflect the grained heterogeneity which was regarded as one of the most significant differences between macroforming and microforming directly in finite element model seen in Figure 2-48(a, b). Then in the messing process, space was discretised and described with a 3D digital image composed of voxels and the billet was meshed with regular cubic elements to control the numerical simulation cost and geometrical error of grain boundaries illustrated in Figure 2-48(e-f).

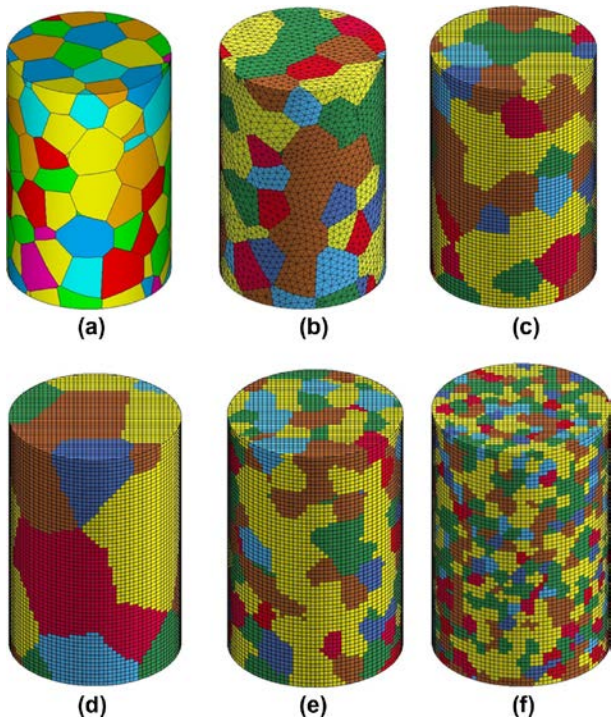

Figure 2-48 Aggregate of polycrystalline, (a) tessellation in 140 voronoi polyhedral, (b) freely meshed model with 140 subdomains, (c–f) microstructure mapping on a 1313×60 cubic element mesh and domain with subdomain numbers 140, 26, 385, 2520 respectively [112].

2.5 Summary and objectives of the work

In this chapter, an introduction to a special phenomenon in microforming processing called “size effects” was given, in addition to its role in resulting different mechanical behaviours and crystallographic characteristics. Further, experimental research and numerical studies on springback which is an inevitable result from plastic deformation

are reviewed in detail. The modelling in microforming has also been reviewed through since it is a major research tool in studying material processing.

According to the literature review, there are some blanks in the research of microforming, for instance, the relationship between grain size effect ratio and mechanical behaviour, and the relationship between grain size effect ratio and the change of crystallographic orientation especially when the ratio is limited in a certain range. Moreover, a more accurate modelling technique for FE simulation is needed with the consideration that current modelling cannot display the topology of specimens' microstructure and the grain heterogeneity simultaneously.

Base on the above summary and analysis, in this thesis, several objectives will be tackled in order to obtain a clear and unambiguous understanding of grain size effect in microforming, the objectives are as follows:

(1) To study size effects in term of specimen's thickness (T) /average grain size (D) in micro tensile test and micro V-bending.

(2) To understand the influence of T/D values (>1, <1 and ≈ 1) on plastic deformation behaviour and fracture behaviour in micro tensile test.

(3) To comprehend the effect of T/D values on texture evolution in annealing process and micro V-bending process.

(4) To propose a new FE simulation approach which combines the Voronoi diagram and the grain heterogeneity and can deliver reliable prediction.

Chapter 3 Experimental instruments, numerical software and methodologies

In this chapter, the experimental instruments, numerical software and methodologies adopted in this study are briefly introduced. The corresponding results are described in detail in the following chapters.

3.1 Material

Nonferrous metals are widely applied in electronic components, medical apparatus and devices in terms of microparts due to their high electrical and thermal conductivity, good ductility and excellent wear resistance, fatigue strength and bearing properties. The most commonly used wrought forms are strip, rod, wire and tube.

C5191 phosphor bronze foil is chosen as the experimental material in this study. Main components of C5191 phosphor bronze are copper, tin and phosphor, and the chemical compositions of C5191 are displayed in Table 3-1. The typical microstructure of C5191 is shown in Figure 3-1. The supplier of this material is K.T. Global Incorporation, Kanagawa, Japan. The supplied form is 1000 mm×100 m×0.07 mm cold rolled coil.

Table 3-1 Chemical compositions of phosphor bronze C5191, in wt%.

Element	Sn	P	Pb	Fe	Zn
Contents	5.87	0.22	0.004	0.001	0.004

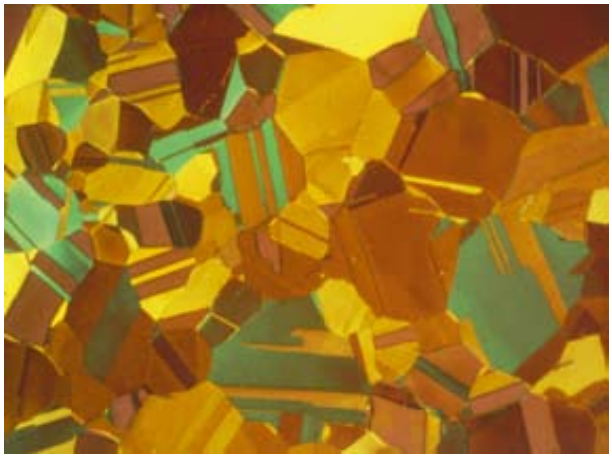

Figure 3-1 Microstructure of phosphor bronze C5191.

3.2 Material sectioning

The sectioning of phosphor bronze foil includes two conditions. One is sectioning for micro tensile test, and its schematic is shown in Figure 3-2. The dimension of the tensile sample is designed according to ASTM E8/E8M. The other is cutting for micro V-bending test, and its dimension is 2 mm×1 mm×0.07 mm. Both sets of sectioning were conducted on a wire-cut electrical discharging machine (EDM).

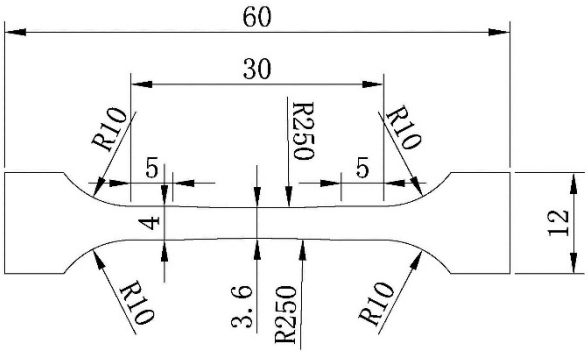

Figure 3-2 Schematic of micro tensile samples (unit: mm).

3.3 Heat treatment experiment

In order to obtain different average grain sizes in materials to achieve different grain size effect ratios, annealing heat treatment was carried out. The micro tensile and micro V-bending samples were annealed in a KTL1400 vacuum tube annealing furnace (Figure 3-3). Because the samples are very small, besides vacuum condition during heat treatment, the Ar air protection was also adopted to avoid oxidation.

Figure 3-3 Photo of KTL1400 tube furnace.

3.4 Sample preparation

After annealing, samples for micro V-bending were mounted in fine Polyfast powder (conductive resin). The normal size Polyfast power will compress the samples severely during mounting process so that the flat samples can become warped. Therefore, a grinder was used to treat Polyfast powder to fine level to ensure the flatness when mounting.

Figure 3-4 Struers automatic grinder and polisher Tegrapol 21.

Table 3-2 Sample preparation procedures for microstructural analysis.

Procedure	Surface	Force, N	Time, min	Solution
Grinding	1200# Sic paper	30	2	Water
Grinding	9μm Largo cloth	30	4	DP-lubricant red
Polishing	3μm Mol cloth	25	3	DP-lubricant red
Polishing	OP-chem	15	1.5	OP-S

The following grinding and polishing were performed on the Struers automatic Tegrapol 21 (Figure 3-4). The grinding and polishing procedures for metallography are presented in Table 3-2.

For electron backscatter diffraction (EBSD) test, the samples were treated further. Due to the softness and microscale level of samples, an ion beam milling system (Leica EM RES101) was adopted to finalise polishing, qualifying the surface of samples for EBSD data acquisition. The milling period for each sample was 15 minutes with 1.5 (revolutions per minute) RPM rotation, Dual ion beam (Argon) milling is at +3 degree angle to sample surface with 4kV beam energy at 2mA current. The image of Leica EM RES101 is illustrated in Figure 3-5.

Figure 3-5 Photo of Leica EM RES 101.

3.5 Optical microscope (OM)

The concept of OM (also referred to as “light microscope”) applied to the investigation of materials is to use visible light and a series of lenses to magnify images of specimens and examine the microstructure of materials. The OM used in this study was Leica DMR OM and the photo of this microscope is shown in Figure 3-6.

Figure 3-6 Photo of Leica DMR OM.

3.6 Micro tensile test

In order to carry out uniaxial micro tensile test on materials with different grain size effect ratios, a set of INSTRON 5848 micro tester (as shown in Figure 3-7) was selected. This equipment can offer ultra-precise displacement control: 20 nm and can accommodate odd-shaped components. A video extensometer is also installed to ensure the accuracy of stress/strain measurements. Therefore, it is very suitable to be

employed to investigate microscale level deformation behaviour and deliver reliable and accurate results.

Figure 3-7 INSTRON 5848 micro tester with video extensometer.

3.7 Micro V-bending

3.7.1 Machine

Micro V-bending test was conducted on the desk-top servo press machine DT-3AW system (Figure 3-8), which is capable to afford position accuracy within ± 2μm. The equipment was used to conducting micro V-bending experiment. The research objectives focus on the springback amount after unloading and the change of grain orientations before and after V-bending.

Figure 3-8 Photo of the desk-top servo press machine DT-3AW system.

3.7.2 Moulds

A set of self-designed bending mould including upper mould, lower mould and punch and V-die were employed respectively as shown in Figures 3-9 and 3-10.

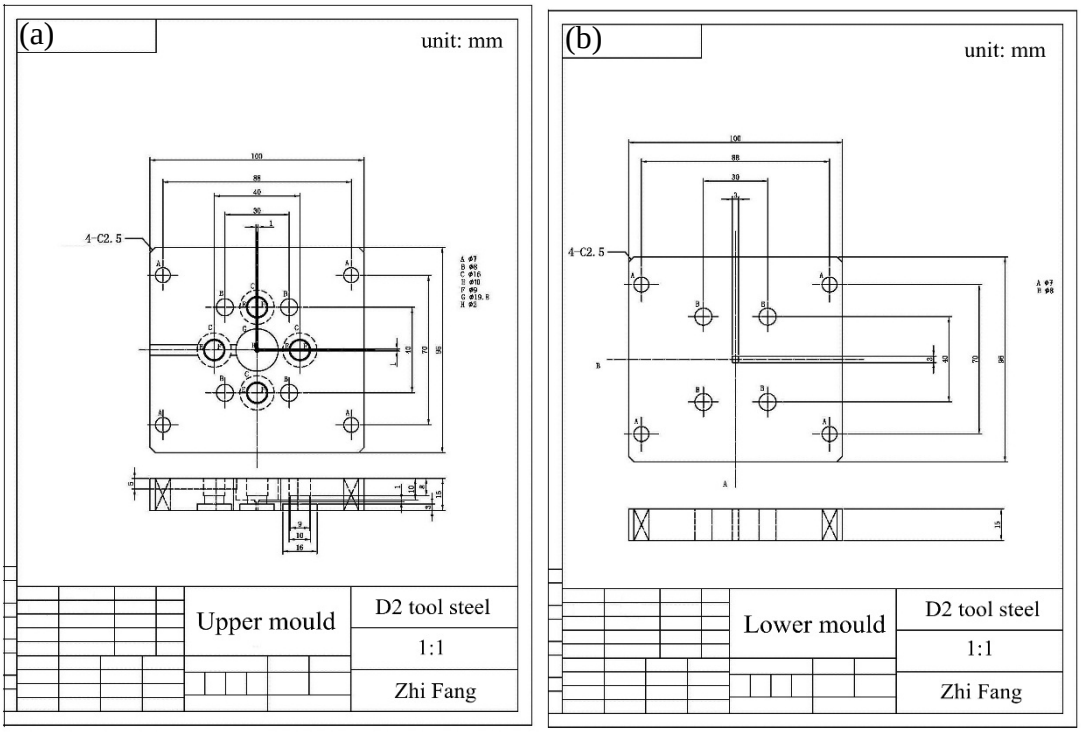

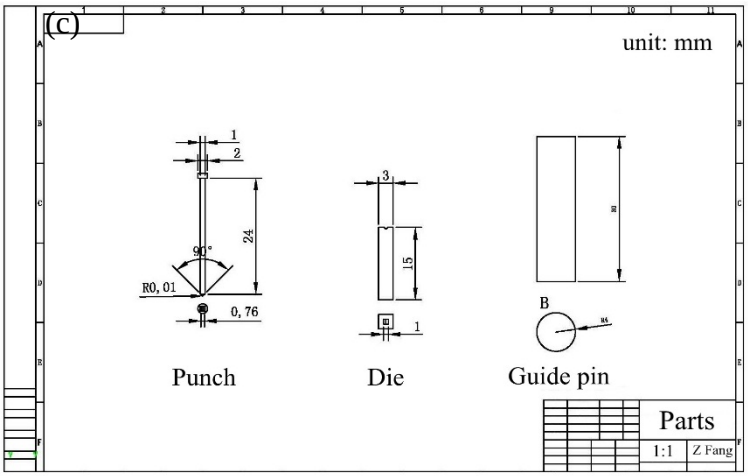

Figure 3-9 The design drawing of the upper mould, the lower mould, the punch and the V-die.

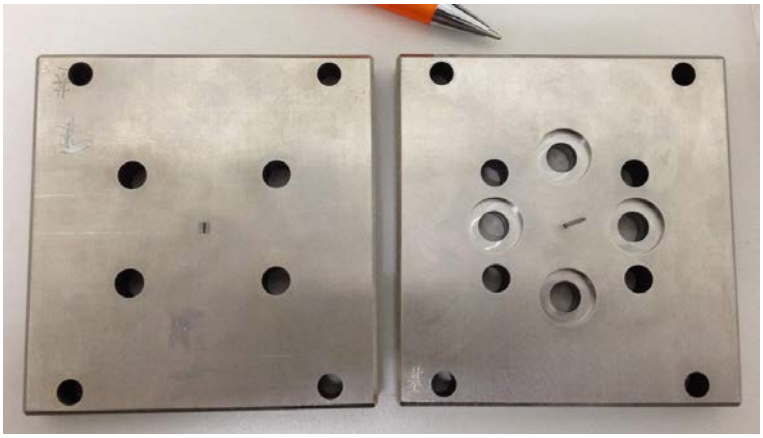

Figure 3-10 Photo of the assembled upper mould and the lower mould.

3.8 VHX-1000 digit microscope

Unlike the traditional microscope, VHX-1000 KEYENCE microscope (Figure 3-11) can provide online measurement. This function was used to measure springback angles after magnifying the bended samples.

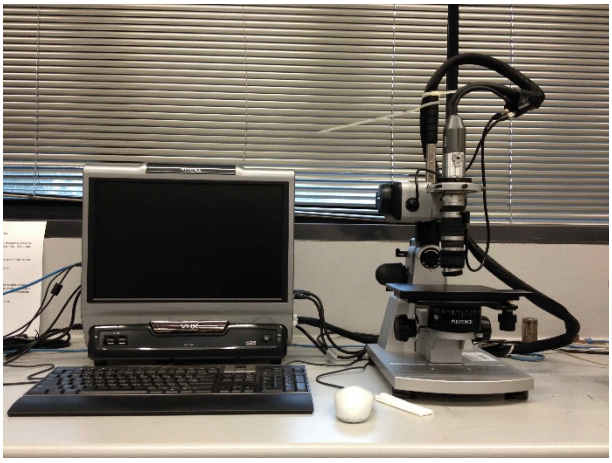

Figure 3-11 Photo of VHX-1000 KEYENCE microscope.

3.9 Scanning electron microscope (SEM)

SEM is a type of electron microscope that produces images of a sample by scanning its surface with a focused beam of electrons. JEOL 6490 SEM (as shown in Figure 3-12) was used to investigate the microstructure of specimens and fracture surfaces.

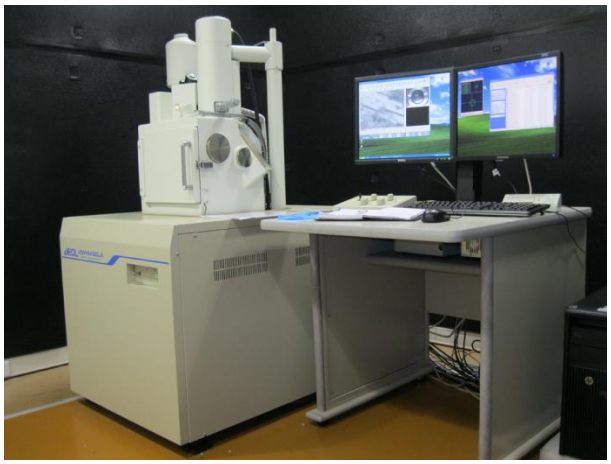

Figure 3-12 Photo of JEOL 6490 SEM.

Electron backscatter diffraction (EBSD) is a microstructural crystallographic technique which is used to examine the crystallographic orientation in materials. In the present study, JEOL 7001F field emission gun scanning electron microscope (FEG- SEM) (Figure 3-13) was adopted to acquire the information about the orientation of grains in flat and bended samples and to construct the EBSD maps.

Figure 3-13 Photo of JEOL JSM 7001F FEG-SEM.

The EBSD maps were collected from the FEG- SEM at voltage of 15kV. The HKL Channel 5 software was used to analyse the acquired maps in offline mode. The software interface is shown in Figure 3-14.

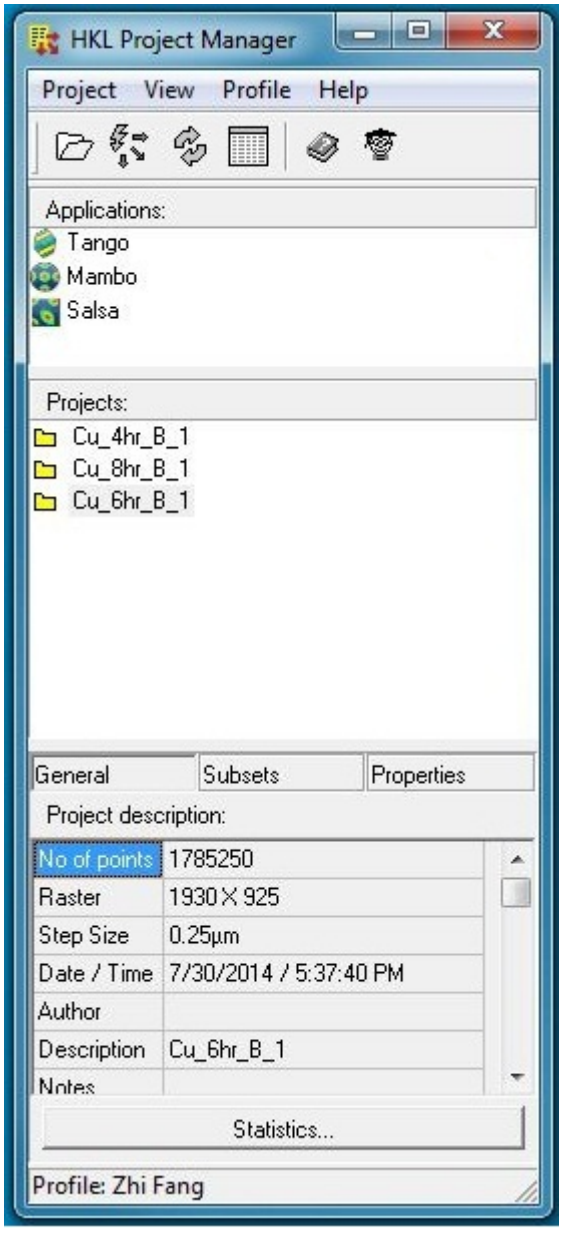

Figure 3-14 The interface of HKL Channel 5 software used to interpret the EBSD data.

3.10 Software applied for numerical simulation

To obtain a better understanding of microforming, numerical simulation was also carried out except for physical experiments. However, it is not easy to conduct because the most obvious difference between conventional models and microforming models is that the materials involved cannot be recognised as homogenous ones. This requires an innovative approach to be adopted in the modelling to realise the inhomogeneity of microforming samples. In this study, Voronoi tessellations were proposed to solve this problem, and three kinds of software: MATLAB, Python and ABAQUS were used to achieve this goal.

3.10.1 MATLAB

MATLAB (matrix laboratory) is a multi-paradigm numerical computing environment and fourth-generation programming language. Developed by MathWorks which is an American privately held corporation that specialises in mathematical computing software, MATLAB allows matrix manipulations, plotting of functions and data, implementation of algorithms, creation of user interfaces, and interfacing with programs written in other languages, including C, C++, Java, Fortran and Python. In this research, 2D and 3D voronoi diagrams were plotted by MATLAB in graphic user interface (GUI), and all the vertex and edges data were acquired according to this software. The MATLAB version applied in this study is MATLAB R2013a.

3.10.2 Python

Python is a widely used general-purpose, high-level programming language, and it has been successfully embedded in a number of software products as a scripting language, including in finite element method (FEM) software such as ABAQUS, 3D animation packages such as 3ds Max, Blender and Cinema 4D. In this modelling, Python (Version 2.7) acts as a bridge to link the plotting data of Voronoi diagram in MATLAB to the pre-processing in ABAQUS/CAE.

3.10.3 ABAQUS

ABAQUS is a software suite for finite element analysis (FEA) and computer-aided engineering (CAE). The ABAQUS version applied in this study is ABAQUS 6.11. It consists of five core software products:

(1) ABAQUS/CAE, a software application used for both the modelling and analysis of mechanical components and assemblies (pre-processing) and visualising the FEA results. A subset of ABAQUS/CAE including only the post-processing module can be launched independently in the ABAQUS/Viewer product.

(2) ABAQUS/Standard, a general purpose FE analyser that employs implicit integration scheme.

(3) ABAQUS/Explicit, a special-purpose FE analyser that employs explicit integration scheme to solve highly nonlinear systems with many complex contacts under transient loads.

(4) ABAQUS/CFD, a computational fluid dynamics software application which provides advanced computational fluid dynamics capabilities with extensive support for pre-processing and post-processing provided in ABAQUS/CAE.

(5) ABAQUS/Electromagnetic, a computational electromagnetic software application which solves advanced computational electromagnetic problems.

In this microforming numerical simulation, ABAQUS and MATLAB were used to conduct micro V-bending simulation combining with Voronoi diagrams implemented by Python script files.

3.11 Research methodology

The research methods which are involved with this dissertation can be categorised as physical experiment and numerical modelling. For physical experiments, micro tensile tests and micro V-bending have been chosen as the processing method to investigate the research objectives. Grain size effect is expressed by the ratio of specimen's thickness (T)/ average grain size (D), and this variable can be achieved by heat

treatment recrystallisation grain growth. In this study, annealing is chosen to obtain different average grain sizes with fixed specimens' thickness so that the ratio *T*/*D* can be valued greater than 1, smaller than 1 and approximately equal to 1. To analyse the tensile tests' results, Scanning Electron Microscope (SEM) is used to observe fracture morphologies, and Electron Back Scattered Diffraction (EBSD) technology is employed to detect texture characterisation both in annealing and micro V-bending. All the experimental results are discussed and analysed from a size effects (*T*/*D*)-centred perspective.

To numerical analysis, the numerical modelling is carried out on commercial and prestige finite element (FE) software ABAQUS and the grain heterogeneity is reflected in the model simultaneously. The application of Voronoi diagram[113-120] is conducted in the research, and the combination between micro V-bending FE model and Voronoi tessellation is the highlight which is distinctive when comparing to other FE models. Besides, the Python script language has been frequently used during Voronoi tessellation generation and the grain heterogeneity realisation, which saves a large amount of time instead of desktop operating ABAQUS pre-processor.

3.12 Summary

The experimental facilities, simulation software and methodologies used for the current study were introduced in this chapter. The detailed experimental and modelling

procedures employed to study a particular condition as well as corresponding results are presented and discussed in the following chapters.

Chapter 4 Effects of thickness/average grain size on micro deformation behaviour and fracture

4.1 Introduction

The popularity of microforming technology has attracted tens of thousands of attentions due to the prevalent usage of its matching products-micro parts. The increasing demand of micro-scale products for high accuracy and high quality has also inspired the development of microforming technology. Although the metal forming in traditional level has been progressed for centuries and a series of classic knowledge and theories have been established systematically by previous researchers, it is common known that these macro-scale processing theories cannot be directly applied in micro-scale world with minaturisation due to size effect [6, 13, 121]. When the scaling of specimens downsize to micro-level, the parameters which may not be important in conventional process begin to play a significant role in controlling the accuracy of deformation, and in another way, determining the dimensions of processed specimens.

Several researches have been conducted to investigate the size effect in micro deformation behaviours and mechanics. Engle and Eckstein [6] proposed the surface

layer model to explain why flow stress reduced in microforming process. Geiger et al. [11] and Vollertsen et al. [12, 13] conducted a comprehensive assessment of state of the art of microforming technology. Fu et al. [122] updated the development of these microforming technologies in the latest review. Diehl et al. [123] systematically investigated the relationship between the microstructure and mechanical properties and the forming behaviour by tensile and hydraulic bulge tests and bending test on thin metal foils. Ma et al. [14] researched the size effect on fracture behaviour in deep drawing process. Their results illustrate that limit drawing ratio (LDR) is significantly decreased with grain size. Kals and Eckstein [15] carried out tensile tests, air bending and punching to investigate the size effect in sheet metal forming by miniaturisation based on similarity theory. Research from Raulea et al. [17] exhibited that the yield strength is interrelated with the proportion between the grain size and specimen thickness. Chan et al. [18] studied the scatter of grain mechanical properties with micro-compression process and proposed a FE model featuring grain size and the scatter of flow stress. Moreover, they investigated the interactive effect of specimen and grain sizes on deformation behaviour [124] and the size effect of pure copper in micro extrusion process [125]. Lu et al. [112] enhanced this modelling by implanting Voronoi tessellation algorithm into pre-processor of finite element software. Moreover, Xu et al. [21, 126] studied the size effect on deformation behaviour and fracture feature by micro-blanking in terms of the ratios of different blanking clearances to grain size. Wang et al. [23] studied the size effect of cavity dimension in coining process and revealed that the micro-formability decreased with the increase of the ratio of grain

sizes to die cavity width. Gau et al. [24] conducted three points bending to study the correlation between springback amount and *T*/*D* (thickness/average grain diameter) ratios. They observed that springback is related to the ratio of sheet thickness to grain size, but all the ratios were larger than 1. Liu et al. [22] developed a constitutive model considering the grain boundary strain hardening. Yeh et al. [127] also proposed a mathematical model which took into account the thickness and grain size effect in micro cup drawing. Fu et al. [16] investigated the size effect on fracture mechanism of annealed copper foils with different *T*/*D* by tensile testing, and they concluded that the number of micro-voids decrease with the decrease of *T*/*D*. Hmida et al. [26] observed the formability decreases with the increase of *T*/*D* by the single point incremental forming process of copper foils with various grain sizes and thickness. Chan and Fu [128] carried out experimental studies and numerical modelling on the flow stress of sheet metal in microforming in terms of *T*/*D*. Michel and Picart [129] also conducted tensile and hydraulic bulging tests on CuZn36 to evaluate size effects on the constitutive behaviour. However, the ratios of thickness to grain size in these studies are limited in greater than 1. Yun et al. [130] proposed a constitutive model for thin metal considering the first order size effects, but they found that the great offset occurred when $T/D<1$. Peng et al. [131] adopted a uniform double linear constitutive equation into their model to study the constitutive behaviour in microforming, and proposed a uniform size dependent constitutive model by introducing a scale factor to evaluate the material behaviour [132].

In microforming, the size effect of materials plays a significant role in influencing the deformation results and the accuracy of final products. Nevertheless, it is noticeable that among the prior studies, there is a lack of in-depth research on the interactive effect of micro deformation and fracture behaviours, and the size effect expressed by the ratios of specimen thickness to grain size, especially when they are approximately larger than, equal to and less than 1. This means there is just more than one grain, only one grain or an incomplete grain in the thickness direction. In this study, uniaxial tensile tests were carried out with phosphor bronze foil to study the effect of the ratio T/D on micro scale plastic deformation, and their fracture morphologies were observed under SEM. The ratios are reflected as $T/D>1$ (1.23), $T/D<1$ (0.68) and $T/D\approx1$ (1.07) respectively by means of different annealing treatments. At the same time, with consideration that the surface layer model cannot be applicable when $T/D<1$, a new constitutive model are proposed based on the classic composite model. The results obtained from the model are compared with the experimental ones, and the efficiency of the developed model is verified.

4.2 Experiments

4.2.1 Sample preparation

Phosphor bronze C5191 foil from cold rolling with thickness 70 μm was employed to conduct this research due to its wide application in industries. The chemical compositions of phosphor bronze are displayed in Table 3-1.

The grain size effect which is the interactive effect between the specimen and grain size is expressed by the ratio of the specimen thickness to average grain size:

$$\text{Grain size effect} = \frac{specimen\ thickness\ (T)}{average\ grain\ size\ (D)} \quad (4\text{-}1)$$

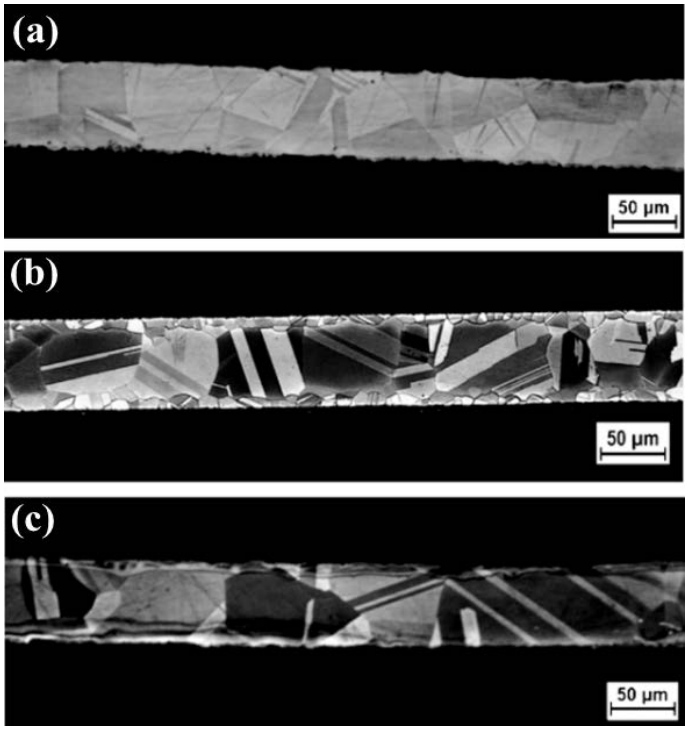

Figure 4-1 Microstructure of annealed phosphor bronze foil. (a) T=70μm, D=57.1μm, T/D<1; (b) T=70μm, D=65.7μm, T/D≈1 and (c) T=70μm, D=103.1μm, T/D<1.

To realise the grain size effect which is greater than, less than and equal to 1 individually, the materials were annealed with different temperatures and holding times in Ar air protection condition before furnace cooling. The anneal conditions are presented in Table 4-1. Although the range of grain size effect is small (from 0.68 to

1.23), what these three ratios reflect three different special microstructural features: a few grains exist in thickness direction, one grain exists in thickness direction and one partial grain in thickness direction. So from this point, the focus of this research is to investigate the effect of three microstructural features and their deformation mechanisms during microforming. This is distinctive from other research which has a large range of ratio values, while only one microstructure is expressed: several grains in specimen's thickness direction.

Table 4-1 Heat treatment and average grain size.

Temperature (°C)	550	550	550
Time (h)	4	6	8
Thickness, T (μm)	70	70	70
Average grain size, D (μm)	57.1	65.7	103.4
T/D	1.23	1.07	0.68

The heat-treated specimens were etched using a solution of 5g of FeCl3, 50ml of HCl and 100ml of H2O for 1-2 s. The microstructures of three different grain sizes in thickness direction are shown in Figure 4-1. It can be seen that the grain size increases with holding time under the same annealing temperature. The average grain size was obtained by software IMAGE J. Straight line was drew along longitudinal direction in microstructure image. The line was both starting from and ending at the boundary of a certain grain. The length of the line was L, and the quantity of the grains which were intercepted by the line was N (N≥30). Then the average grain size was obtained as L/N.

Total 10 samples were observed and measured in this way for each group. The largest and smallest values were discarded, and the final average grain size was the average value for the rest 8 samples.

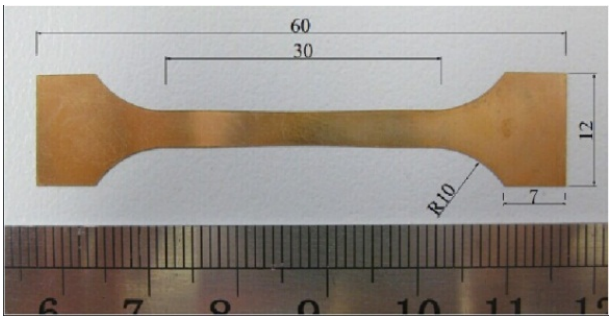

Figure 4-2 The tensile test specimen.

After confirming annealing schedules, the original specimens were sectioned to dog bone-shape which can be seen in Figure 4-2 by a wire-cut electrical discharging machine (EDM). The cut specimens were heat treated to be featured with the different grain size effect ratios: $T/D<1$, $T/D\approx1$ and $T/D<1$. This operation (annealing after sectioning) can avoid the machining stress during EDM since the material is so thin.

4.2.2 Micro tensile test

To further investigate the grain size effect on the mechanical properties and fracture mechanism, micro tensile tests were conducted and the specimens were elongated till fracture. The tests were conducted on INSTRON micro tester 5848 as shown in Figure

4-3. This equipment can offer ultra-precise displacement control: 20 nm, and can accommodate ultra-thin components. A video extensometer is also installed to ensure the accuracy of stress/strain measurements. The crosshead velocity was 0.02 mm/s applied for all the tests, and each test was repeated three times.

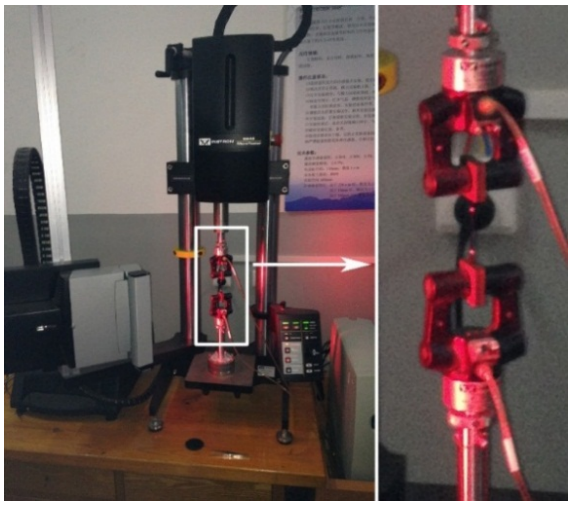

Figure 4-3 INSTRON micro tester 5848 with video extensometer.

4.2.3 SEM observations

After micro tensile test, the fracture surfaces of each *T*/*D* ratio were cleaned by ethanol, and then observed under JEOL 6490 SEM.

4.3 Results and discussion

4.3.1 Effect of *T*/*D* on stress-strain relationship

It can be seen from Figure 4-4 that materials' plasticity increases with the increase of their ratios of *T*/*D*, while the scatter of stress-strain curves profile decreases. When *T*/*D*<1, the average grain size is larger than specimen's thickness, which means most grains involved in the tensile specimens are incomplete. Consequently, due to the lack of grain boundaries and grain boundary corners, concentrated plastic deformation is very difficult to be initiated [133]. This can explain that tensile tests in this group hardly experience plastic deformation. Furthermore, it is clear that this ratio's scatter of stress-strain curves is most obvious in these three groups shown in Figure 4-4(a). This is because without the limitation of grain boundaries, the grain crystal orientation varies and the sliding systems are oriented distinctively when starting an applied stress. In addition, some other deformation modes, such as grain rotation and coordination could change the grain deformation behaviour. Therefore, this kind of grain heterogeneity can contribute to the irreproducible strain-stress relationships. When *T*/*D*>1, the specimen materials can be regarded as polycrystalline aggregate. The quantity of grain boundaries and grain boundary corners will increase largely, which will lead to the appearance of work-hardened grain boundary layers [134]. Once these layers are formed, the stresses within the polycrystalline aggregate will homogenise. The deformation normally take place with the most favorable grain sliding systems, thus the strain-stress curves obtained from this group are the most reproducible which

is reflected in Figure 4-4(c). At the same time, due to the large number of dislocations pile up at grain boundaries and their corners, there is great tendency to activate the plastic deformation, so materials with the ratio $T/D>1$ have the best plasticity comparing to the other two. When $T/D\approx1$, it is notable in Figure 4-4(b) that stress-strain curves are repeated roughly. In this case, there is only one grain in the thickness direction, thus grain matrix deformation and grain boundary sliding can be dominant simultaneously during tests [21]. Plastic deformation is relatively easy to happen because there are grain boundary corners gathering near two sides of thickness direction. However, due to the limitation from thickness direction, grain orientation and coordination cannot occur as easily as they are comparing to materials with $T/D>1$. Therefore, this uncertainty can attribute to the slight scatter of stress-strain curves. According to the results from tensile tests, it is found when the ratio of thickness to grain size is small enough (around 1), the strain-stress relationship on one hand is consistent with classic Hall-Petch relationship as long as average grain size is not scaling down to 10 nm [135]. On the other hand, it becomes very sensitive to the value of the ratio of thickness to average grain size, especially when comparing the plastic deformation occurred with materials' $T/D>1$ to $T/D<1$.

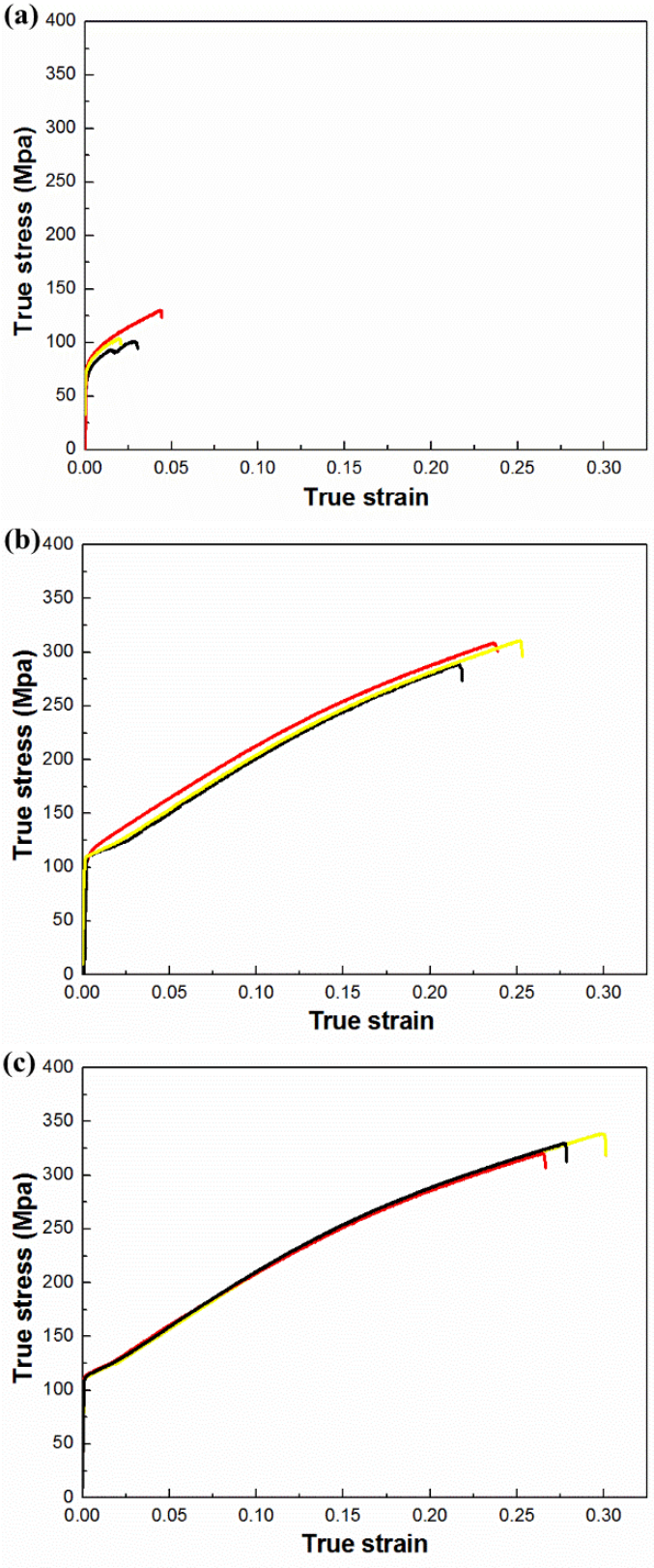

Figure 4-4 Stress-strain curves when different *T*/*D* ratios: (a) *T*/*D*<1, (b) *T*/*D*≈1, and (c) *T*/*D*>1.

4.3.2 Effect of *T*/*D* on fracture behaviour

The fractograph of the tensile-tested samples are shown in Figure 4-5. It is noticeable that different fractograph images were obtained with different ratios of thickness to average grain size. It is found that the number of micro-dimples decreases with the decrease of *T*/*D*. This is consistent with prior studies [16]. The grain boundary fraction in the materials increase with the value of *T*/*D* and because the grain boundaries act as obstacles to dislocation motion, the stresses concentrate at or near grain boundary regions and cause micro-voids and micro-dimples formation consequently in the deformation process. At the same time, micro-dimples and cleavage planes can be found together in all three fractograph, which shows materials can have the mixture of ductile fracture mode and brittle fracture mode, indicating partial plastic deformation occurred during tensile testing. However, a difference can be observed on the fracture surface that the micro-dimples generated when $T/D>1$ is averagely distributed along fracture direction, while when $T/D\approx1$ micro-dimples are mainly focused on a certain limited area, and only a few micro-dimples can be found when $T/D<1$. This phenomenon shows that when more one grain exist in thickness direction, its materials' plasticity is better than that of materials which has just one grain or incomplete one in thickness direction. Inversely, the number of the cleavage planes increase gradually when the ratios of *T*/*D* decrease from larger than 1 to less than 1. When $T/D<1$, cleavage planes take up almost the whole area of fracture surface. This dramatic change can be explained when the grain size approaches to, even overpass the thickness value, the location, size and the orientation of each grain affect the fracture

behaviour significantly. With the decrease of the ratio *T*/*D*, the quantity of the grain boundaries will also decrease, which means when only incomplete grains exist in thickness direction, it forces the grains to have an extremely unfavorable orientation towards the tensile direction, leading to a strong tendency of brittle fracture.

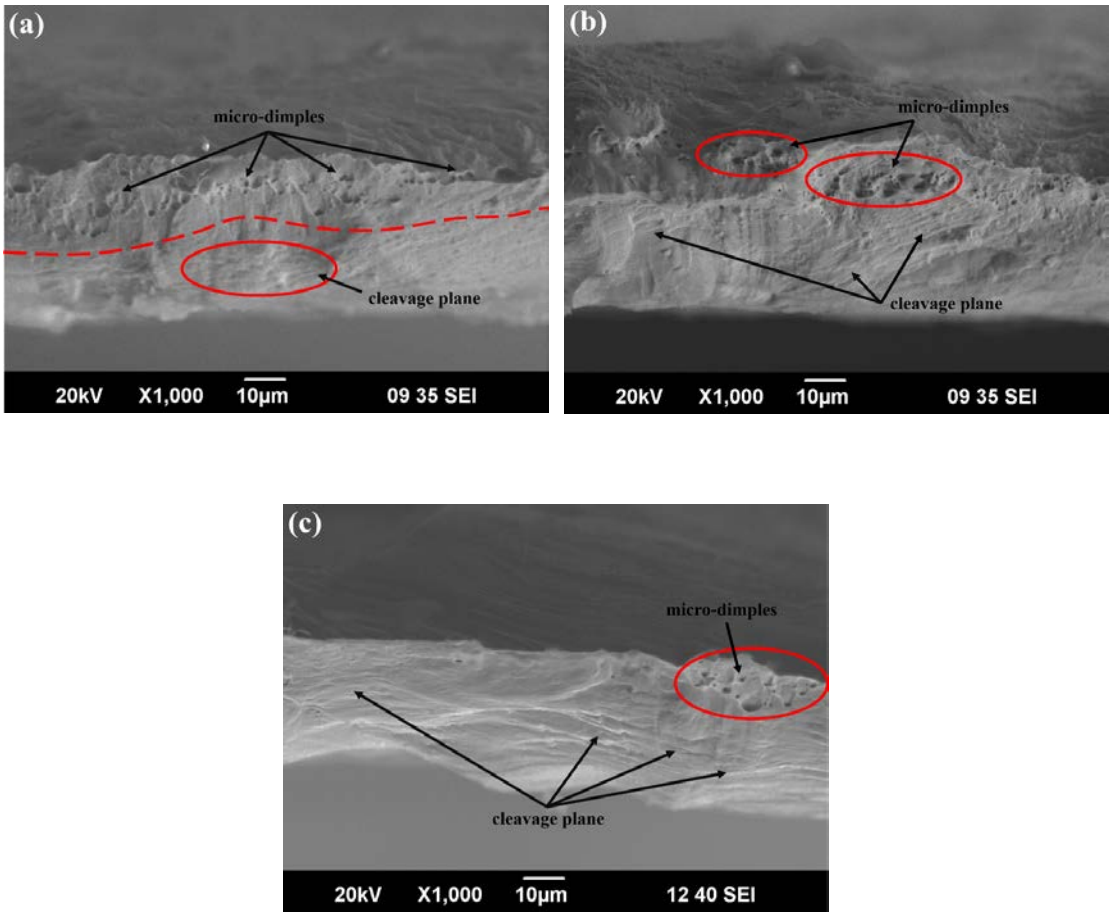

Figure 4-5 Fracture morphology of tested samples (a) *T*/*D*>1, (b) *T*/*D*≈1, and (c) *T*/*D*<1.

4.4 Constitutive model

Normally, the surface layer model is applied when there are several grains in the thickness direction, which means *T*/*D* is comparatively greater than 1. From Figure 4-6, it is illustrated that when *T*/*D*>1, the specimen can be divided into two portions: volume (inner) grains and surface grains.

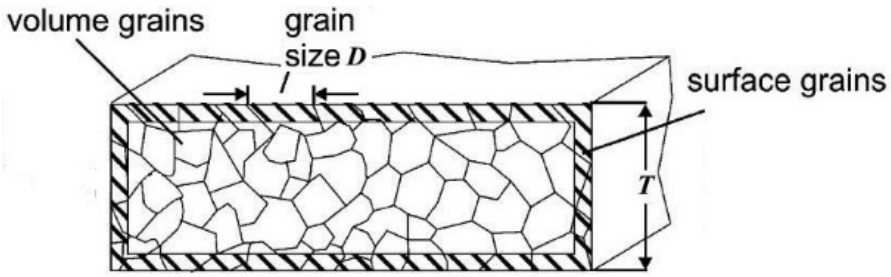

Figure 4-6 The share of the volume grains and surface grains.

However, in our study, the thickness value is close to the average grain size. When the ratio *T*/*D* is slightly greater than 1, there is generally at least one complete grain and a partial grain in thickness direction. So the material still can be regarded as the above two portions. The one grain can be taken as the inner grain of the material, and the other portion can be treated as surface grain. Therefore, the classic surface layer model can still be applicable in this way. The flow stress of the material is expressed as the weighted average of the inner portion' stresses and the surface layer portion's stresses are as follows:

$$\sigma = \eta\sigma_{inner} + (1-\eta)\sigma_{surf} \tag{4-2}$$

where σ is the flow stress of the material, σ_{inner} and σ_{surf} are the stresses of the inner portion and the surface layer of the material respectively. η is size factor to express the fraction of inner portion to the whole material area. It can be calculated based on the following equation [136].

$$\eta = \frac{T-D}{T} \tag{4-3}$$

where *T* is the thickness of the specimen and *D* is the average grain size.

It is notable that this equation cannot be applied when $T<D$ ($T/D<1$), which means the grain size is larger than the strip thickness, only incomplete grains can be observed from the cross section of material. Unlike the previous assumption [22] that the flow stress of surface layer is equal to that of grain interior, the grain boundary strengthening effect cannot be neglected in these two circumstances due to the limited quantities of grain boundaries. Since there is no good way to divide these structures into two portions just like the classic surface layer model, a new constitutive model is proposed in order to better describe these particular material size effects.

4.4.1 Mathematical modelling

The methodology of studying grain size effect on flow stress is based on the composite model developed by Kocks [137] and Meyers and Ashworth [134]. This model has

been proven to be a valid and effective approach to describe the relationship between the flow stress of polycrystalline aggregate and grain size. This composite model assumes that grains are spherical and are composed of grain boundary layers and grain interiors, which is illustrated in Figure 4-7. The idealised representation of the aggregate for $T/D<1$ is shown in Figure 4-8, and the flow stress of the grain aggregate can be expressed as:

$$\sigma_y = A_G \sigma_{fG} + A_{GB} \sigma_{fGB} \tag{4-4}$$

where A_G and A_{GB} are the areal fractions of grain interior and grain boundary respectively. With average grain size D and material thickness T, the grain boundary layers are assumed to have a thickness t.

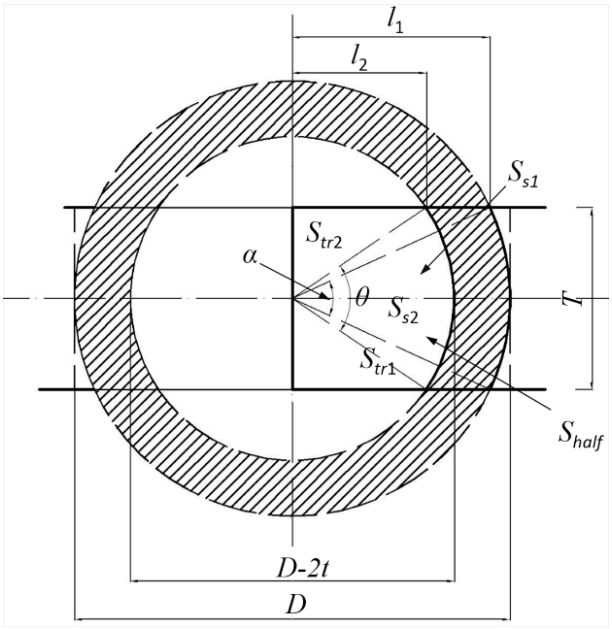

Figure 4-7 Schematic of proportions of grain interior and grain boundary.

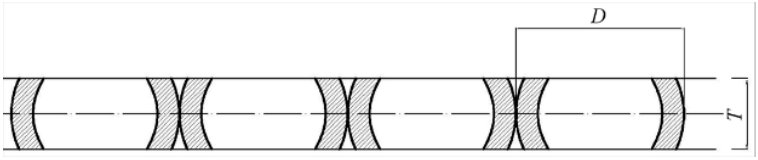

Figure 4-8 Ideal aggregate viewed as composite materials with single incomplete grain in thickness direction.

As it can be seen from Figure 4-8, an idealised spherical grain is limited in thickness direction, and the proportion of grain interior and grain boundary is determined by the thickness value of the material and average grain size, which can be quantified as the ratio of *T*/*D*. Taking the right half grain as an example, the areal fractions are expressed by:

$$A_G = \frac{S_1 - S_2}{S_{half}} \tag{4-5}$$

$$A_{GB} = \frac{S_{half} - S_1 + S_2}{S_{half}} = 1 - A_G \tag{4-6}$$

where S_{half} denotes the area of the right half rectangular, and area S_1 consists of one sector S_{s1} and two triangles S_{tr1}. Similarly, area S_2 is made up of one sector S_{s2} and two trianglesS_{tr2}, and the extra part of the rectangular is treated as grain interior.

$$S_{half} = T \cdot D/2 \tag{4-7}$$

$$S_1 = S_{s1} + 2S_{tr1} \tag{4-8}$$

$$S_2 = S_{s2} + 2S_{tr2} \tag{4-9}$$

The two sectors S_{s1} and S_{s2} can be calculated respectively as:

$$S_{s1} = \frac{\theta\pi\left(\frac{D}{2}\right)^2}{360} \tag{4-10}$$

$$S_{s2} = \frac{\alpha\pi\left(\frac{D}{2}-t\right)^2}{360} \tag{4-11}$$

where θ is the central angle for S_{s1}, and α is the central angle for S_{s2}. They are expressed based on law of cosines by:

$$\theta = \cos^{-1}\left[\frac{2\left(\frac{D}{2}\right)^2 - T^2}{2\left(\frac{D}{2}\right)^2}\right] \tag{4-12}$$

$$\alpha = \cos^{-1}\left[\frac{2\left(\frac{D}{2}-t\right)^2 - T^2}{2\left(\frac{D}{2}-t\right)^2}\right] \tag{4-13}$$

To calculated the areas of triangles S_{tr1} and S_{tr2}, values of l_1 and l_2 need to be obtained. The relationship between the central angles and l_1, l_2 are:

$$l_1^2 = \left(\frac{D}{2}\right)^2 - \left(\frac{T}{2}\right)^2 \tag{4-14}$$

$$l_2^2 = \left(\frac{D}{2} - t\right)^2 - \left(\frac{T}{2}\right)^2 \tag{4-15}$$

Therefore, the triangles' area can be calculated by:

$$s_{tr1} = \frac{1}{2}\frac{T}{2}l_1 \tag{4-16}$$

$$s_{tr2} = \frac{1}{2}\frac{T}{2}l_2 \tag{4-17}$$

Rearranging above equations, the areal fraction of grain boundary and grain interior can be expressed respectively:

$$A_G = \frac{\pi\{D^2\cdot\cos^{-1}(1-2T^2D^{-2})-(D-2t)^2\cdot\cos^{-1}[1-2T^2(D-2t)^{-2}]\}+360T[\sqrt{D^2-T^2}-\sqrt{(D-2t)^2-T^2}]}{T\cdot D/2}$$

(4-18)

$$A_{GB} = 1 - \frac{\pi\{D^2\cdot\cos^{-1}(1-2T^2D^{-2})-(D-2t)^2\cdot\cos^{-1}[1-2T^2(D-2t)^{-2}]\}+360T[\sqrt{D^2-T^2}-\sqrt{(D-2t)^2-T^2}]}{T\cdot D/2}$$

(4-19)

Substituting Equations (4-18) and (4-19) into Equation (4-4), then the new constitutive model the can be expressed by:

$$\sigma_y = \sigma_{fG}\cdot\frac{\pi\{D^2\cdot\cos^{-1}(1-2T^2D^{-2})-(D-2t)^2\cdot\cos^{-1}[1-2T^2(D-2t)^{-2}]\}+360T[\sqrt{D^2-T^2}-\sqrt{(D-2t)^2-T^2}]}{T\cdot D/2}$$

$$+\sigma_{fGB}\left\{1-\frac{\pi\{D^2\cdot\cos^{-1}(1-2T^2D^{-2})-(D-2t)^2\cdot\cos^{-1}[1-2T^2(D-2t)^{-2}]\}+360T[\sqrt{D^2-T^2}-\sqrt{(D-2t)^2-T^2}]}{T\cdot D/2}\right\}$$

(4-20)

According to the previous studies [133], the relationship between average grain size *D* and the thickness *t* of grain boundary can be described as:

$$t = kD^n \tag{4-21}$$

where *k* and *n* are regarded as constants for a specific material. To copper and copper alloy, the correlation between grain size and thickness is:

$$t = 0.133D^{0.7} \tag{4-22}$$

In this way, there are only σ_{fG} and σ_{fGB} are unknown in Equation (4-20) when σ_y is to be solved.

4.4.2 Verification

The flow stresses of grain interior and grain boundary of copper alloy is determined in reference [22] shown in Figure 4-9. It can be seen that the grain boundaries show a much faster rising hardening rate comparing to the gran interiors. This phenomenon has been exemplified by the results of Hirth's research [138]. The grain-boundary regions are shown with pronounced slip activity on two slip systems, which leads to a much higher hardening rate than the grain interiors.

Substituting the values of flow stresses of grain interior and boundary from Figure 4-9 and Equation (4-22) into Equation (4-20), then the flow stress σ_y can be obtained. Figure 4-10 shows the comparison of the calculated and the experimental true stress-strain curves which were obtained under the condition of specimen' T/D>1. A good agreement between the calculations and experiments [20] illustrates that the developed constitutive model is capable to predict the relationship between stress and strain when the value of material's thickness/average grain size is less than 1 which can be frequent in microforming.

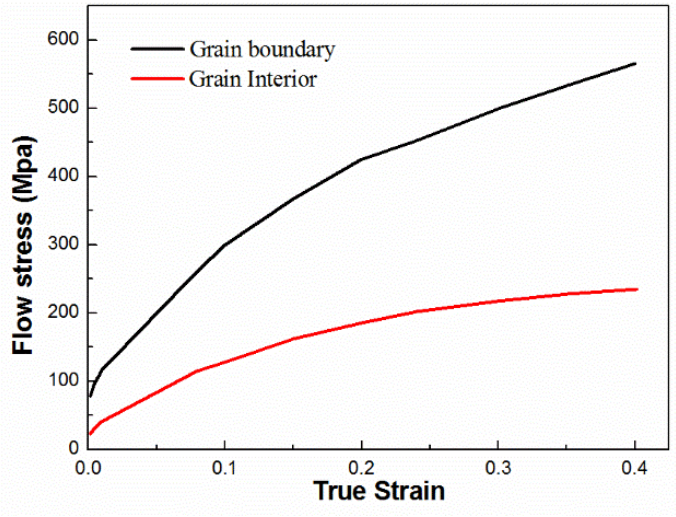

Figure 4-9 Flow stresses of grain interior and boundary of pure copper and copper alloy sheet foil.

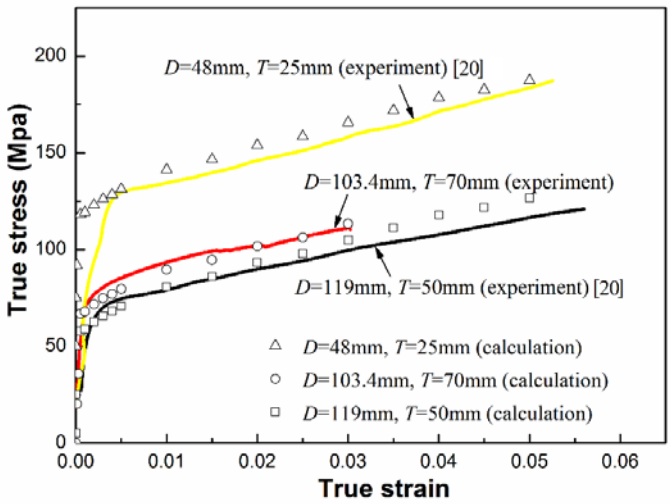

Figure 4-10 Comparison of calculated and experimental stress-strain curves when $T/D<1$.

4.5 Summary

In this chapter, the influence of the ratio of thickness to average grain size on micro scale materials' deformation and fracture behaviour was investigated. The ratios are chosen to be around 1, but in three different ranges: $T/D>1$ (1.23), $T/D\approx1$ (1.07) and $T/D<1$ (0.68). The following conclusions are obtained:

(1) Plastic deformation increase with the increase of T/D, and this is extremely obvious when comparing the plastic deformation occurred with materials' $T/D<1$ to $T/D>1$. This shows that the deformation behaviour is very sensitive to the value of the ratio of thickness to average grain size when the range is around 1.

(2) The number of micro-dimples decreases with the decrease of T/D, while the number of cleavage planes increase with it. When $T/D>1$, micro-dimple can be found are averagely distributed in fracture surface, which shows a great tendency of ductile fracture. However, large area of cleavage plane means that brittle facture has a strong tendency to be occurred when $T/D<1$. Therefore, $T/D\approx1$ can be regards as the divide of ductile fracture and brittle fracture, and this ratio becomes a decisive factor to materials' fracture mode.

(3) When $T/D<1$, there is only single incomplete grain in thickness direction, and classic surface layer model cannot be applied in this situation. A new

constitutive model is developed based on composite model with the consideration of $T/D<1$. Comparison was made between simulation values and experimental ones, and a good agreement verified the validity of the developed model.

Chapter 5 Grain size effect on texture evolution of annealed and micro V-bended phosphor bronze foil

5.1 Introduction

The micro parts which are mostly made from nonferrous alloys, such as copper alloy and aluminium and magnesium alloy are widely being applied [24]. The increasing demand of micro-scale products for high accuracy and high quality has also inspired the development of microforming technology. In micro-scale world, it is common known that size effects are playing a significant role in influencing materials' mechanical properties, texture, microstructures, and formability and so on. In practice, the most versatile technique to present grain size effect is to obtain a given recrystallised grain size via heat treatment after which a scale factor (specimen dimension/grain size) can be achieved.

Prior to this investigation, several researches have been conducted to explore the role that grain size effect plays in texture evolution in conventional and micro forming process with various nonferrous alloys. Park et al. [27] found out that tensile properties of the friction stir welded magnesium alloy AZ61 were strongly affected by crystallographic orientation distribution and grain size. Valle et al. [28, 29] carried out ECAP and large-strain hot rolling experiment on magnesium alloy to conclude that

both texture and gran size have a great influence on work hardening as well as ductility. Llanes [30] found a much more pronounced cyclic hardening and high saturation stresses is linked to some certain fibre textures in coarse-grained copper rather than fine-grained copper. Furthermore, Hoseini et al. [32] proposed that after ECAP processing, the grain size of pure Ti has no impact on the corrosion resistance when the (0002) planes parallel to the surface. Janssen et al. [31] found that the ratio of thickness to grain size can be viewed as a clue for flow stress when texture in samples were similar. Yin et al. [33] concluded that in Mg AZ31 alloy gran size of 0.8 μm or below can eliminate large yield asymmetry caused by $\{10\bar{1}2\}$ tensile twinning by tensile, compressive and ECAP testing, and Guo et al. [34] also found that the work-hardening rate of AZ31 alloy decreases as grain size decreases, but is irrelevant to (0002) pole intensity. Mabuchi et al. [37] proposed that the grain size dependence is related to the distribution of grain boundary misorientations, and Leffers and Juul Jensen [38] described that both texture and microstructure changed dramatically when a brass plate was severely bent during rolling. Zhang et al. [35] studied the improvability of texture of AZ31B Mg alloy and found that texture control has more effect on bendability at lower temperature, and Kaneko and Eguchi [36] also verified the decisive effect of texture on bendability. Song et al. [40] explained these results in-depth by investigating texture evolution during bending process. Sutou et al. investigated Cu-Al-Mn-based shape memory alloys on damping properties [41] and on pseudoelasticity [39] by studying the effect of grain size and texture. Barnett et al. [42] found that the grain size is critical when identifying twinning-slip transition by compressing extruded samples.

Vaidya and Sinha [43] expressed the electromigration response of thin film aluminium by a function of grain size and the degree of {111} fibre texture.

In the present study, heat treatment experiment was firstly carried out on phosphor bronze foils to obtain different scale factors which were expressed as thickness (T)/average grain size (D) >1, <1 and ≈1. Micro V-bending was then conducted three times for the specimens of each ratio. The microtexture analyses of annealed and micro V-bended specimens were carried out by employing an automated high-resolution EBSD system. The texture characterisations during micro V-bending process were revealed systematically by comparing the texture data from the annealed specimens to that from the bended ones with the consideration of the ratio T/D.

5.2 Experiments

5.2.1 Heat treatment

Phosphor bronze C5191 foil from cold rolling with thickness 70 μm was employed to conduct this research.

Total six specimens measuring 2 mm (length) ×1 mm (width) ×0.07 mm (thickness) were cut by wire-cut EDM from as-received materials, and then these specimens were subjected to various heat treatments to acquire different grain sizes. To accomplish the

aim of different grain size effect ratios, the materials were annealed in Ar air protection condition with the same temperatures but different holding times before furnace cooling. The anneal conditions are the same as that in Chapter 4 since it has been tested that these heat treatment can achieve the target grain size. The microstructures of three different grain sizes in thickness direction are shown in Figure 5-1, as it also illustrates the crystallographic orientation information in terms of inverse pole figure (IPF) which will be discussed in the next section. It can be seen that the grain size increases with holding time under the same annealing temperature. After annealing, the specimens were divided into two groups: one group was straight samples for recrystallisation texture acquisition, and the other was for micro V-bending experiment and then to be scanned for grain orientation map of bended specimens.

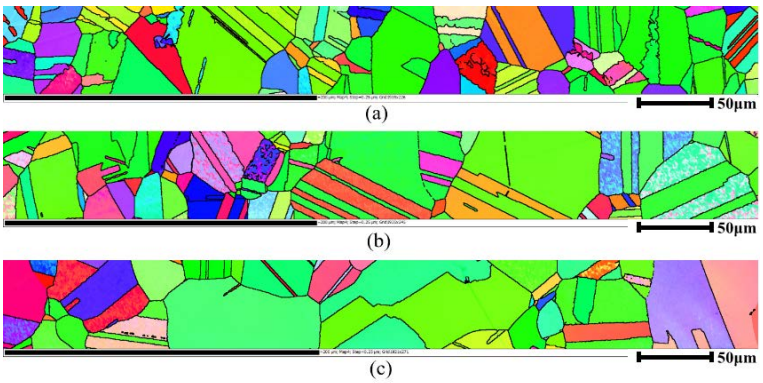

Figure 5-1 IPF maps of annealed phosphor bronze foils: (a) T/D >1, (b) $T/D \approx 1$, and (c) T/D <1.

5.2.2 Micro V-bending experiment

To investigate the relationship between the ratio *T*/*D* and the change of the distribution of crystallographic orientations during bending process, micro V-bending was conducted with the annealed specimens on the desk-top servo press machine DT-3AW. This equipment has position accuracy within ± 2 μm and a set of self-designed bending models are employed respectively as shown in Figure 5-2. The machine can provide 30 KN maximum force and ±0.002 mm guidepost position accuracy. In addition, micro V-bending tooling set (punch and female die) was high-precisely manufactured from D2 tool steel with very good dimensional stability (±2 μm) to conquer the difficulty of positioning the bending set

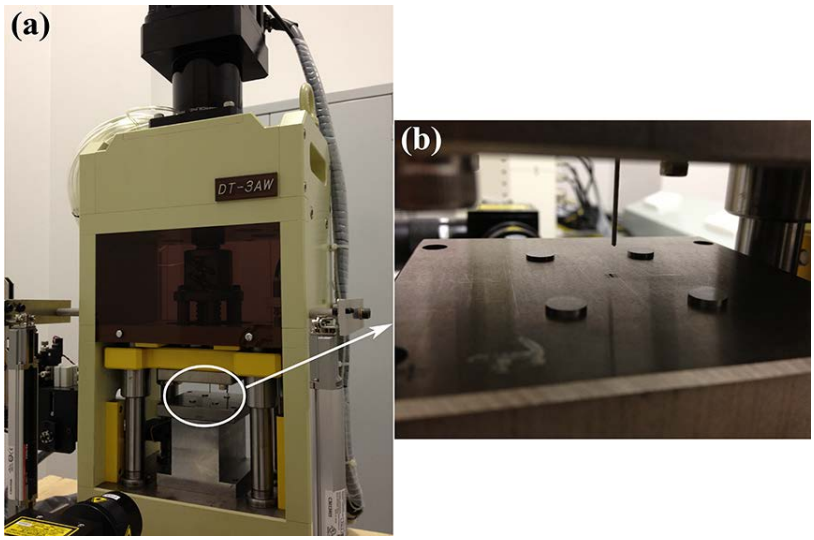

Figure 5-2 Micro V-bending set (b) in Desk-top servo press machine DT-3AW (a).

The delicate punch and die were manufactured with 90 degree convex-concavely, and these two elements were separately installed into the upper and lower moulds. The micro punch was fabricated with high dimensional accuracy of ± 1 μm by micro-grinding, and the other pertinent geometric parameters are: die gap = 0.8 mm, die depth = 0.5 mm, punch corner radius = 0.01 mm, punch stroke = 0.43 mm. Before conducting the experiment, the surfaces between the punch and die were well lubricated by machine oil. The micro V-bending test was performed at room temperature and annealed specimens were placed in the middle of die and bended with punch speed of 0.1 mm/s. Figure 5-3 illustrates the micro V-bending process from loading to bending, and then unloading. Tight shots of these three processes were taken and key components: punch, specimen and die were enlarged in ellipses.

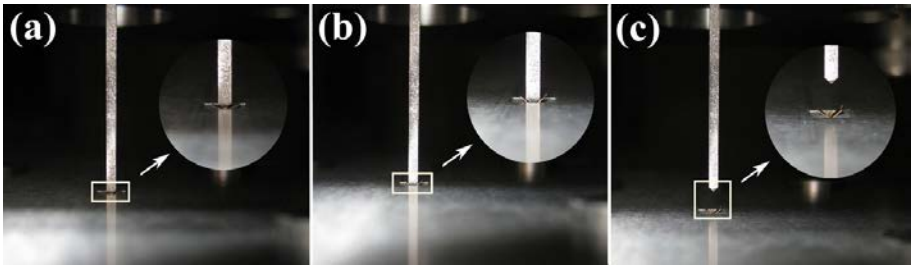

Figure 5-3 Micro V-bending process: (a) loading (b) bending (c) unloading.

5.2.3 EBSD observations

After annealing, the specimens were divided into two groups: one group was straight samples for recrystallisation texture acquisition, and the other was for micro V-bending

experiment and then to be scanned for grain orientation map of bended specimens. The cross section of the rolling direction (RD) - normal direction (ND) sections for straight (annealed) and bended specimens with three different *T*/*D* values were polished mechanically. Due to the small geometry and the softness of specimens, an ion beam milling system (Leica EM RES102) was adopted to finalise polishing, qualifying the surface of specimens for EBSD data acquisition. EBSD mapping was carried out on a JEOL-JSM7001F field emission gun (FEG) scanning electron microscope (SEM), fitted with a Nordly-II (S) camera at 15kV, ~5 nA and 10 mm working distance. A step size of 0.25 μm was maintained constant for all the maps. In all maps, a minimum of 3 pixel was used to identify grain structures and misorientations (θ) less than 2° were disregarded. The orientation distribution functions (ODFs) were calculated via HKL Channel-5 and the α-fibre intensities were determined with a 10° deviation from the ideal skeleton line. The grain size in IPF maps was measured independently of the twin grains according to the standard of ASTM.

5.3 Results and discussion

5.3.1 Effect of *T*/*D* on recrystallisation texture

The ideal texture components of face centred cubic (f.c.c.) materials which are involved in this research are shown schematically in Figure 5-4 and Table 5-1 with φ_2 =0°, 45° ODF sections. The colouring orientation maps of annealed phosphor bronze

foils with different *T*/*D* values are illustrated in Figure 5-1, Moreover, φ_2 =0°, 45° ODF sections of the selected areas in Figure 5-1 with increasing *T*/*D* factors are given in Figure 5-5. The variations in the intensity (*f*(*g*)) of the individual texture components along the various fibres are illustrated in Figure 5-6. It is well established that grain orientation is related to strain-induced recrystallisation, but that is not the point in this research since the material used is a final product and no more plastic strain will occur before heat treatment. With respect to phosphor bronze (f.c.c.) which is classified as low stacking fault energy (SFE) material [139], the annealing process resulted in the development of the characteristic α-texture and {110} texture which is parallel to the transverse direction (TD).

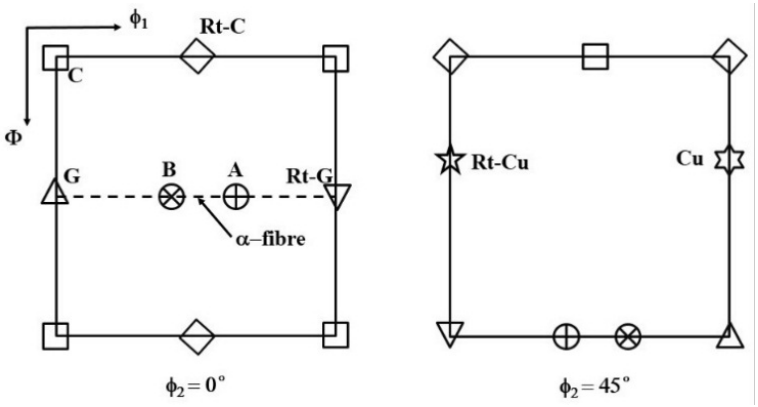

Figure 5-4 A schematic representation of the important texture components in f.c.c. material.

Table 5-1 Euler angles and Miller indices for common texture components in f.c.c. materials.

Texture component	Symbol	Euler angles			Miller indices	Fibre
		ϕ_1	Φ	ϕ_2		
Cube(C)	□	45	0	45	{001}<110>	-
Goss(G)	△	90	90	45	{110}<001>	α
Brass(B)	⊗	55	90	45	{110}<112>	α/β
A	⊕	35	90	45	{110}<111>	α
Rotated Goss(Rt-G)	▽	0	90	45	{011}<011>	-
Rotated Cube (Rt-C)	◇	0/90	0	45	{001}<110>	-
Copper (Cu)	✡	90	34	45	{112}<111>	β
Rotated Copper(Rt-Cu)	☆	0	35	45		–

As seen in Figure 5-5(a), the texture in the material with T/D>1 comprises an α-fibre (from the strong Goss (G) orientation to the strong Brass (B) orientation and the slight A orientation, and then the Rotated Goss (Rt-G) orientation) along φ_1=0-90° at Φ=45°, φ_2=0°. This can be understood according to the study from Hirsch and lücke [140]: with reducing SFE, the intensity of the Cu orientation decreases and the B orientation enhances with a spread towards the G orientation. Among all the components along α-fibre, the most perceptible feature in the material with this scale factor is the threshold of the twinning of Brass as it can be seen that both intensity peaks of B orientation is twinning and moving to the opposite direction. With longer annealing time which means when the ratio of thickness to average grain size is approximately equal to 1, a noticeable decrease in the intensity of the G and Rt-G orientations can be

observed in Figure 5-6. The B orientation slightly shifts towards the A orientation during this stage along with its intensity weakening. Moreover, two completely separate B components shown in Figure 5-5(b) indicate that the twinning of brass texture is developing and the intensity of the A orientation remains almost unchanged. The most distinctive revolution in the material with $T/D<1$ is the significant surge of the A orientation in terms of the intensity which arrives at $f(g)=16.6$. Meanwhile, the twinning of B components is close to finish so that the B orientation totally deviates from its ideal coordinate in Euler space. This results the intensity of the B orientation keeping deceasing along α-fibre. The above intensity variation can be explained in terms of twinning such that the Rt-G and A component have a first order twin relationship with the G/B orientation while the first order twinning of the B orientation leads to crystallogrphically identical variants and explains its retention on recrystallisation [141]. Furthermore, it is noticeable for the disappearance of Rt-Cu component from $T/D>1$ to $T/D<1$. The Rt-Cu is the only recrystallisation component that does not exhibit the first order twin relationship among these texture components, and it has a ~Σ9 (37.3° <101>) relationship with the A orientation and a 30° <111> relationship with the B orientation. This indicates that when the second order of twinning of the B orientation occurs (when $T/D<1$), it may lead to the disappearance of the Rt-Cu component. Similarly, it also explains the surge in A intensity and the plunge in B intensity as the ratio $T/D<1$. It can be seen that the parameter T/D is closely linked to the relationship between the grain size effect and recrystallisation texture components and their intensities.

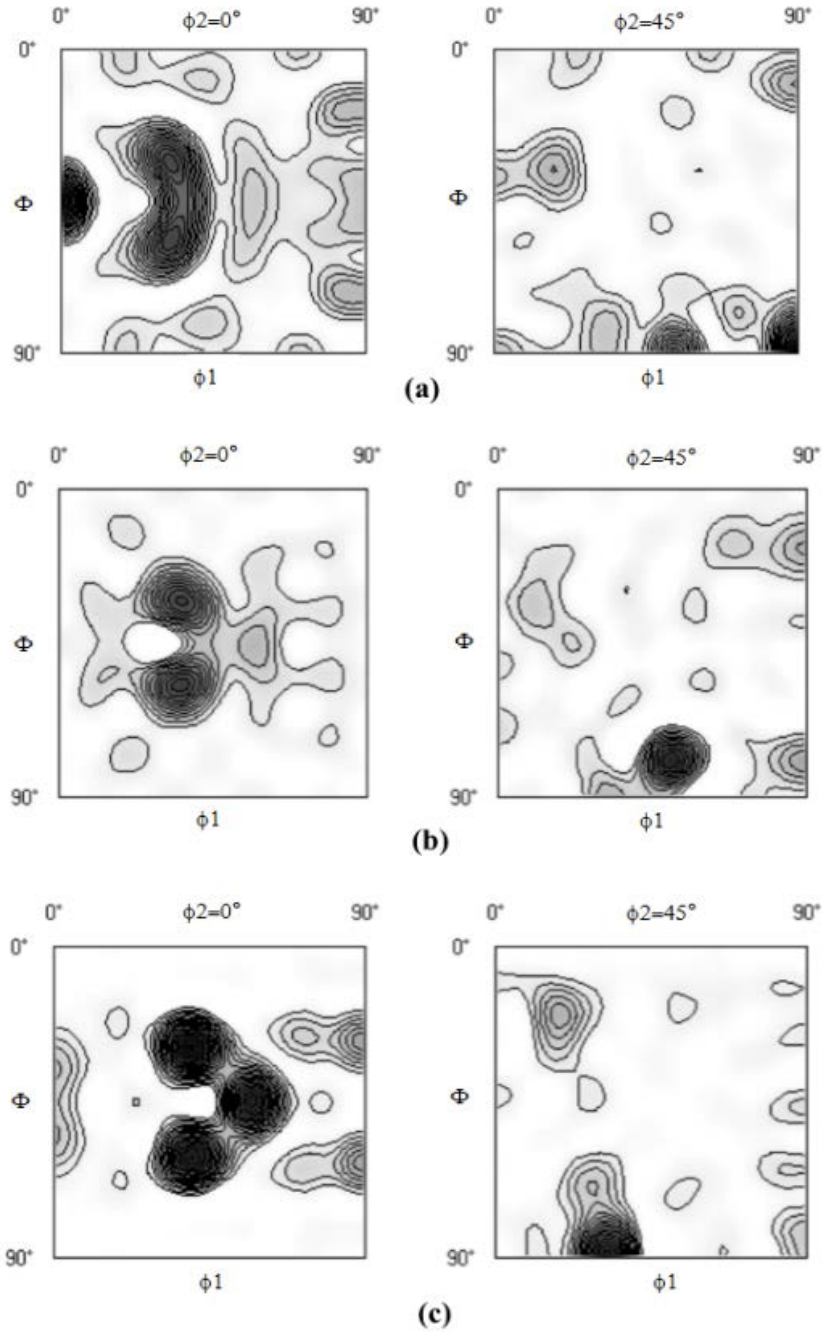

Figure 5-5 φ_2=0°, 45° ODF sections: (a) *T*/*D*>1, (b) *T*/*D*≈1, and (c) *T*/*D*<1. Contour levels = 1×.

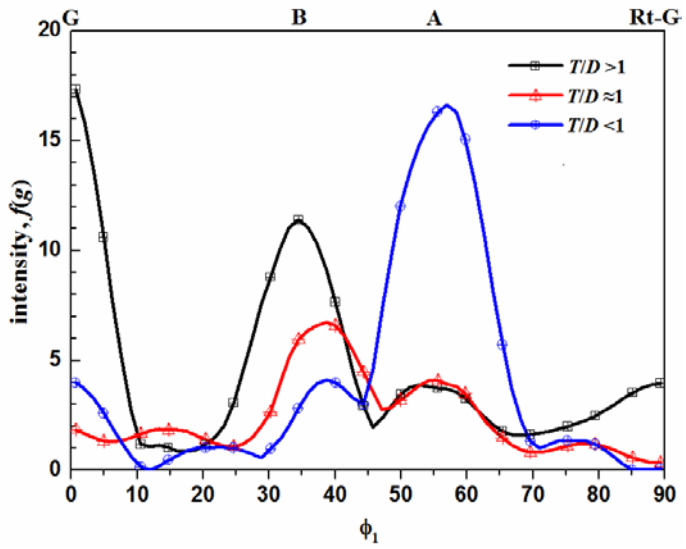

Figure 5-6 The variation in texture components intensity (*f*(*g*)) along α-fibre.

5.3.2 Effect of *T*/*D* on deformation texture in micro V-bending

The IPF maps of the deformation zone for bended specimens are illustrated in Figure 5-7. By comparing Figures 5-1 to 5-7, it can be seen that after micro V-bending the crystallographic orientations change in all three specimens.

More specifically, the material with *T*/*D*>1 has the most obvious colour change, which indicates that this material experienced the most grain rotations during micro V-bending. The material with *T*/*D*≈1 and that with *T*/*D*<1 underwent less and the least grain rotation since the former displays an average degree colour change and the latter has the least colour change. When *T*/*D*>1, there are several grains consisting in the specimen's thickness direction. During the bending process, it is understood that some

grains which reach the critical resolved shear stress, as a threshold value, will firstly initiate dislocation slip and plastic deformation. Since these grains are surrounded by other grains in the specimen due to $T/D>1$ microstructure, their deformation cannot be isolated and arbitrary. This means that the first-initiated grains have to coordinate their rotation and deformation with the adjacent grains to ensure the consistency of the specimen's deformation. On the basis of grain coordination, driven by the applied stress on the specimen and the stress concentration which is caused by dislocation pile-up groups from glided grains, increasing grains in the material will undergo rotations and plastic deformation. When $T/D\approx1$, there is only one complete grain ideally in thickness direction. The above grain coordination will still exist in the bending process, but because of the increase of grain size, the influence of grain coordination deformation will weaken. Conversely, as the grain size is close to the thickness geometry, grains' deformation is likely to be affected by the upper and lower boundaries of the specimen. According to crystallography, the grains' movement can be divided into two patterns according to the direction of the applied force. One is the grain slip movement due to the resolved shear stress along the slip direction, and the other is rotating towards the stress direction because the stress component is normal to slip plane. The most obvious difference between these two microstructures ($T/D>1$ and $T/D\approx1$) when plastic deformation is initiated is that the second type of grain movement will be comparatively limited by the upper and lower specimen boundaries. Figure 5-8 illustrates how the grain which is not located in the vicinity of material boundaries

(when $T/D>1$) can rotate easily while the grain rotation in the material with $T/D\approx1$ will be restricted by the upper and lower boundaries.

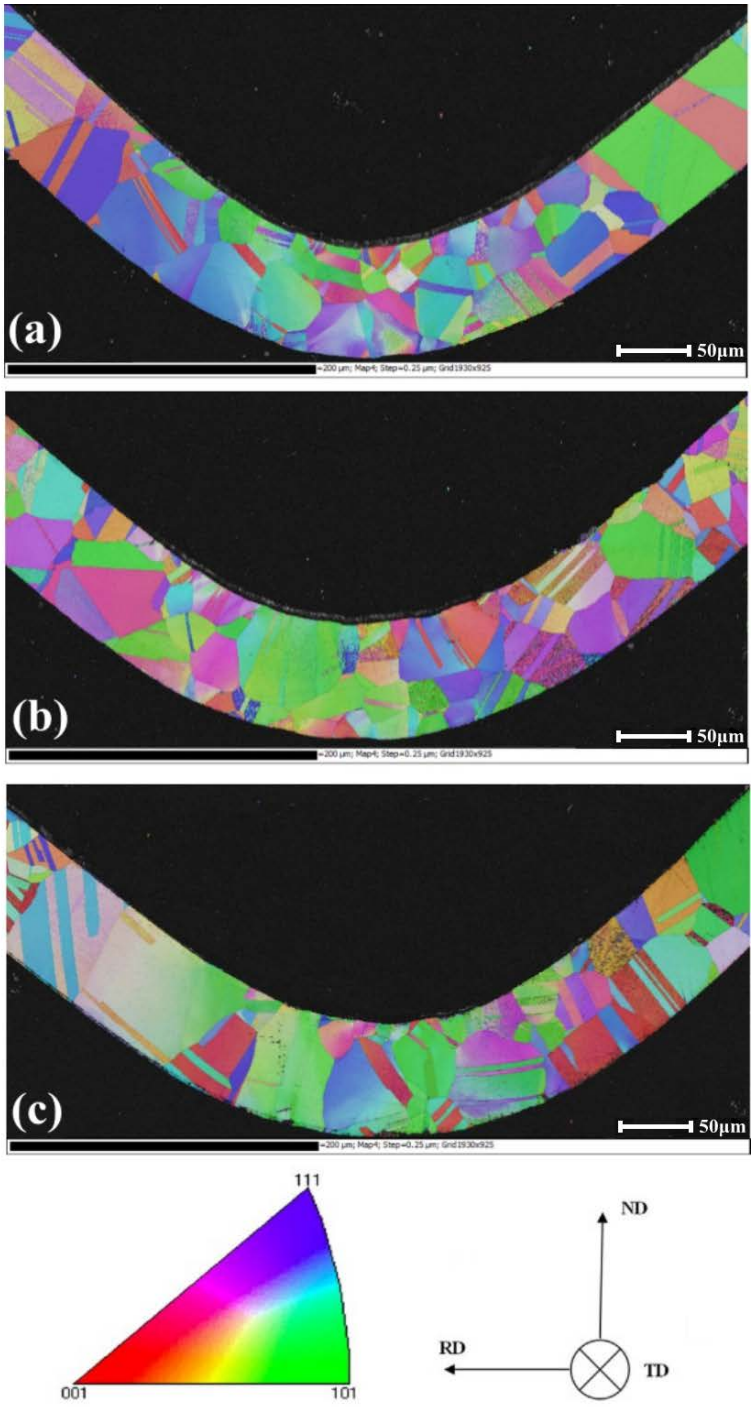

Figure 5-7 IPF maps of the deformation zone for bended annealed phosphor bronze foil: (a) $T/D>1$, (b) $T/D\approx1$ and (c) $T/D<1$.

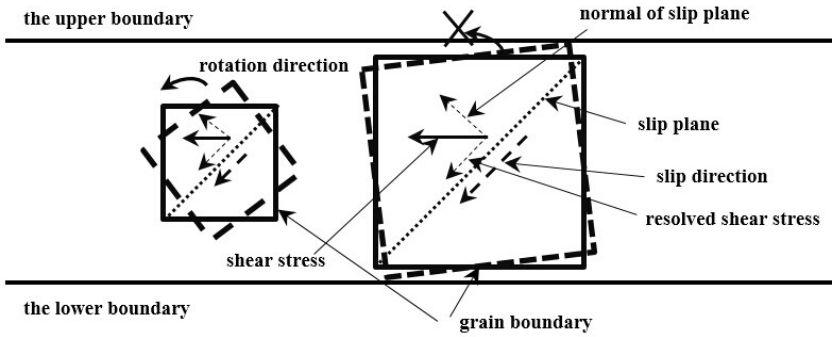

Figure 5-8 Schematic illustration of how grain rotation is restricted by grain boundary.

When $T/D<1$, the grain rotation will be affected and restricted further by the upper and lower boundaries in thickness direction. Moreover, during the micro V-bending process, the movement of slip bands in each grain will not only be terminated in the vicinity of grain boundaries, but also in the vicinity of the upper and lower boundaries, since the size of grains is so large when $T/D<1$ that grain boundaries in vertical direction are replaced by the material's upper and lower ones. This can explain why when grain size is larger than the thickness value, its motion will be severely affected by the material upper and lower boundaries. This impact is more profound than that in the material with $T/D\approx1$, because in the latter condition, the grains have relatively free space to slip and rotate. In the case of bending in this research, the experimental conditions for each T/D sample are completely the same: punch stroke, punch speed, bending angle and bending radius. Even the free edges in the bending specimens are identical. With respect to V-bending, the upper boundary contacts with punch and the lower boundary contacts with V-die. The non-contact areas belong to free boundary, while the contact

areas, no matter with punch or V-die, belong to constraint boundary. Therefore, the only difference in this design is how the size of grain takes its effect on free and constraint boundaries. From Figure 5-9, it can be seen that the punch contacts with a limited number of grains due to the tiny size of punch radius.

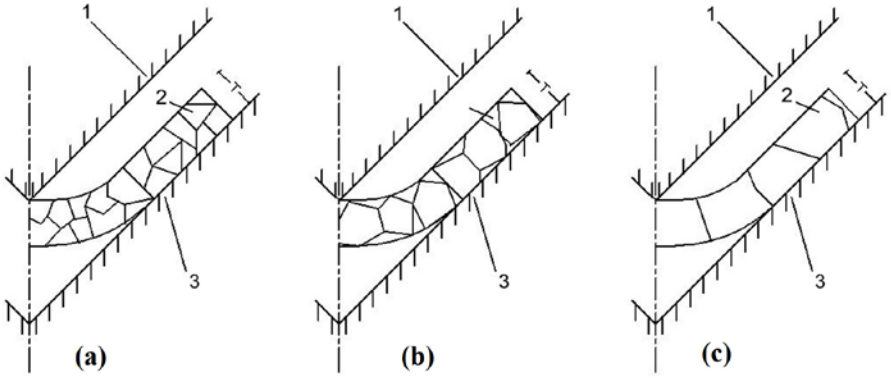

Figure 5-9 Schematic of micro V-bending (a) $T/D<1$, (b) $T/D \approx 1$ and (c) $T/o>1$. 1-punch, 2-grain, 3-V-die.

According to the bending theory, the inside layer will experience compression deformation and tensile strain will occur in the out layer. So grain coordination deformation will become more important on free and punch constraint boundaries with the decrease of grain size. The other issue needs to be considered is the constraint boundary contacting V-die, and the difference on the constraint boundary is the number of grain boundaries which are in touch with V-die. Based on the theory of open and closed lubricant pockets [10], when there are more grain boundaries (from $T/D<1$ to $T/D>1$), there will be more open lubricant pockets, resulting high friction force

between the specimens and V-die. This difference on constraint boundary will increase the corresponding bending force for each ratio specimens.

5.3.3 Effect of *T*/*D* on {110} texture in micro V-bending

The abovementioned statements are based on the relationship between the grain size effect and crystallographic grain rotations during micro V-bending process. With respect to grain orientation in bended specimens, it can be seen from Figure 5-10 (a)-(c) that with *T*/*D* decreases, the area of green colour in the deformation zone increases, which can be interpreted that when the size of grain is close enough to the thickness value or even scale over it, the grain has a tendency to stay its original crystallographic plane under plastic deformation. In order to further confirm this judgment, several points in green area in main deformation zone has been randomly chosen, and their orientations has been illustrated in the corresponding (110) pole figures.

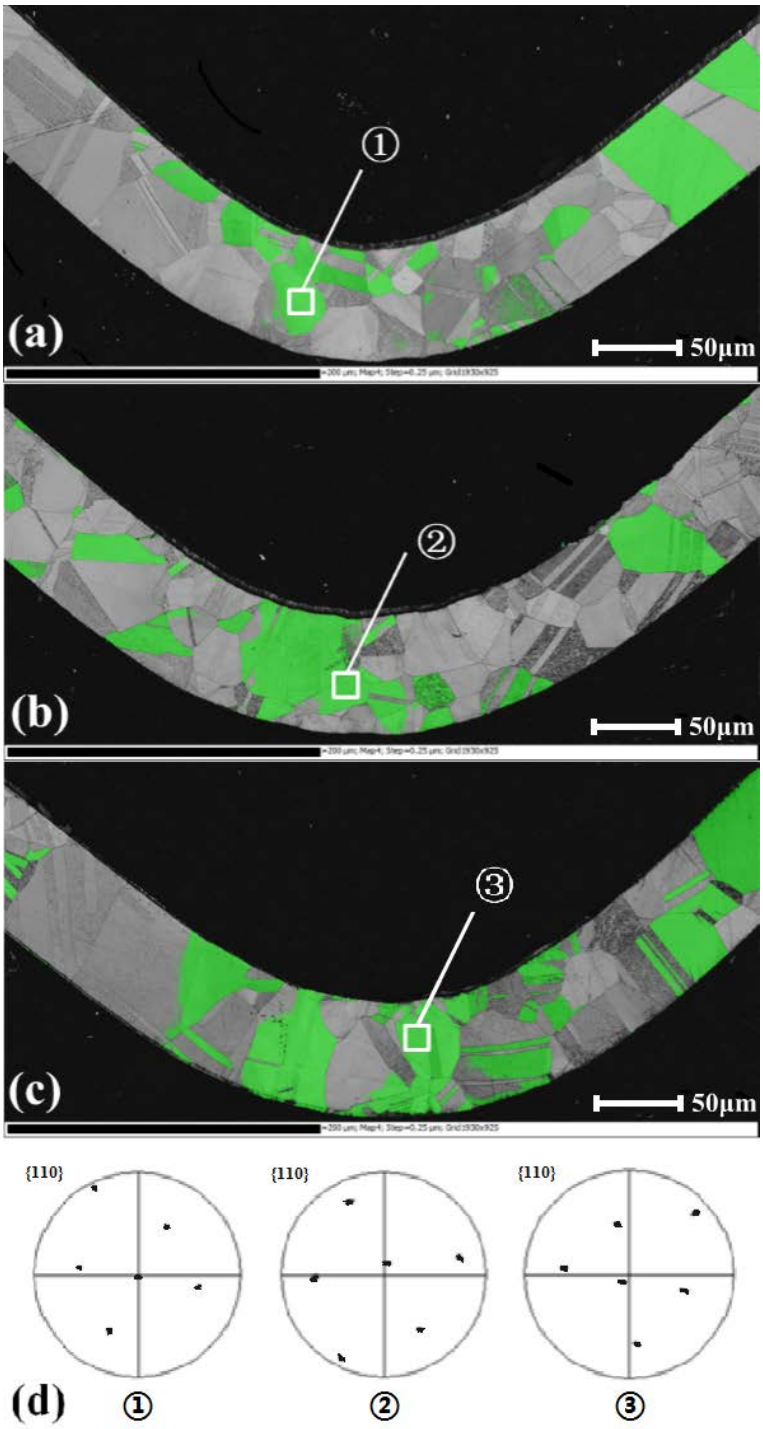

Figure 5-10 {110} portion (green colour) in bended specimens: (a) $T/D>1$ (b) $T/D\approx1$ (c) $T/D<1$ and (d): (110) pole figures for the points labelled 1-3.

It is shown that no matter the value of *T*/*D* is, the grain orientations almost stay at the initial orientations of their annealing textures: the Brass component and the A component, however, the quantity of these components changes. So, it is concluded that for phosphor bronze during micro V-bending, when the ratio *T*/*D* decreases from >1 to <1, the stability of {110} texture increases comparing to other texture components. This judgment can also be explained in terms of crystallography. The slip system for f.c.c. materials is {111}<110>, while the miller indices for the B component and the A component are {110}<112> and {110}<111> respectively. Table 5-2 delivers how the family of crystallographic planes {111} and {110} intersect in which "–" means non perpendicular while "P" represents two planes are perpendicular.

Table 5-2 The intersection of the family of crystal planes {111} and {110}.

	(110)	(101)	(011)	$(\bar{1}10)$	$(\bar{1}01)$	$(0\bar{1}1)$
(111)	–	–	–	P	P	P
$(\bar{1}11)$	P	P	–	–	–	P
$(1\bar{1}1)$	P	–	P	–	P	–
$(11\bar{1})$	–	P	P	P	–	–

It is shown that the half of two crystallographic planes {111} and {110} are mutually perpendicular; therefore, when the resolved shear stress reaches to its critical value and initiates the slip on slip plane {111}, the slip on {110} plane is very hard to be initiated since it is vertical to {111} plane and no resolved shear stress can work on {110} plane.

5.4 Summary

In this chapter, the influence of the ratio of *T*/*D* on texture evolution in annealing and bending for phosphor bronze foil was investigated by EBSD. The ratios were *T*/*D*>1 (1.23), *T*/*D*≈1 (1.07), and *T*/*D*<1 (0.68). The following conclusions are obtained:

(1) Texture evolution during annealing is correlative with the material's grain size effect. The ratio *T*/*D*≈1 can be regarded as a divide for the types of texture component and their corresponding intensities.

(2) Annealing texture evolution of phosphor bronze represents typical α-fibre components, and it is found that when the value of *T*/*D* increases, the intensities of the Goss and Brass components decrease but the intensity of the A orientation increases.

(3) During micro V-bending process, the grain rotation is also found to have a connection with the ratio *T*/*D*. More precisely, when the ratio *T*/*D* decreases, less grains are likely to rotate along with bending process due to grain coordination.

(4) The stability of {110} crystallographic plane increases with the decrease of *T*/*D* from >1 to <1 when undergoing micro V-bending. This can be ascribed that the position of {110} plane is perpendicular to f.c.c. materials' {111} slip plane.

Chapter 6 The implementation of 2D/3D Voronoi diagram in ABAQUS/CAE

6.1 Grain size and grain boundary

When other parameters of a certain microstructure are equal, the grain size will exert a strong influence on the mechanical properties of polycrystalline metal. Specifically, through the interaction between this size factor and the characteristic dislocation length scales in polycrystal, the nature of its plastic flow can be modified. This modification can directly lead to grain size-dependent with respect to plastic flow.

The most widely accepted empirical theory which describes the influence of grain size on the yield stress is the Hall-Petch relationship. It is a linear relationship between the yield stress and reciprocal of the square root of the grain size, and its formula can be expressed as:

$$\sigma_y = \sigma_0 + kd^{-\frac{1}{2}} \tag{6-1}$$

where σ_y is the yield stress and σ_0 is a material's constant for the starting stress for dislocation movement (or the resistance of the lattice to dislocation motion), k is the strengthening coefficient (a constant specific to each material), and d is the average

grain diameter (grain size). The law works on the yield strengths of a wide range of materials, both single phase and poly-phase.

The original theoretical considerations for Equation (6-1) were based on grain boundaries which act as barriers to dislocation motion. Dislocations emanating from a source inside a grain are held up against grain boundaries and form a pileup. As long as the stress concentration from this pileup reaches a critical value, the flow of dislocation will propagate across the boundaries by penetration or the operation of a source in the boundaries or in the neighbour grain.

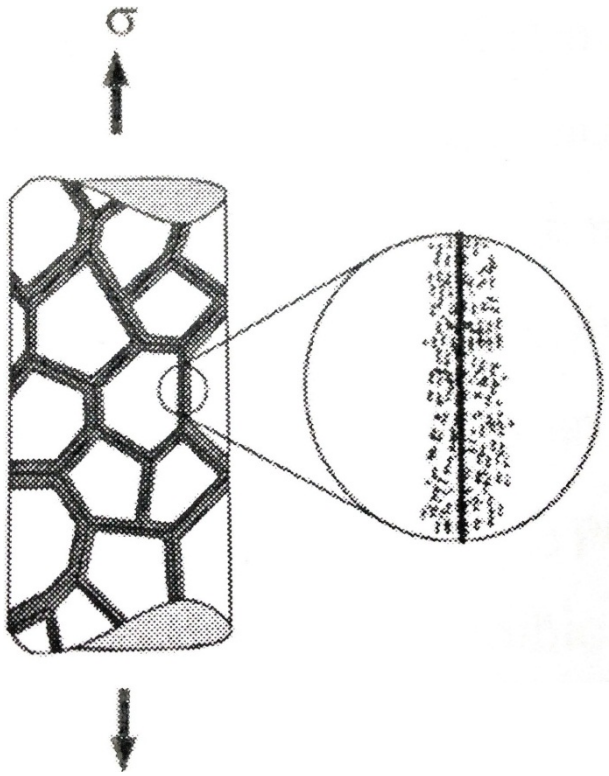

Figure 6-1 Formation of dislocation forests near boundaries as hypothesised in the models [134].

There is extensive experimental evidence that grain boundaries can be regarded as both sources and barriers for dislocations: Carrington and McLean [142] and Douthwaite and Evans [143], and Murr [144] pointed to the fact that in the early stages of plastic flow grain boundaries act primarily as sources of dislocations by means of etch pit and transmission electron microscopy (TEM) respectively. Li [145] and Meyers [134] assumed that at the onset of yielding, grain boundaries act as sources of dislocations and 'pump' dislocations into the grains. As a consequence, as shown in Figure 6-1, forests of dislocation are formed in regions close to the boundaries, and the yield stress is accordingly described as the stress required to move the dislocations through these forests.

6.2 Voronoi diagram

6.2.1 Introduction

As the geometry of a specimen is close to the dimension of grain sizes, there are a small number of grains in deformation area or force area of the specimen where the grain size effect becomes more obvious and significant. This feature leads to grains with different sizes, shapes and orientation resulting in the scatter of the measured mechanical properties. In order to numerically investigate the material heterogeneity in microforming, Voronoi diagram is applied to describe and simulate grain aggregates at steady state.

The Voronoi diagram have been used to conduct research by generating the like polycrystalline material structure [146], and it can subdivide an area or space into convex polygons or cells that fill in the space without overlap. The idea of Voronoi diagram, as an area of computational geometry can date back the 17th century. In his book on the principles of philosophy [147], R. Descartes claimed that the solar system consists of vortices. His illustrations show a decomposition of space into convex regions, each consisting of matter revolving round one of the fixed stars as shown in Figure 6-2.

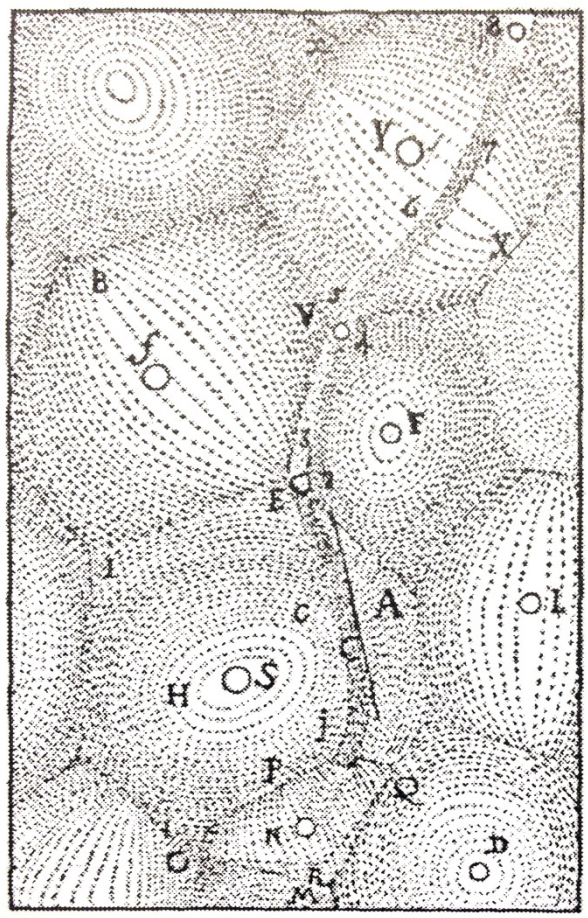

Figure 6-2 Descartes' decomposition of space into vortices.

Descartes did not explicitly define the extension of these regions, but the underlying idea is clear. The concept has independently emerged and proven useful in various fields of science. Different names particular to the respective filed have been proposed and used, such as *medial axis transform* in biology and physiology [148, 149], *Wigner-Seitz zones* in chemistry and physics [150, 151], *fundamental domain* in crystallography [152], and *Thiessen polygons* in meteorology and geography [153, 154]. The mathematicians Dirichlet [155] and Voronoi [118] were the first scholars to formally introduce this concept. They used it to study quadratic forms where the sites are integer lattice points and the influence is measured by the Euclidean distance. The resulting structure has been called Dirichlet tessellation or Voronoi diagram (tessellation), which has now become its standard name.

6.2.2 Definition

S is denoted in the plane by a set of *n* (*n*>2) point sites *p*, *q*, … for points $p=(x_p, y_p)$ and $r=(x_r, y_r)$, let $d(p, r)=\sqrt{(x_p - x_r)^2 + (y_p - y_r)^2}$ denote their Euclidean distance. $\overline{pq}$ is used to denote the line segment from *p* to *q*.

For $p, q \in S$, let

$$B(p,q) = \{r | d(p,r) = d(q,r)\} \tag{6-2}$$

be the bisector of *p* and *q*. *B*(*p*, *q*) is the perpendicular line through the centre of the line segment $\overline{pq}$.

It separates the half plane

$$D(p,q) = \{r | d(p,r) < d(q,r)\} \tag{6-3}$$

Containing p from the half plane $D(p, q)$ containing q. We call

$$VR(p,S) = \bigcap_{q \in S, q \neq p} D(p,q) \tag{6-4}$$

the Voronoi region of p with respect to S. Finally, the Voronoi diagram of S is defined as follows:

$$V(S) = \bigcup_{q \in S, q \neq p} \overline{VR(p,S)} \cap \overline{VR(q,S)} \tag{6-5}$$

By definition, each Voronoi region $VR(p, S)$ is the intersection of n-1 open half plane containing the site p. Therefore, $VR(p, S)$ is open and convex. Different Voronoi regions are disjointed and Figure 6-3 shows an example of 2D Voronoi diagram.

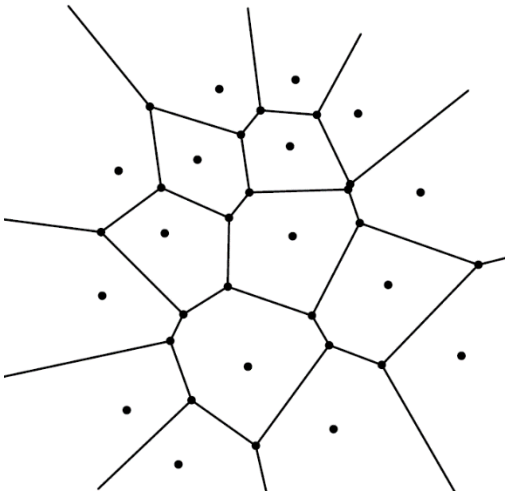

Figure 6-3 A 2D Voronoi diagram.

The common boundary of two Voronoi regions belongs to *V*(*S*) and is called a Voronoi edge, if it contains more than one point. If the Voronoi edge e borders the regions of p and q then $e \in B(p,q)$ holds. The endpoints of Voronoi edges are called Voronoi vertices which belong to the common boundary of three or more Voronoi regions.

There is an intuitive way of looking at the Voronoi diagram *V*(*S*). Let *x* be an arbitrary point in the plane. We prescribe a circle, *C*, at *x* and let its radius grow, from 0 onwards. At some stage the expanding circle will, for the first time, hit one or more sites of *S*. Now there are three different cases.

Case 1: if the circle *C* expands from *x* hits exactly one site, *p*, then *x* belongs to *VR*(*p*, *S*). If *C* hits exactly two sites *p* and *q*, then *x* is an interior point of a Voronoi edge separating the regions of *p* and *q*. If *C* hits three or more sites simultaneously, then *x* is a Voronoi vertex adjacent to those regions whose sites have been hit.

Case 2: A point *p* of *S* lies on the convex hull of *S* if its Voronoi region *VR*(*p*, *S*) is unbounded.

Case 3: The Voronoi diagram *V*(*S*) has many edges and vertices. The average number of edges in the boundary of a Voronoi region is less than 6.

In general, a triangulation of *S* is a planar graph with the vertex set *S* and straight line edges, which is maximal in the sense that no further straight line edge can be added without crossing other edges. Each triangulation of *S* contains the edges of the convex hull of *S*. its bounded faces are triangles, due to maximality. We call a subset of edges of a triangulation a tessellation of *S* if it contains the edges of the convex hull, and if each point of *S* has at least two adjacent edges. Consequently, two points of *S* are joined by a Delaunay edge if their Voronoi regions are edge-adjacent. Therefore, *DT*(*S*) is the graph-theoretical dual of *V*(*S*), realised by straight line edges. Figure 6-4 gives an example that the Voronoi diagram *V*(*S*) is drawn by solid lines and *DT*(*S*) by dash lines.

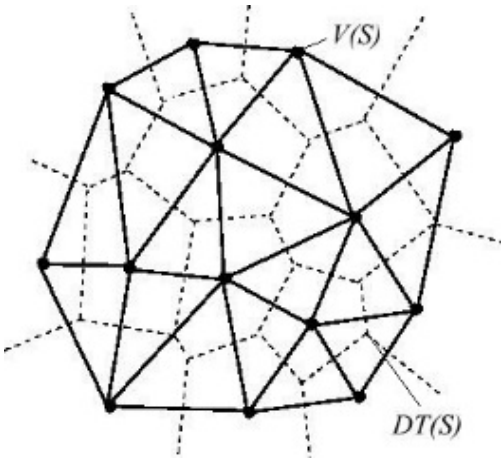

Figure 6-4 Voronoi diagram and Delaunay tessellation.

6.3 Implementation in ABAQUS/CAE

In this section, a comprehensive 2D and 3D Voronoi diagram generation method in commercial FE software ABAQUS/CAE is stated. This implementation is conducted with the assistance of other two sets of software: MATLAB and Python, and the related functions are expressed.

6.3.1 2D Voronoi diagram in ABAQUS/CAE

For implementing a 2D Voronoi diagram into ABAQUS pre-processing, the first job is to plot the 2D Voronoi diagram in MATLAB. The algorithm for generating Voronoi diagram is very sound in MATLAB, and the syntax we chose to generate a Voronoi diagram is *voronoi*(*x*, *y*) which plots the bounded cells of the Voronoi diagram for the points *x*, *y*. For obtaining the topology of the Voronoi diagram, for example, the vertices for each Voronoi cell, the syntax [*V*, *C*] = *voronoin* ([*x*, *y*]) is used. To any point *p*, it has at least one neighbourhood which belong to the *p*'s Voronoi cell, which means that any domain *V*(*p*) cannot be null. This declares that to a Voronoi diagram from *n* unique points,

- *V*(*S*) contains *n* domains exactly, and parts of these domains are infinite.
- Every vertex in Voronoi diagram goes through at least three circle centres of seeds, and these circles do not contain any other seeds.
- Seeds are decisive to the position and size of Voronoi cells.

To recrystallised metal microstructure, the grain shape can be considered as equiaxed which is consistent with the topology structure of Voronoi cells. Therefore, the key issue for successfully generating grain-like Voronoi diagram in MATLAB is seeding. Here the seeding method is stated in the following.

(1) Assuming that a Voronoi diagram consists of $i \times j$ ($i, j \geq 1$) Voronoi cells with average 'grain' size D. So the length of the plane can be calculated as $D \times i$, and its width is $D \times j$ where $i, j \geq 1$.

(2) Dividing the plane into $i \times j$ equal rectangles, and seeding at the centre of each rectangle. The coordinates of the seeds can be expressed as

$$x_{(i,j)} = \frac{D}{2} + (j-1) \times D \tag{6-6}$$

$$y_{(i,j)} = \frac{D}{2} + (i-1) \times D \tag{6-7}$$

(3) Taking r which is named as shape control factor as an arbitrary value between -1 and 1, the expression of r is:

$$r = 2 \times \mathrm{rand}(1,1) - 1 \tag{6-8}$$

where rand(1, 1) is a MATLAB syntax distributing pseudorandom number valued between 0 and 1. So the new coordinates of the seeds can be expressed as

$$x_{(i+1,j)} = x_{(i,j)} + r \times \frac{D}{2} \tag{6-9}$$

$$y_{(i,j+1)} = y_{(i,j)} + r \times \frac{D}{2} \tag{6-10}$$

Then in this way the seeds' coordinates can be obtained.

The key point in seeding process is that changing the coordinates of seeds to change the shape of Voronoi cells by assigning different *r* values. Otherwise, the seeds will be just distributed in the centre of each rectangle and grain shape-like Voronoi cells cannot be generated. Figure 6-5 shows the Voronoi diagram plotting in MATLAB when *r* is assigned with different value ranges.

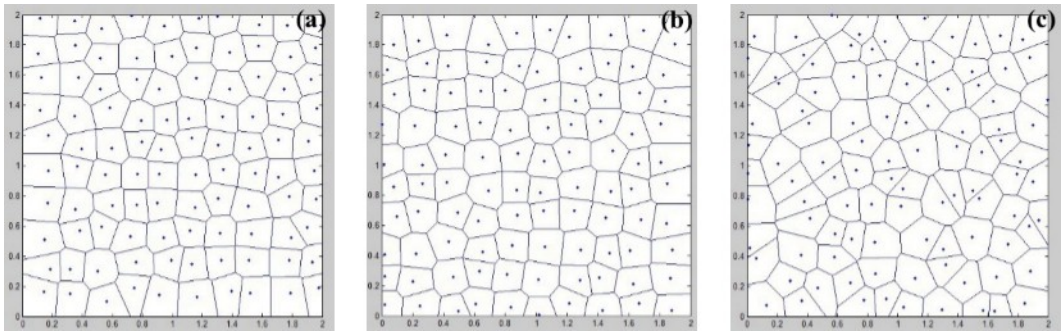

Figure 6-5 2D Voronoi diagram under different r values: (a) -1<*r*<0, (b) 0<*r*<1 and (c) -1<*r*<1.

It can be seen that, when *r* values from -1 to 0 and from 0 to 1, the plots are similar to normal rectangles and the shape factor does not take much effect. However, when the value of *r* is extended from -1 to 1, it increases the irregularity of the Voronoi diagram which can be clearly visualised in MATLAB plotting.

After plotting 2D Voronoi diagram in MATLAB, the coordinates of every vertex in each Voronoi cell can be obtained. Two groups of information are essential for copying the Voronoi diagram in MATLAB. One is the coordinates of all the vertices in the

diagram, and the other is the indices of connecting each vertex for every Voronoi cell. More specifically, each Voronoi cell can contain several vertices, and this topology information can be found when the syntax [*V*, *C*] = *voronoin* ([*x*, *y*]) is adopted. *V* delivers the Voronoi vertex information, and is an *m*-by-*n* array of the *m* Voronoi vertices in *n*-dimensional space, and each row corresponds to a Voronoi vertex. *C* is a vector array where each element contains the indices into *V* of the vertices of the corresponding Voronoi cell. Figure 6-6 illustrates a Voronoi cell marked with the indices of vertices, and it can only be plotted successfully when the vertices are connected in a clockwise or anti-clockwise order. Otherwise, for example, if vertex 20 was connected with vertex 79 instead of 5 or 34, the cell can be an error.

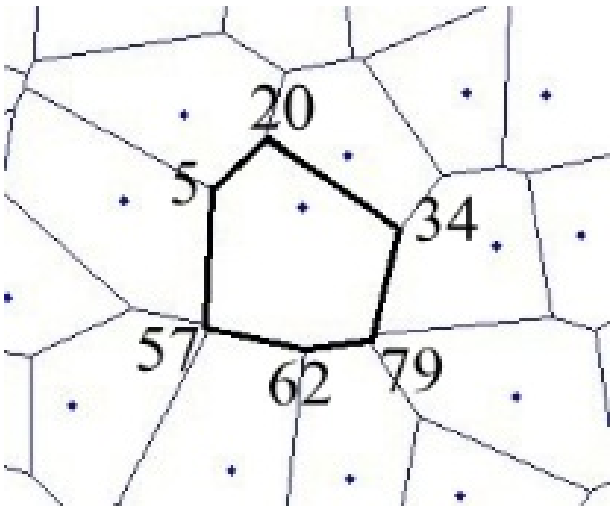

Figure 6-6 2D Voronoi cell with indices.

Therefore, when programming Python script language, it is significant to confirm that each vertex should be linked in the given orders provided by MATLAB. In this study, Python script files are generated through MATLAB programming, and a function has been created in MATLAB to finish this task. In this function, all the Python script statements should follow Python's syntax and semantics since it is going to be run as a script file in ABAQUS/CAE.

The technique used here is that loops have been applied to record all the vertices coordinates in the diagram, and to every two vertices which can be connected through lines, they are renumbered to fit in the loops. The programming of the loops in MATLAB is as follows.

```
for i = 1:size(LineX_Coords,2)
    LinePts(i,1)=LineX_Coords(1,i);
    LinePts(i,2)=LineY_Coords(1,i);
    LinePts(i,3)=LineX_Coords(2,i);
    LinePts(i,4)=LineY_Coords(2,i)
end
```

This is a loop for renumbering the coordinates of connectable vertices stored from *V*.

```
for i = 1:size(LinePts,1);
fprintf(fa_prg,'%s\n',
['mySketch.Line(point1=(',num2str(LinePts(i,1)),',',num2str(LinePts(i,
2)),'),point2=(',num2str(LinePts(i,3)),',',num2str(LinePts(i,4)),'))']
);
end
```

This is a loop for programming Python script language to connect the vertices according to the indices in *C*.

Moreover, when all the edges in Voronoi diagram are draw, it is necessary to draw a rectangle to include all the Voronoi cells and to limit the boundary of the specimen because the side Voronoi cells contain edges with infinite length. Last but not the least, every Voronoi cell should be partitioned into a face which ensures that Voronoi cells are not simply frames but faces with boundaries. If Voronoi cells were just frames connected from edges, mechanical properties cannot be assigned into Voronoi tessellations in ABAQUS pre-processing.

Other Python statements for acting as ABAQUS/CAE script language can be found in Python related reference books, so these contents will be skipped here. Figure 6-7 shows 2D Voronoi diagrams with different size Voronoi cells (grain sizes) in the same specimen dimension.

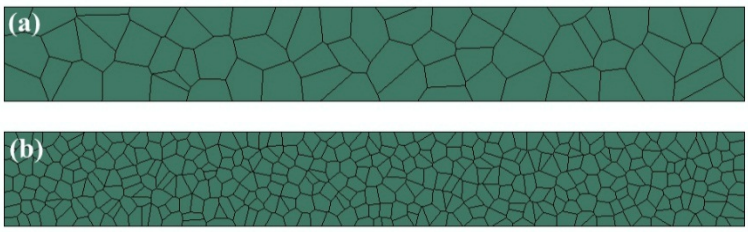

Figure 6-7 Different quantity Voronoi cells in a fixed specimen dimension (a) 66 grains, and (b) 375 grains.

6.3.2 3D Voronoi diagram implementation in ABAQUS/CAE

The general flow path for 3D Voronoi diagram implementation in ABAQUS/CAE is evolved from that for 2D one. Therefore, it is necessary to point out the differences between these two methods. On the surface, although one more dimension is added, and one more parameter needs to be considered, some details for 3D Voronoi diagram are completely distinctive to the method for its 2D counterpart. In this section, a comprehensive method for 3D Voronoi diagram implementation in ABAQUS/CAE is stated.

Firstly, a 3D Voronoi tessellation is generated by means of programming in MATLAB. As 2D Voronoi diagram can be plotted according to the build-in function *voronoi*(*x, y*) in MATLAB itself, the programming code for 3D counterpart is evolved and modified based on this function, and can make the size of Voronoi cells controllable. For 3D Voronoi diagram implementation, *voronoi*(*x, y*) is no longer applicable since it is for

2D plotting. Instead, [*V*, *C*] = *voronoin* ([*x*, *y*, *z*]) is firstly used to obtain the coordinates of 3D Voronoi cells' vertices and the indices of connecting every vertex for each cell. *x*, *y*, *z* are the coordinates of seeds in *X*, *Y*, *Z* direction, and the distance between two adjacent seeds is the grain size of physical specimen. In visualisation, another function *convhulln*(*Verts*) is used. *Verts* represent the whole coordinates of the vertices in 3D Voronoi diagram. To 3D visualisation, this function returns to the indices of the *Verts* points that comprise the facets of the convex hull of these points, so it actually computes the vertices of the facets that make up the Voronoi cell. Then *patch* function is applied to generate the figure in MATLAB plotting. Figure 6-8 displays 1 mm×1 mm×1 mm cubic 3D Voronoi diagram with 0.1mm Voronoi cell size (grain size) plotted in MATLAB.

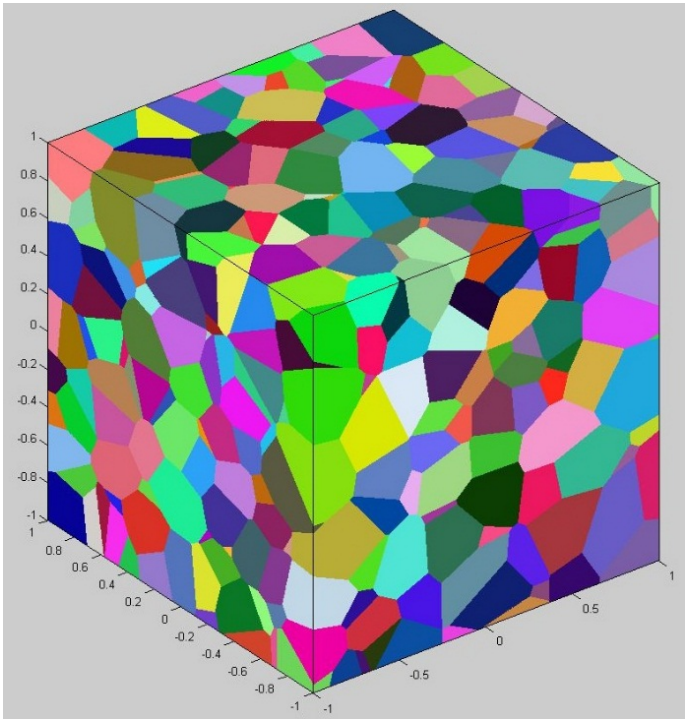

Figure 6-8 3D Voronoi diagram in MATLAB.

Secondly, extracting the coordinate values of the entire vertex from the 3D Voronoi tessellation plot, and then stores all these data into a Python file. This file is also generated by means of Matlab programming, and the codes, like 2D Voronoi diagram implementation, should be consistent with Python's syntax and semantics because this file will work as a script file in ABAQUS/CAE. However, more than the 2D counterpart, the vertices should be connected to edges in the given indices, and the edges are connected to make up facets. Last, these facets are combined together to generates the Voronoi cells while facets can directly represent Voronoi cells in 2D plotting.

Finally, entering GUI of ABAQUS/CAE, and clicking 'file' then choosing 'run script'. From the popped-up window, the generated Python file which is suffixed by 'py.' can be traced and selected according to the route which had been set up in the second step. Python programming language runs as scripting language that can be embedded in ABAQUS/CAE to achieve less time consuming, less repetitive and more flexible operation. Instead of human operation in pre-processing, Python scripts can promptly and compactly execute commands in ABAQUS/CAE through typing given statements and expressions. Especially for the multiple Voronoi tessellations implementation, Python has a natural advantage when inputting a large number of coordinates values and connecting them repetitively. Figure 6-9 illustrates how ABAQUS scripting interface commands interact with the ABAQUS/CAE kernel.

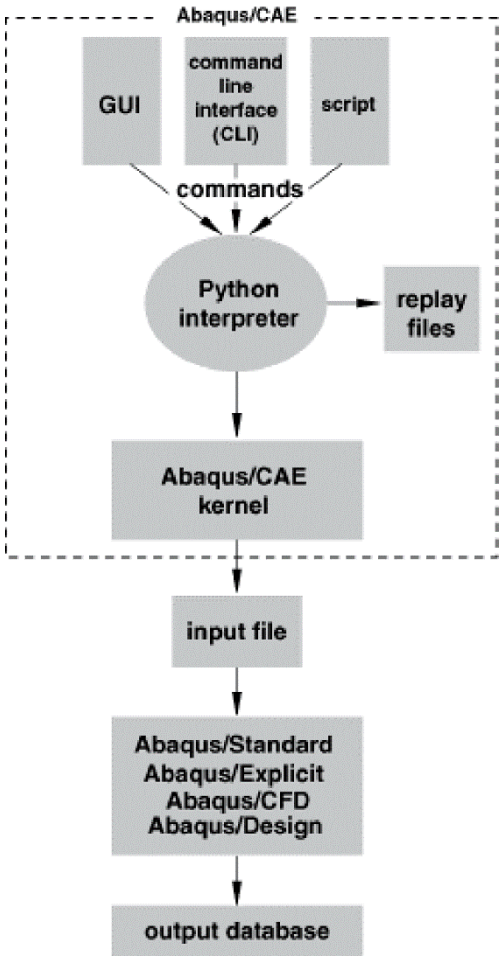

Figure 6-9 ABAQUS scripting interface commands and ABAQUS/CAE [156].

If there were syntax mistakes, then debugging until the file can be fully interpreted by ABAQUS/CAE which delivers that Voronoi diagram can be completely duplicated from the 3D plot in MATLAB. Voronoi tessellations are especially suitable in ABAQUS/CAE to compose experimental specimens (to realise polycrystalline aggregate) in the microforming FE models. Figure 6-10 illustrates a specimen ($T/D<1$) which is computationally divided into multiple grains and each single grain contains grain interior and grain boundary.

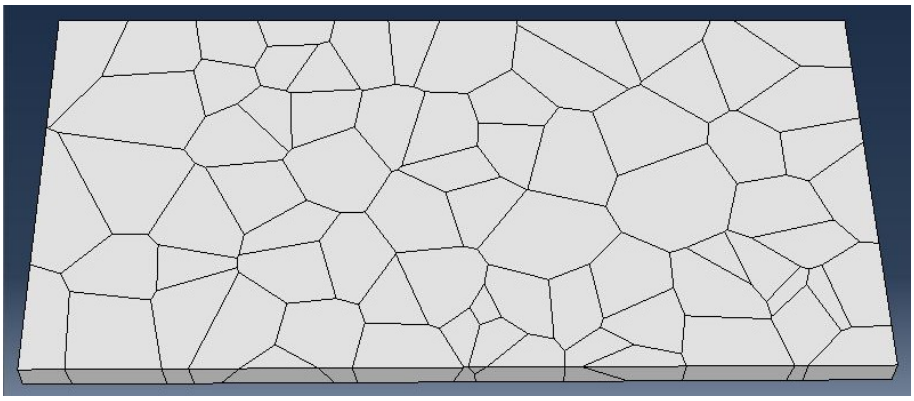

Figure 6-10 Voronoised specimen in ABAQUS/CAE.

6.4 Grain heterogeneity

After the implementation of Voronoi diagram in ABAQUS/CAE, the virtual specimens which are made up of Voronoi diagram are equipped with a certain number of like-grains structures. According to the previous research [157], the grain interior and grain boundary can be modelled as a single body. This is because stress incompatibility at grain boundary will disappear when grain interior is undergone plastic deformation. Nevertheless, in microforming simulation which is featured with inhomogeneity and heterogeneity, no matter 2D or 3D Voronoi diagram, each grain involved in the specimen needs to be employed with a particular property to make it inhomogeneous to each other.

It is acknowledged that different orientations, sizes and shapes of different grains have a momentous impact on inhomogeneous deformation behaviour and the scatter of

material mechanical properties. The methodology adopted in this study to investigate the grain inhomogeneity is to distinguish the inhomogeneity of the mechanical property of each grain (each Voronoi tessellation) involved in a whole specimen. This method is easy to conduct and is to understand, and it requires tensile test results (stress-strain curves) and the concept of normal distribution. Normally, the scatter of stress-strain curves for different grains can be seen in Figure 2-45.

It is shown that each grain mechanical property corresponds to different grain. In macro level, the interest of mechanical property tests, for example tensile test, is the mean stress-strain curve, which is normally obtained by averaging three test results. Generally, these three test results are not repeated, and it is accepted that this scatter of experimental results is caused by errors coming from measurement, observation and operation [18, 158, 159]. However, in microforming, for any grain involved in a polycrystalline sample, it has a unique stress-strain curve which may be higher or lower than or approximately the same as the sample's averaged stress-strain curve. This proposes two different points of views on the scatter for test results. In macroforming, the scatter comes from human errors, while in microforming, the scatter comes from and represents the grain heterogeneity itself. Theoretically, different grains in one sample actually have different mechanical properties, but this feature will normally be ignored when considering macroscopic conventional processing. However, it should never be neglected in microforming since each grain mechanical property can influence uniquely and greatly on deformation behaviour, especially for grains which

are located in the deformation zone of specimens. For instance, mechanical properties of the grains in bending deformation zone will have a significant impact on springback. However, the grain in side areas will have much less impact on it since these grains are hardly deformed during bending.

To the blue stress-strain curve in Figure 6-11, it is believed that when a tensile test result goes to the blue curve, it is the effect of all the grains in the specimen work together. Therefore, there must have some grains' mechanical properties are higher than the blue curve's value, and some other grains must own lower mechanical properties. Here comes a problem: how can we confirm the range of grain mechanical properties. At this stage, it is difficult to find the exact range of grain mechanical properties for a certain specimen. However, a close answer can be acquired. In previous studies, the probability density function was used to study how to obtain discrete grains mechanical properties from measured material mechanical properties. The function was formulated in the research of [18]:

$$f(\sigma,\varepsilon)=\frac{1}{S(\varepsilon)\sqrt{2\pi}}e^{-\frac{1}{2}\left[\frac{\sigma(\varepsilon)-\sigma_m(\varepsilon)}{S(\varepsilon)}\right]^2} \tag{6-11}$$

where the standard deviation $S(\varepsilon)$ was described as:

$$S(\varepsilon)=\sqrt{\frac{\sum_{j=1}^{t}\left[\sigma_j(\epsilon)-\sigma_m(\epsilon)\right]^2}{t-1}} \tag{6-12}$$

and the mean flow stress $\sigma_m(\varepsilon)$ was illustrated as:

$$\sigma_m(\varepsilon)=\frac{\sum_{j=1}^{t}\sigma_j(\varepsilon)}{t} \tag{6-13}$$

where t is the total number of tensile samples, and $\sigma_j(\varepsilon)$ is the jth tensile test result.

Based on these four test results in Figure 6-11 (fine lines), the mean grain mechanical properties, the upper and the lower bounds of grain mechanical properties (thick lines) can be calculated through Equations (6-12) and (6-13). Finally, seven grain mechanical properties are obtained, and the scatter of grain mechanical properties can be displayed.

In FE simulation, these distinctive grain properties will be assigned into Voronoi tessellations with normal distribution probability by Python scripting. Figure 6-11 shows a specimen which contains grains assigned with seven grain mechanical properties.

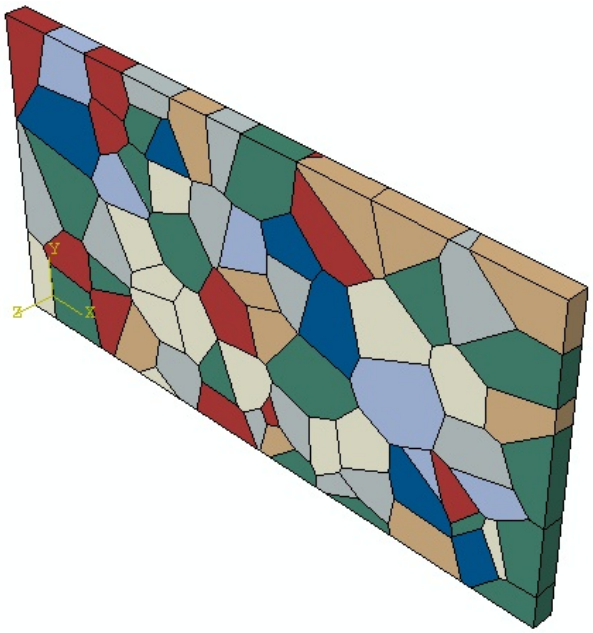

Figure 6-11 A voronoised specimen with seven grain mechanical properties (each colour represents one grain mechanical property).

This figure illustrates that each Voronoi tessellation can be equipped with different and unique mechanical properties in the model, and each Voronoi tessellation will influence deformation behaviour significantly. In this way, the grain mechanical properties combine with Voronoi tessellations, the grain heterogeneity can be achieved in ABAQUS/CAE.

6.5 Summary

This chapter introduces the whole flow path of the implementation of 2D and 3D Voronoi diagrams in ABAQUS/CAE by MATLAB and Python script language. Moreover, the grain heterogeneity and how to quantify it are explained in detail. These preparations differentiate the numerical simulation in microforming from that in conventional forming.

Chapter 7 Numerical study on springback in micro V-bending

7.1 Introduction

The increasing requirement of micro-scale products for high accuracy and high quality has prompted the development of microforming technology research. The metal forming in conventional level has been progressed for centuries and a series of classic knowledge and theories have been established systematically by previous researchers and scholars. Nevertheless, it is commonly known that these macro-scale processing theories cannot be straight applied to micro-scale world because of “size effect”. Vollertsen et al. [12] categorised size effects and discussed the occurring problems in microforming related to size effects, they also focused on the relationships between size effects and formability and forming processes [13]. Engel and Eckstein [6] and Geiger [11] have both reviewed many research projects targeting the problems which were associated with miniaturisation.

With respect to an inevitable phenomenon: springback, it is important to investigate how size effect and springback will influence each other mutually during forming process. Springback theories of sheet metal forming have also been studied and

developed by various experimental and computational techniques and procedures, among which V-bending, U-bending and cylindrical bending are the widest range performed because the result of springback is normally obvious and can be easily gauged. For V-bending researches, Tekıner [52] investigated springback compensation in terms of different materials and thickness during V-bending. Zhang et al. [53] studied experimentally on the deformation mechanisms of V-bending by deformable punches and dies, and concluded that the selection of punch material is of great importance for a given work material. Li et al. [93] considered the change of Young's modulus in plastic bending process and confirmed the accuracy of hardening mode and springback precision.

It is noticeable that while the scale of specimens downsizes to micro-level, the parameters which may not be that significant in conventional bending begin to play a vital role in influencing the accuracy of bending, in another way, determining the springback effect. Gau et al. [24] investigated the springback behaviour via three points bending. They observed that springback is related to the ratio of sheet thickness to grain size. Similarly, Liu et al. [22] studied size effect and springback by developing a constitutive model based on surface layer model. Since size effect is significantly important in micro-world, the grain heterogeneity of specimen has to be considered regardless of conducting physical experiment or modelling. The grain heterogeneity can be described by the scatter of grain behaviours which can be attributed to different grain sizes, shape and orientations. When building models, this scatter can be

employed into single virtual grain, and different grains will affect separately and mutually during the simulation process. The scatters of grain mechanical properties were investigated comprehensively in previous research by Chan et al. [18] and Lu et al. [112].

In recent years, the Voronoi diagram was introduced to generate polycrystalline aggregate. This method subdivides a space tessellation into Voronoi polyhedral, which is similar to morphogenetic process of nucleation and growth from random seeds [160]. Voronoi tessellation has an extensive application in scientific researches: Aurenhammer [120] introduced the algorithm and its mathematical applications on Voronoi diagrams detailedly. Okabe et al.[119] fully described an up-to-date and comprehensive unification of numerous previous literature on the subject of Voronoi diagrams. Schiøtz et al. [135] simulated the reverse Hall-Petch effect by Voronoi construction where grains were produced. Specifically in materials science, polycrystalline microstructures are commonly represented by Voronoi diagram because of its geometric features [161, 162]. However, limited computational research has illustrated the complete 3D Voronoi tessellation realisation when FE model was carried out, since it has been used as a functional approach in polycrystalline materials research.

The main objective of this chapter is to introduce a new FE model for micro V-bending with consideration of polycrystalline aggregate and the grain heterogeneity. The former

is implemented in commercial software ABAQUS/CAE in terms of Voronoi tessellations, and the latter is reflected by the scatter of grain mechanical properties. To obtain related grain size information and grain mechanical properties which are necessary for building up the bending FE model, corresponding heat treatment and micro tensile test have been conducted. Physical micro V-bending experiment is also carried out, and the efficiency of the developed model is verified by comparing the prediction results with the experimental ones. The research objectives in this chapter are inspired from the microstructures, the scattering tensile tests' results in Chapter 4 and the bending final angles in Chapter 5. By applying digital Voronoi diagram program in Chapter 6 and combining it with experimental data, it is promising to explore an appropriate FE simulation method to provide a better prediction for microforming process of metals.

7.2 Experiments

7.2.1 Microstructure of the experimental material

The phosphor bronze C5191 also known as copper tin foil C5191 with thickness 70μm was chosen for micro V-bending experiment

The bending specimens measuring 2×1×0.07 mm were cut by wire-cut EDM from as-received phosphor bronze foil, and then annealed at 650°C for 4h before furnace

cooling. To avoid oxidation, the heat treatment was carried out in Ar air protection condition. The microstructure of specimen along length direction after the annealing treatment are shown in Figure 7-1, and it was obtained through etching with $FeCl_3$ (5g) + HCl (15 ml) + H_2O (85 ml) solution for 2 s. The average grain size is 162.8 μm and it can be seen that the grain size in the direction of foil thickness is restricted, which means only one partial grain exists in thickness direction. The good point is when simulating this microstructure in FE model, and it is easy to observe each grain's influence on whole deformation behaviour since grain size is big enough to distinguish.

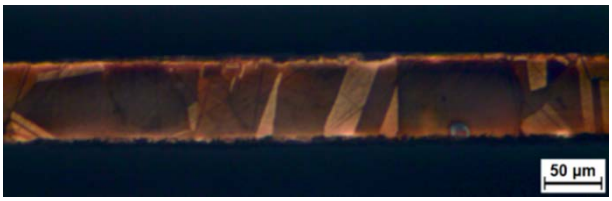

Figure 7-1 Microstructure of annealed phosphor bronze foil.

7.2.2 Micro tensile test

The main purpose of tensile test in this chapter is to gain the stress-strain relationship of the annealed C5191 foil, then to extend the scatter of the material mechanical properties to the scatter of grain mechanical properties. The dimensions of tensile

specimens are identical with that in Chapter 4 (Figure 4-2), and the specimens were also annealed under the same heat treatment process as the bending specimens' one.

Like the tensile tests in Chapter 4, the micro tensile tests were conducted at room temperature on INSTRON micro tester 5848 with the crosshead velocity 0.005 mm/s, and the video extensometer was utilised to record and measure the strain precisely.

7.2.3 Micro V-bending experiment

To investigate the phosphor bronze foil springback phenomenon, the desk-top servo press machine DT-3AW which can afford position accuracy within ± 2 μm and a set of self-designed bending model were employed respectively. They are the same equipment which has been introduced in Chapter 5.

The micro V-bending test was performed at room temperature and annealed specimens were placed in the middle of die and bended with punch speed 0.5 mm/s and punch stroke 0.43 mm, and other experimental parameters are the same with that in Chapter 5. In order to obtain the higher accuracy of the springback effect, the bending test was repeated three times. After the test, each bended specimen was observed and its angle was measured under the VHX-1000 KEYENCE microscope for three times then averaged.

7.3 Experimental results

7.3.1 Material and grain mechanical properties

Based on the research of Lu et al. [112], statistical distribution of grain properties can be divided into seven classes. Among these seven grain properties, the upper and lower bound grain properties and the mean grain properties can be calculated [18]. Therefore, in order to obtain the grains' stress-strain relationship, four groups of true stress-strain curves were obtained as shown in Figure 7-3 after the tensile tests, which are marked as curves 1, 2, 3 and 4, and it is noticeable that they are not repeated. It is generally accepted that this scatter of experimental results is caused by errors coming from measurement, observation and operation [158, 159].

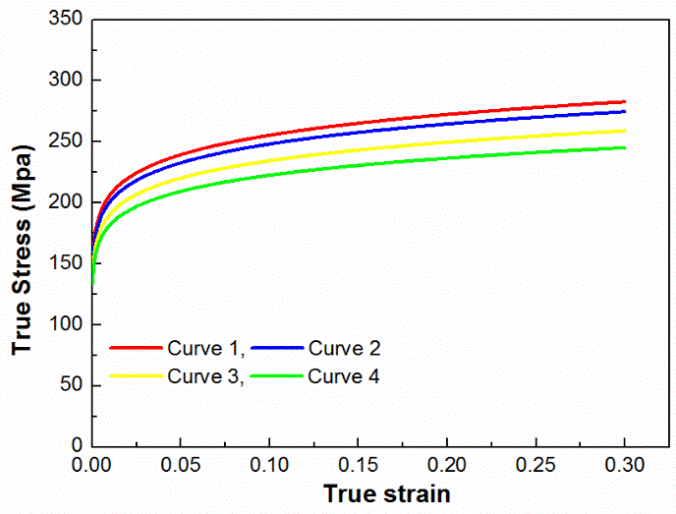

Figure 7-3 Material mechanical properties from tensile tests.

However, in microforming, because the specimen is not regarded as homogeneous material, the minimum unit is no longer a whole piece of specimen but each grain contained in the specimen. The scatter range is determined by grain properties which can be influenced by grain size, orientation, shapes and forming process, therefore, this effect could be attributed to different grain mechanical properties. In other words, if a certain tensile test result goes to curve 1, then it is believed that there must be some grains possess mechanical properties which are higher than curve 1. Similarly, there also must be same grains possess mechanical properties which are lower than and equal to curve 1. All these microscopic grain mechanical properties work together, producing the macroscopic curve 1.

Based on these four test results, the mean grain mechanical properties, the upper and the lower bounds of grain mechanical properties can be calculated through Equations (6-12) and (6-13). Finally, seven grain mechanical properties are obtained and the scatter of grain mechanical properties is displayed in Figure 7-4.

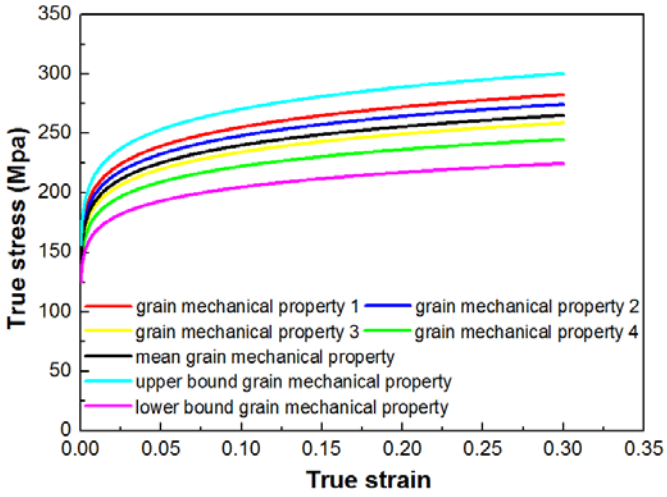

Figure 7-4 Evaluating grain plastic properties from tensile test.

7.3.2 Micro V-bending experimental results

Figure 7-5 shows one bended specimen under microscope VHX-1000 KEYENCE where the springback angle can be measured. It can be observed that obvious springback occurred during unloading process, from bending angle 90° to final one. In order to minimise the possibility of measuring error, each bended specimen were measured three times. The measured angles data from micro V-bending experiment is displayed in Table 7-1.

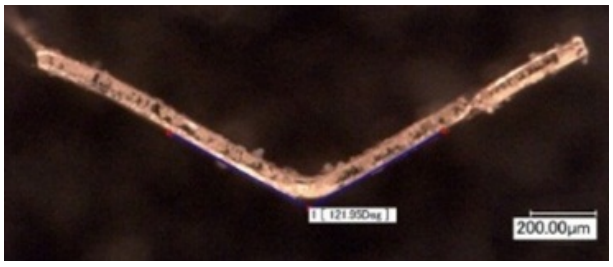

Figure 7-5 Bended angle after springback measured in VHX-1000 KEYENCE.

Table 7-1 Measured and averaged springback angles for bended specimens (degree).

Times of measurement	1st	2nd	3rd	Average
Specimen No. 1	31.60	31.95	32.31	31.95
Specimen No. 2	32.56	31.85	31.63	32.01
Specimen No. 3	30.94	30.74	31.09	30.92

7.4 FE simulation

7.4.1 Voronoi tessellation implement in ABAQUS

In this study, a comprehensive 3D Voronoi diagram implementation has been conducted to simulate specimens in micro V-bending. The detailed methodology for how to implement Voronoi diagram into ABAQUS/CAE has been described in Chapter 6. Here, the corresponding application is focused on.

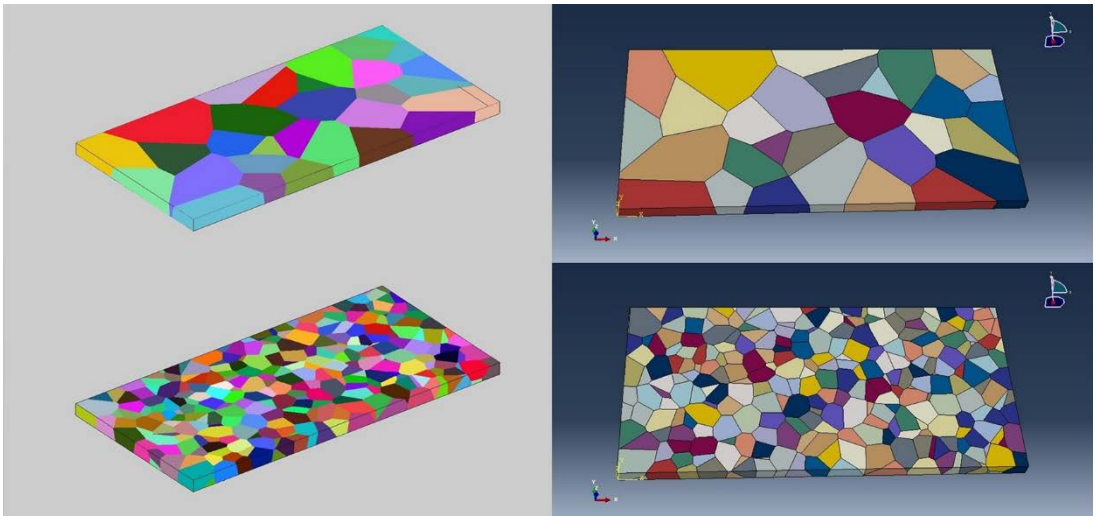

Figure 7-6 3D Voronoi tessellation implementation in MATLAB (left) and ABAQUS/CAE (right) with 30 and 300 grains respectively.

Figure 7-6 displays 3D Voronoi diagram implementation in MATLAB and ABAQUS with 30 grains (grain size 290.9 μm) and 300 grains (grain size 96.1 μm) in a 2 mm×1 mm×0.07 mm specimen respectively. The grain density can be calculated by the following equation:

$$\rho_G = \frac{3}{4} \cdot \frac{l \times w \times h}{\pi (D_{ave}/2)^3} \tag{7-1}$$

When there is only one grain in thickness direction which is the same condition with our specimens, there is no need to take thickness value into account; regarding the specimen as a two-dimensional one, the grain density equation can be expressed as:

$$\rho_G = \frac{l \times w}{\pi (D_{ave}/2)^2} \tag{7-2}$$

where *l*, *w* and *h* are the specimen's dimension: length, width and height, and D_{ave} is the average gran size. It can be seen that each Voronoi tessellations can be successfully generated and visualised as 'grains' in ABAQUS/CAE.

7.4.2 Grain heterogeneity

How to realise the grain heterogeneity in Voronoi diagram by Python script file has been detailed in Chapter 6, therefore, in this section, we study how to apply it with FE model. In this simulation, micro V-bending specimen sizing 2 mm×1 mm×0.07 mm is designed with 75 grains according to physical average grain size of 162.8 μm and Equation (7-2). The quantities of grains which possess different grain mechanical properties were calculated via multiplying each $f(\sigma, \varepsilon)$ from Equation (7-2) by total number of 75 grains. Except grains of the mean grain mechanical property, other grains'

quantities can be obtained by as above products. The grains of the mean grain property can be calculated via subtracting the grain quantity of the other six grain properties from total 75 grains. After calculation, the quantities of grains possessing the upper and lower bound grain mechanical properties are both 6, and both 13 grains are equipped with grain mechanical properties 1 and 2. Moreover, grain mechanical properties 3 and 4 are occupied by both 10 grains individually and the rest of 17 grains possess the mean grain mechanical properties. In this way, all 75 grains which consist of a bending specimen are provided with a certain grain mechanical property.

To the 75 grains, green (17 grains) represents the mean grain plastic property, grey (13 grains) and white (13 grains) symbolise grain mechanical properties 2 and 3, and yellow (10 grains) and red (10 grains) stand for grain mechanical properties 1 and 4 respectively. The upper and lower bound grain plastic properties are represented by dark blue (6 grains) and light blue (6 grains) seen in Figure 7-7.

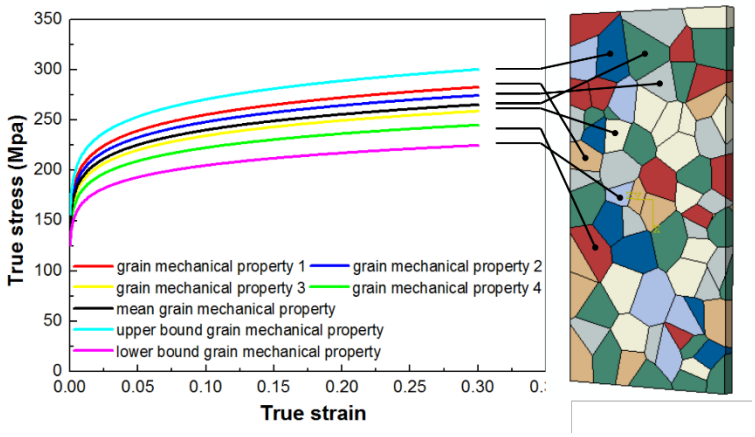

Figure 7-7 Grain properties randomly assigned on voronoised bending sample.

In order to investigate the influence of grain heterogeneity on springback, as it can be seen that the FE model is not set up as a traditional asymmetric one. Instead, the model is closer to real physical experimental condition as the right and the left sides of the sample are not equal in terms of grain size and the scatter of grain mechanical properties.

7.4.3 Numerical simulation procedure

Here the authors simulate micro V-bending process with an implicit FEM package: ABAQUS/Standard. The process parameters in the simulation are the same as those in physical experiments, and the value of friction coefficient is 0.02 according to the study from [62]. The FE model of micro V-bending and voronoised specimen is shown in Figure 7-8(a), and Figure 7-8(b) illustrates the grain heterogeneity in voronoised specimen, among which different colours represent different grain mechanical properties.

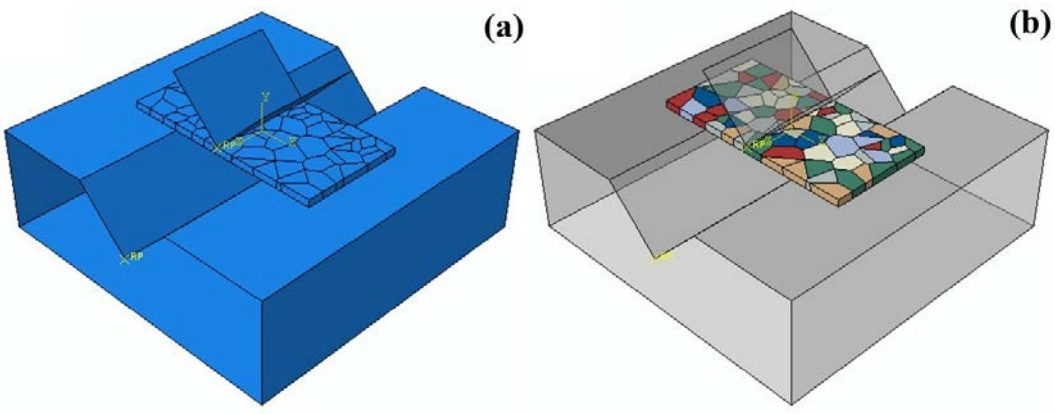

Figure 7-8 FEM simulation of micro V-bending with Voronoi tessellations (a) and grain heterogeneity (b).

The meshing of bending specimen is displayed in Figure 7-9. Due to tiny edges in Voronoi tessellations, some regions in the specimen are too complicated for structured and sweep meshing. Therefore, the modified tetrahedral element C3D10M which is robust to solve large deformation and contact problems was adopted in this simulation, and two analytic rigid surfaces are used to simulate the punch and die since they are stiff components.

Figure 7-9 Meshing of voronoised bending specimen.

7.5 Verification and discussion

Figure 7-10 illustrates the final result of the micro V-bending simulation. It is noticeable that the inhomogeneous deformation occurred during the bending process. The middle deformation zone presents different colours, which means different grains in this area experienced various deformation behaviours due to the grain heterogeneity. This can be explained that in the whole bending process, some grains firstly reach their

yield stress points, which leads to plastic deformation happens prior to other grains. By this analogy, some grains have low yield stress points, and this means they may still be under elastic stress condition even the specimen has started the plastic deformation. So this kind of grain heterogeneous defamation can play a significant role in affecting springback result and needs to be considered when conducting numerical simulation of microforming process. The angle was measured by CAD software, and it is observed that the right and the left side of sample experienced different levels of bending and springback, which means the two halves of bending specimen deformed differently due to the grain heterogeneity.

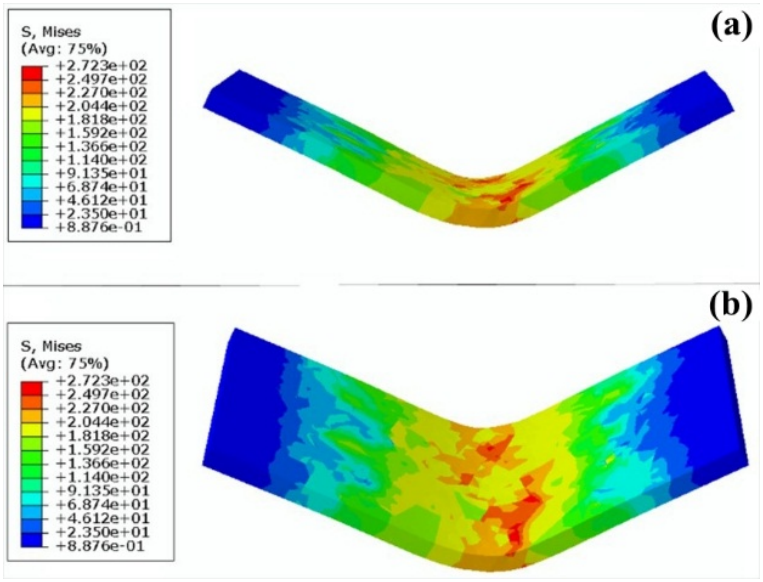

Figure 7-10 Final angles after springback (a) and Von Mises stress distribution (b).

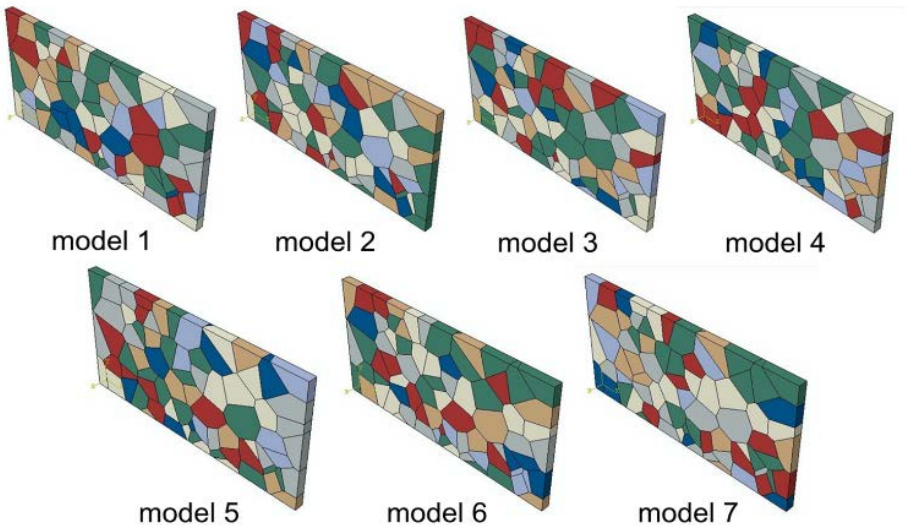

Figure 7-11 Bending specimens with different grain heterogeneity distributions.

During traditional bending test, central main deformation area's deformation behaviour is most decisive to the deformation process and the final angle. In micro V-bending, random distribution of each grain plastic property in the specimen has an essential influence on simulation result. Even the difference is small, the grain heterogeneity can be quite dominant. This kind of phenomenon could be also caused by distinctive meshing in each grain in the FE model due to distinctive grain shape and size. With the consideration of the grain heterogeneity in micro V-bending, the grain mechanical properties of main deformation area can straight forwardly affect the final angle and springback result. However, Python script cannot fix the distribution of grains plastic properties during the process of assigning grains plastic properties to grains, which means grains plastic properties are fixed in terms of their grain numbers but irregular in terms of distribution. Take upper bound grain mechanical properties as an example,

it is known that it is assigned to 6 grains but unassured that where these 6 grains will distribute in the specimen. So in order to minimise the uncertainty of distribution of grain mechanical properties in the main deformation area, it is assumed that each grain mechanical property has one seventh opportunity to be assigned to grains located in central deformation zone. This hypothesis is based on that seven grain plastic properties are obtained by experiment and calculation, and they are randomly distributed in bending specimens. Specimens with different random grain heterogeneity distributions were exhibited in Figure 7-11, which are called models 1, 2 and so on.

Seven groups micro V-bending FEM simulations have been conducted with above seven specimens individually. Springback angles of seven simulations and an average were measured and calculated as shown in Table 7-2.

Table 7-2 Springback angles from FEM simulation (degree).

Distribution group	1	2	3	4	5	6	7	average
Springback angles	30.52	27.37	32.09	31.78	33.44	28.65	34.12	31.14

Seven simulation springback angles were averaged to compare with three experimental values illustrated in Figure 7-12. It can be seen that the springback angles from FE

simulation models 1, 3 and 4 are in good agreement with experimental springback angles. This can be attributed to the grain heterogeneity which can reflect bending specimen's mechanical property from microscopic level. In other words, the adoption of the scatter of grain mechanical properties in this model can compensate the errors from tensile tests. This is because more or less errors can occur during tensile tests, and the application of these results in coming FE models will lead to further inaccuracy of simulation results. The scatter of grain mechanical properties provides a range of mechanical properties, covering the possible errors from tensile tests consequently. Moreover, it is noticeable that simulations with other models vary from experimental results significantly.

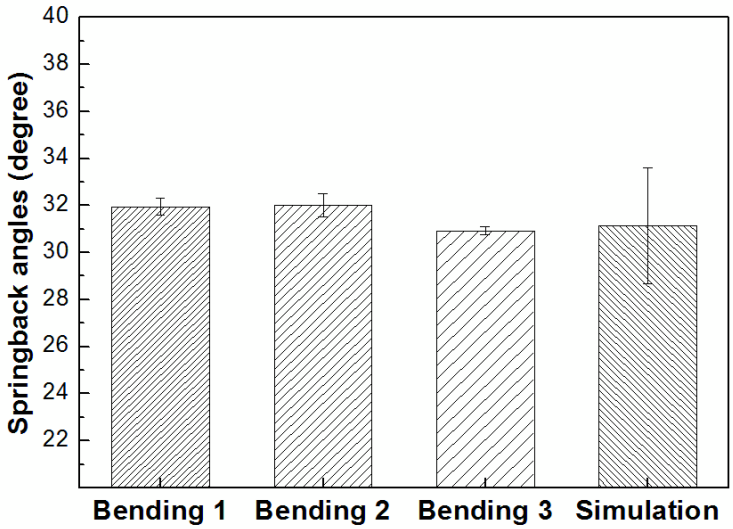

Figure 7-12 Comparison between experimental and simulation final angles after springback.

This outcome can also explained by the grain heterogeneity. As mentioned above, Python scripts cannot control the distribution of grain mechanical properties in the specimen. So in this simulation, if many upper or lower bound grain properties were distributed in central deformation area, then the bending (springback) results could differentiate from experimental ones. Conversely, if enough grains assigned with mean grain mechanical properties were distributed in central deformation area, the numerical result should have a good agreement with practical ones. At the same time, it is found that the average springback angle and experimental results have a good agreement. The scatter of springback angles can be successfully reduced by averaging the testing values. This is because the influence of the random distribution of the grain heterogeneity is lessened. The grain heterogeneity, in essence, is grain mechanical properties irregularly spread in the whole specimen. To a single specimen in FE simulation, due to the uncertainty of the distributions of grain mechanical properties, the corresponding springback angle may be larger, lower or close to counterpart experimental value. However, with more numbers of distributions are taken into FE simulations, the clearer upper and lower bounds in which the springback angles will scatter, and the scatter can be minimised by averaging, and the average springback angles should be one of the closest results. From this perspective, the grain heterogeneity is the main reason for the scatter of springback angles.

7.6 Summary

In this study, the scatter of grain mechanical properties is calculated based on the results from tensile tests and these grain mechanical properties were assigned to each Voronoi tessellation to achieve the grain heterogeneity in ABAQUS/CAE. A new FE model is built with above mentioned Voronoi tessellation and grain heterogeneity to simulate the micro V-bending process. Micro V-bending experiment is also conducted to validate the numerical results. The following conclusions are drawn from this study:

(1) The 3D Voronoi tessellations can be displayed in ABAQUS/CAE based on experimental microstructure and grain size, and the specimen consists of Voronoi tessellations can effectively represent grain shape and size.

(2) The grain heterogeneity can be expressed by the scatter of grain mechanical properties based on the scatter of material mechanical properties which is acquired by tensile tests.

(3) A FE model is established with Voronoi tessellations and the grain heterogeneity, and the simulation results and experimental ones are in good agreement, which verified the reliability of the developed model.

(4) The distribution of grain mechanical properties in main formation area of specimen is one of the most influential factors affecting springback angles.

Chapter 8 Conclusions and future work

8.1 Conclusions

Detailed conclusions have been described in Chapters 4 - 7. The general conclusions are presented in the similar sequence of the chapter as follows.

(1) In microforming, deformation behaviour is very sensitive to the value of the ratio of thickness to average grain size when the range is around 1.

(2) $T/D \approx 1$ can be regards as the divide of ductile fracture and brittle fracture, and this ratio becomes a decisive factor to materials' fracture mode.

(3) When $T/D<1$, the classic surface layer model cannot be applied. A new constitutive model is developed based on composite model, and the validity of the developed model has been verified.

(4) Recrystallisation texture is correlative with the material's grain size effect. When the ratio T/D changes around 1 as a divide, the types of texture component and their corresponding intensities also vary.

(5) Annealing texture evolution of phosphor bronze denotes typical α-fibre components. Meanwhile, it is found that when the value of *T*/*D* increases, the intensities of the Goss and Brass components decrease but the intensity of the A orientation increases.

(6) During micro V-bending process, the grain rotation has a connection with the ratio *T*/*D*: when the ratio *T*/*D* decreases, not many grains are likely to rotate.

(7) The stability of {110} crystallographic plane increases with the decrease of *T*/*D* from *T*/*D* >1 to <1 during micro V-bending process.

(8) The 2D/3D Voronoi diagrams can be displayed in ABAQUS/CAE with MATLAB and Python to represent polycrystalline aggregate.

(9) The grain heterogeneity can be obtained from the scatter of grain mechanical properties which is extended from the scatter of material mechanical properties.

(10) A FE bending model has been established with Voronoi tessellations and the grain heterogeneity, and it precisely predicted the springback angles.

(11) The distribution of grain mechanical properties in main formation area of specimen is one of the most influential factors affecting springback angles in microforming of metals.

8.2 Future work

In this study, micro V-bending is conducted to investigate the change of crystallographic orientation on f. c. c. phosphor bronze with three different *T*/*D* ratios. Since it has been found that *T*/*D* is closely related with the stability of {110} crystallographic plane and grain rotation, *T*/*D* could have a great impact on springback angle was assumed. This assumption is also based on the work from Meyersm and Ashworth [134] as shown in Figure 8-1. The grain orientation has an obvious effect on the elastic properties of individual grain, especially the Young's modulus, which means the ratio *T*/*D* could affect springback because it has an influence on grain orientation during deformation, which should be further studied in the future.

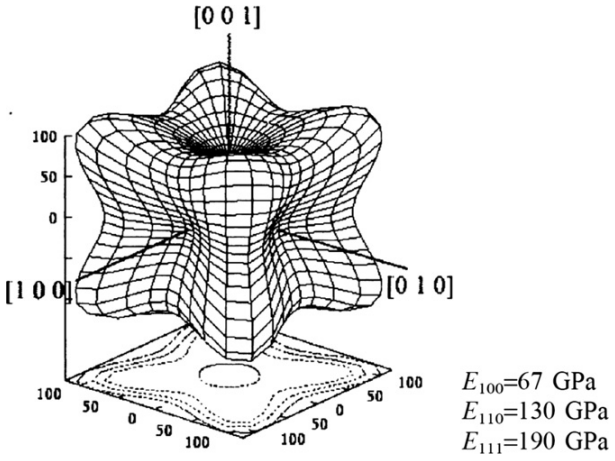

Figure 8-1 Polar plots of Young's modulus showing the elastic anisotropy in copper [134].

In addition, the 3D Voronoi tessellations in FE simulation have an issue which can be improved in the future. The voronoised grains both in MATLAB and ABAQUS/CAE contain some small edges shown in Figure 8-2, and these edges cannot accommodate too many seeds during seeding in ABAQUS pre-processing. Consequently, this drawback will limit the element type and mesh algorithm, affecting the meshing result and simulation result consequently.

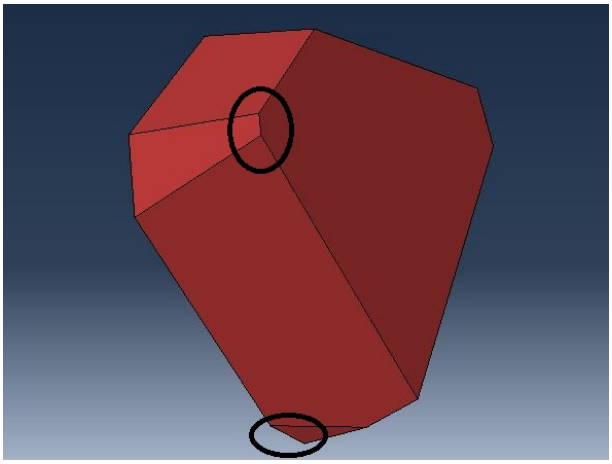

Figure 8-2 Small edges in 3D Voronoi tessellation.

Furthermore, the scatters of grain mechanical properties in this study are expressed by the scatter of specimen mechanical properties which are obtained by micro tensile test. Since the grain orientation information (both before bending and after bending) in three different *T*/*D* materials has been obtained by EBSD technology, crystal plasticity finite element method (CPFEM) could be adopted to extend this research. In that case, the scatter of grain mechanical properties will not be appropriate, since their values are

not in a certain range, but will be expressed by Euler angles (φ, θ, Ψ). This means each grain in the specimen will have a unique character in terms of angle values and its precision should be more reliable. Applying Voronoi tessellations into CPFEM and improving the precision of simulation can be a part of future study

Therefore, these three points can form the future work.

(1) To further enhance the accuracy of the springback prediction in FE simulation with the consideration of grain orientation. This requires the knowledge of crystal plasticity finite element methods.

(2) To optimise the geometrical structure of 3D Voronoi tessellations. This aims to replace the small edges and faces in Voronoi tessellations by vertices, thus facilitating seeding and obtaining better meshing results.

(3) To combine Voronoi tessellations with CPFEM in FE simulation. By comparing predicted results with experimental ones, useful information about deformation mode activation, stress-strain data and crystal re-orientations can be obtained, which leads to a fundamentally understanding of the nature of bending under the grain scale.

References

1. F. Vollertsen, *Categories of size effects.* Production Engineering, 2008. 2(4): p. 377-383.
2. R. Eckstein, M. Geiger, and U. Engel. *Specific characteristics of micro sheet metal working*. in *Proceedings of the SheMet, September*. 1999.
3. H. Wicht and J. Bouchaud, *NEXUS market analysis for MEMS and microsystems III 2005-2009.* MST-news, Verlag VDI/VDE Innovation+ Technik GmbH, 2005. 5: p. 33-34.
4. F. Vollertsen, Z. Hu, H. S. Niehoff, and C. Theiler, *State of the art in micro forming and investigations into micro deep drawing.* Journal Of Materials Processing Technology, 2004. 151(1): p. 70-79.
5. M. Geiger and U. Engel, *Microforming-a Challenge to the Plasticity Research Community-Addressed to the 40th Anniversary of the JSTP.* JOURNAL-JAPAN SOCIETY FOR TECHNOLOGY OF PLASTICITY, 2002. 43(3; ISSU 494): p. 5-7.
6. U. Engel and R. Eckstein, *Microforming—from basic research to its realization.* Journal Of Materials Processing Technology, 2002. 125: p. 35-44.
7. C. Pande and K. Cooper, *Nanomechanics of Hall–Petch relationship in nanocrystalline materials.* Progress In Materials Science, 2009. 54(6): p. 689-706.

8. M. Zhao, J. Li, and Q. Jiang, *Hall–Petch relationship in nanometer size range.* Journal Of Alloys And Compounds, 2003. 361(1): p. 160-164.

9. N. Tiesler, *Microforming—size effects in friction and their influence on extrusion processes.* Wire, 2002. 52(1): p. 34-38.

10. T. Sobis, U. Engel, and M. Geiger, *A theoretical study on wear simulation in metal forming processes.* Journal Of Materials Processing Technology, 1992. 34(1): p. 233-240.

11. M. Geiger, M. Kleiner, R. Eckstein, N. Tiesler, and U. Engel, *Microforming.* CIRP Annals-Manufacturing Technology, 2001. 50(2): p. 445-462.

12. F. Vollertsen, H. Schulze Niehoff, and Z. Hu, *State of the art in micro forming.* International Journal of Machine Tools and Manufacture, 2006. 46(11): p. 1172-1179.

13. F. Vollertsen, D. Biermann, H. N. Hansen, I. Jawahir, and K. Kuzman, *Size effects in manufacturing of metallic components.* CIRP Annals-Manufacturing Technology, 2009. 58(2): p. 566-587.

14. X. Ma, R. Lapovok, C. Gu, A. Molotnikov, Y. Estrin, E. Pereloma, C. Davies, and P. Hodgson, *Deep drawing behaviour of ultrafine grained copper: modelling and experiment.* Journal of materials science, 2009. 44(14): p. 3807-3812.

15. T. Kals and R. Eckstein, *Miniaturization in sheet metal working.* Journal Of Materials Processing Technology, 2000. 103(1): p. 95-101.

16. M. Fu and W. Chan, *Geometry and grain size effects on the fracture behavior of sheet metal in micro-scale plastic deformation.* Materials & Design, 2011. 32(10): p. 4738-4746.

17. L. Raulea, A. Goijaerts, L. Govaert, and F. Baaijens, *Size effects in the processing of thin metal sheets.* Journal of Materials Processing Technology, 2001. 115(1): p. 44-48.

18. W. Chan, M. Fu, J. Lu, and J. Liu, *Modeling of grain size effect on micro deformation behavior in micro-forming of pure copper.* Materials Science And Engineering: A, 2010. 527(24): p. 6638-6648.

19. H. Lu, D. Wei, Z. Jiang, K. Manabe, and K. Furushima, *Study on size effect in micro cross wedge rolling.* International Journal of Steel Research, 2011: p. 962-967.

20. H.-Z. Li, X.-H. Dong, Y. Shen, R. Zhou, A. Diehl, H. Hagenah, U. Engel, M. Merklein, and J. Cao, *Analysis of microbending of CuZn37 brass foils based on strain gradient hardening models.* Journal Of Materials Processing Technology, 2012. 212(3): p. 653-661.

21. J. Xu, B. Guo, C. Wang, and D. Shan, *Blanking clearance and grain size effects on micro deformation behavior and fracture in micro-blanking of brass foil.* International Journal of Machine Tools and Manufacture, 2012. 60: p. 27-34.

22. J. Liu, M. Fu, J. Lu, and W. Chan, *Influence of size effect on the springback of sheet metal foils in micro-bending.* Computational Materials Science, 2011. 50(9): p. 2604-2614.

23. C. Wang, D. Shan, J. Zhou, B. Guo, and L. Sun, *Size effects of the cavity dimension on the microforming ability during coining process.* Journal of Materials Processing Technology, 2007. 187: p. 256-259.

24. J.-T. Gau, C. Principe, and M. Yu, *Springback behavior of brass in micro sheet forming.* Journal Of Materials Processing Technology, 2007. 191(1): p. 7-10.

25. A. Diehl, U. Engel, and M. Geiger, *Mechanical properties and bending behaviour of metal foils.* Proceedings of the Institution of Mechanical Engineers, Part B: Journal of Engineering Manufacture, 2008. 222(1): p. 83-91.

26. R. Ben Hmida, S. Thibaud, A. Gilbin, and F. Richard, *Influence of the initial grain size in single point incremental forming process for thin sheets metal and microparts: Experimental investigations.* Materials & Design, 2013. 45: p. 155-165.

27. S. H. C. Park, Y. S. Sato, and H. Kokawa, *Effect of micro-texture on fracture location in friction stir weld of Mg alloy AZ61 during tensile test.* Scripta Materialia, 2003. 49(2): p. 161-166.

28. J. Del Valle, F. Carreño, and O. A. Ruano, *Influence of texture and grain size on work hardening and ductility in magnesium-based alloys processed by ECAP and rolling.* Acta Materialia, 2006. 54(16): p. 4247-4259.

29. J. Del Valle and O. Ruano, *Separate contributions of texture and grain size on the creep mechanisms in a fine-grained magnesium alloy.* Acta Materialia, 2007. 55(2): p. 455-466.

30. L. Llanes, A. Rollett, C. Laird, and J. Bassani, *Effect of grain size and annealing texture on the cyclic response and the substructure evolution of polycrystalline copper.* Acta metallurgica et materialia, 1993. 41(9): p. 2667-2679.

31. P. Janssen, T. H. De Keijser, and M. Geers, *An experimental assessment of grain size effects in the uniaxial straining of thin Al sheet with a few grains across the thickness.* Materials Science And Engineering: A, 2006. 419(1): p. 238-248.

32. M. Hoseini, A. Shahryari, S. Omanovic, and J. A. Szpunar, *Comparative effect of grain size and texture on the corrosion behaviour of commercially pure titanium processed by equal channel angular pressing.* Corrosion Science, 2009. 51(12): p. 3064-3067.

33. S. Yin, C. Wang, Y. Diao, S. Wu, and S. Li, *Influence of grain size and texture on the yield asymmetry of Mg-3Al-1Zn alloy.* Journal Of Materials Science & Technology, 2011. 27(1): p. 29-34.

34. L. Guo, Z. Chen, and L. Gao, *Effects of grain size, texture and twinning on mechanical properties and work-hardening behavior of AZ31 magnesium alloys.* Materials Science And Engineering: A, 2011. 528(29): p. 8537-8545.

35. H. Zhang, G. Huang, D. Kong, G. Sang, and B. Song, *Influence of initial texture on formability of AZ31B magnesium alloy sheets at different temperatures.* Journal Of Materials Processing Technology, 2011. 211(10): p. 1575-1580.

36. H. Kaneko and T. Eguchi, *Influence of Texture on Bendability of Cu-Ni-Si Alloys.* Materials Transactions, 2012. 53(11): p. 1847-1851.

37. M. Mabuchi, Y. Chino, H. Iwasaki, T. Aizawa, and K. Higashi, *The grain size and texture dependence of tensile properties in extruded Mg-9Al-1Zn.* Materials transactions-JIM, 2001. 42(7): p. 1182-1189.

38. T. Leffers and D. Juul Jensen, *The effect of bending and straightening on rolling texture and microstructure in brass.* Scripta metallurgica et materialia, 1990. 24(12): p. 2431-2435.

39. Y. Sutou, T. Omori, K. Yamauchi, N. Ono, R. Kainuma, and K. Ishida, *Effect of grain size and texture on pseudoelasticity in Cu–Al–Mn-based shape memory wire.* Acta Materialia, 2005. 53(15): p. 4121-4133.

40. B. Song, G. Huang, H. Li, L. Zhang, G. Huang, and F. Pan, *Texture evolution and mechanical properties of AZ31B magnesium alloy sheets processed by repeated unidirectional bending.* Journal Of Alloys And Compounds, 2010. 489(2): p. 475-481.

41. Y. Sutou, T. Omori, N. Koeda, R. Kainuma, and K. Ishida, *Effects of grain size and texture on damping properties of Cu–Al–Mn-based shape memory alloys.* Materials Science And Engineering: A, 2006. 438: p. 743-746.

42. M. Barnett, Z. Keshavarz, A. Beer, and D. Atwell, *Influence of grain size on the compressive deformation of wrought Mg–3Al–1Zn.* Acta Materialia, 2004. 52(17): p. 5093-5103.

43. S. Vaidya and A. Sinha, *Effect of texture and grain structure on electromigration in Al-0.5% Cu thin films.* Thin Solid Films, 1981. 75(3): p. 253-259.

44. Y. Wang, C. Chang, C. Lee, H. Lin, and J. Huang, *Texture and weak grain size dependence in friction stir processed Mg–Al–Zn alloy.* Scripta Materialia, 2006. 55(7): p. 637-640.

45. F. Cimolin, R. Vadori, and C. Canuto, *Springback compensation in deep drawing applications.* Meccanica, 2008. 43(2): p. 101-113.

46. R. Hill, *The mathematical theory of plasticity*. Vol. 11. 1998: Oxford university press.

47. A. Mendelson, *Plasticity: theory and application*. 1968: Macmillan New York.

48. T. Buranathiti and J. Cao, *An effective analytical model for springback prediction in straight flanging processes.* International Journal of Materials and Product Technology, 2004. 21(1): p. 137-153.

49. T. Meinders, A. Konter, S. Meijers, E. Atzema, and H. Kappert, *A sensitivity analysis on the springback behavior of the unconstrained bending problem.* International Journal of Forming Processes, 2006. 9(3): p. 365-402.

50. I.-N. Chou and C. Hung, *Finite element analysis and optimization on springback reduction.* International Journal of Machine Tools and Manufacture, 1999. 39(3): p. 517-536.

51. S. Han and K. Park. *An investigation of the factors influencing springback by empirical and simulative techniques*. in *Proceedings of Numisheet*. 1999.

52. *Z.* Tekıner, *An experimental study on the examination of springback of sheet metals with several thicknesses and properties in bending dies.* Journal of Materials Processing Technology, 2004. 145(1): p. 109-117.

53. L. Zhang, G. Lu, and S. Leong, *V-shaped sheet forming by deformable punches.* Journal of Materials Processing Technology, 1997. 63(1): p. 134-139.

54. H. Livatyali and T. Altan, *Prediction and elimination of springback in straight flanging using computer aided design methods: Part 1. Experimental investigations.* Journal of Materials Processing Technology, 2001. 117(1): p. 262-268.

55. H. Livatyali, H. Wu, and T. Altan, *Prediction and elimination of springback in straight flanging using computer-aided design methods: Part 2: Fem predictions and tool design.* Journal of Materials Processing Technology, 2002. 120(1): p. 348-354.

56. T. Kuwabara, Y. Asano, S. Ikeda, and H. Hayashi, *An evaluation method for springback characteristics of sheet metals based on a stretch bending test.* Proc. IDDRG 2004,Sindelfingen Germany, 2004: p. 55-64.

57. F. Pourboghrat and E. Chu, *Springback in plane strain stretch/draw sheet forming.* International Journal of Mechanical Sciences, 1995. 37(3): p. 327-341.

58. G. Liu, Z. Lin, W. Xu, and Y. Bao, *Variable blankholder force in U-shaped part forming for eliminating springback error.* Journal of Materials Processing Technology, 2002. 120(1): p. 259-264.

59. W. Xu, C. Ma, C. Li, and W. Feng, *Sensitive factors in springback simulation for sheet metal forming.* Journal of Materials Processing Technology, 2004. 151(1): p. 217-222.

60. E. Bayraktar and S. Altintas, *Square cup deep drawing and 2D-draw bending analysis of Hadfield steel.* Journal of Materials Processing Technology, 1996. 60(1): p. 183-190.

61. W. Carden, L. Geng, D. Matlock, and R. Wagoner, *Measurement of springback.* International Journal of Mechanical Sciences, 2002. 44(1): p. 79-101.

62. K. Li, W. Carden, and R. Wagoner, *Simulation of springback.* International Journal of Mechanical Sciences, 2002. 44(1): p. 103-122.

63. R. Wagoner. *Fundamental aspects of springback in sheet metal forming*. in *Proc of Numisheet Conf, Jejv Island, Korea*. 2002.

64. K. Li, L. Geng, and R. Wagoner. *Simulation of springback: choice of element*. in *Proceedings of Sixth ICTP*. 1999.

65. Z. Zhang and S. Hu, *Stress and residual stress distributions in plane strain bending.* International Journal of Mechanical Sciences, 1998. 40(6): p. 533-543.

66. L. Geng, Y. Shen, and R. Wagoner, *Anisotropic hardening equations derived from reverse-bend testing.* International journal of plasticity, 2002. 18(5): p. 743-767.

67. B. Chun, J. Jinn, and J. Lee, *Modeling the Bauschinger effect for sheet metals, part I: theory.* International journal of plasticity, 2002. 18(5): p. 571-595.

68. R. Cleveland and A. Ghosh, *Inelastic effects on springback in metals.* International Journal Of Plasticity, 2002. 18(5): p. 769-785.

69. F. Yoshida, T. Uemori, and K. Fujiwara, *Elastic–plastic behavior of steel sheets under in-plane cyclic tension–compression at large strain.* International journal of plasticity, 2002. 18(5): p. 633-659.

70. K. Zhao and J. Lee, *Finite element analysis of the three-point bending of sheet metals.* Journal of Materials Processing Technology, 2002. 122(1): p. 6-11.

71. F. Yoshida, M. Urabe, and V. Toropov, *Identification of material parameters in constitutive model for sheet metals from cyclic bending tests.* International Journal of Mechanical Sciences, 1998. 40(2): p. 237-249.

72. J.-T. Gau and G. L. Kinzel, *A new model for springback prediction in which the Bauschinger effect is considered.* International Journal of Mechanical Sciences, 2001. 43(8): p. 1813-1832.

73. J.-T. Gau and G. L. Kinzel, *An experimental investigation of the influence of the Bauschinger effect on springback predictions.* Journal of Materials Processing Technology, 2001. 108(3): p. 369-375.

74. A. Diehl, U. Engel, and M. Geiger, *Spring-Back Behaviour of Thin Metal Foils in Free Bending Processes.* Multi-Material Micro Manufacture, 2005: p. 147-150.

75. C. Bruni, A. Forcellese, F. Gabrielli, and M. Simoncini, *Air bending of AZ31 magnesium alloy in warm and hot forming conditions.* Journal Of Materials Processing Technology, 2006. 177(1): p. 373-376.

76. F.-K. Chen and T.-B. Huang, *Formability of stamping magnesium-alloy AZ31 sheets.* Journal Of Materials Processing Technology, 2003. 142(3): p. 643-647.

77. Y. Moon, S. Kang, J. Cho, and T. Kim, *Effect of tool temperature on the reduction of the springback of aluminum sheets.* Journal Of Materials Processing Technology, 2003. 132(1): p. 365-368.

78. S. Novotny and M. Geiger, *Process design for hydroforming of lightweight metal sheets at elevated temperatures.* Journal of Materials Processing Technology, 2003. 138(1): p. 594-599.

79. S. Novotiny, M. Celeghini, and M. Geiger, *Measurement of material properties of aluminum sheet alloys at elevated temperature.* Proceedings of the Eighth SheMet'00, Birmingham, 2000: p. 363-370.

80. S. Novotny and P. Hein, *Hydroforming of sheet metal pairs from aluminium alloys.* Journal of Materials Processing Technology, 2001. 115(1): p. 65-69.

81. Y. Moon, Y. Kang, J. Park, and S. Gong, *Tool temperature control to increase the deep drawability of aluminum 1050 sheet.* International Journal of Machine Tools and Manufacture, 2001. 41(9): p. 1283-1294.

82. G. E. Dieter, *Mechanical metallurgy*. Vol. 3. 1976: McGraw-Hill New York.

83. S.-I. Oh and T. Altan, *Metal forming and the finite-element method*. 1989: Oxford university press.

84. R. H. Wagoner and J.-L. Chenot, *Metal forming analysis*. 2001: Cambridge University Press.

85. S. Choudhry and J. Lee, *Dynamic plane-strain finite element simulation of industrial sheet-metal forming processes.* International Journal of Mechanical Sciences, 1994. 36(3): p. 189-207.

86. J. Cho, S. Moon, Y. Moon, and S. Kang, *Finite element investigation on spring-back characteristics in sheet metal U-bending process.* Journal of Materials Processing Technology, 2003. 141(1): p. 109-116.

87. L.-P. Lei, S.-M. Hwang, and B.-S. Kang, *Finite element analysis and design in stainless steel sheet forming and its experimental comparison.* Journal Of Materials Processing Technology, 2001. 110(1): p. 70-77.

88. H. Mullan, *Improved prediction of springback on final formed components.* Journal of Materials Processing Technology, 2004. 153: p. 464-471.

89. L. Papeleux and J.-P. Ponthot, *Finite element simulation of springback in sheet metal forming.* Journal of Materials Processing Technology, 2002. 125: p. 785-791.

90. M. Math and B. Grizelj, *Finite element approach in the plate bending process.* Journal of Materials Processing Technology, 2002. 125: p. 778-784.

91. P. Chen, M. Koc, and M. L. Wenner, *Experimental investigation of springback variation in forming of high strength steels.* Journal of manufacturing science and engineering, 2008. 130(4).

92. V. Esat, H. Darendeliler, and M. I. Gokler, *Finite element analysis of springback in bending of aluminium sheets.* Materials & Design, 2002. 23(2): p. 223-229.

93. X. Li, Y. Yang, Y. Wang, J. Bao, and S. Li, *Effect of the material-hardening mode on the springback simulation accuracy of V-free bending.* Journal of Materials Processing Technology, 2002. 123(2): p. 209-211.

94. Q. Bui, L. Papeleux, and J.-P. Ponthot, *Numerical simulation of springback using enhanced assumed strain elements.* Journal of Materials Processing Technology, 2004. 153: p. 314-318.

95. P. Sun, J. Gracio, and J. Ferreira, *Control system of a mini hydraulic press for evaluating springback in sheet metal forming.* Journal of Materials Processing Technology, 2006. 176(1): p. 55-61.

96. C. Gomes, O. Onipede, and M. Lovell, *Investigation of springback in high strength anisotropic steels.* Journal of Materials Processing Technology, 2005. 159(1): p. 91-98.

97. Y. Ling, H. Lee, and B. Cheok, *Finite element analysis of springback in L-bending of sheet metal.* Journal of Materials Processing Technology, 2005. 168(2): p. 296-302.

98. R. Bahloul, S. Ben-Elechi, and A. Potiron, *Optimisation of springback predicted by experimental and numerical approach by using response surface methodology.* Journal of Materials Processing Technology, 2006. 173(1): p. 101-110.

99. J.-H. Song, H. Huh, and S.-H. Kim, *Stress-based springback reduction of a channel shaped auto-body part with high-strength steel using response surface*

methodology. Journal of engineering materials and technology, 2007. 129(3): p. 397-406.

100. A. D. Santos and P. Teixeira, *A study on experimental benchmarks and simulation results in sheet metal forming.* Journal of Materials Processing Technology, 2008. 199(1): p. 327-336.

101. W. Gan and R. Wagoner, *Die design method for sheet springback.* International Journal of Mechanical Sciences, 2004. 46(7): p. 1097-1113.

102. J. Yanagimoto and K. Oyamada, *Mechanism of springback-free bending of high-strength steel sheets under warm forming conditions.* CIRP Annals-Manufacturing Technology, 2007. 56(1): p. 265-268.

103. M. Oliveira, J. Alves, B. Chaparro, and L. Menezes, *Study on the influence of work-hardening modeling in springback prediction.* International journal of plasticity, 2007. 23(3): p. 516-543.

104. S.-W. Lee, *A study on the bi-directional springback of sheet metal stamping.* Journal of Materials Processing Technology, 2005. 167(1): p. 33-40.

105. D. Fei and P. Hodgson, *Experimental and numerical studies of springback in air v-bending process for cold rolled TRIP steels.* Nuclear engineering and design, 2006. 236(18): p. 1847-1851.

106. Tekaslan, U. Şeker, and A. zdemir, *Determining springback amount of steel sheet metal has 0.5 mm thickness in bending dies.* Materials & Design, 2006. 27(3): p. 251-258.

107. H. Kim, N. Nargundkar, and T. Altan, *Prediction of bend allowance and springback in air bending.* Journal of manufacturing science and engineering, 2007. 129(2): p. 342-351.

108. M. Garcia-Romeu, J. Ciurana, and I. Ferrer, *Springback determination of sheet metals in an air bending process based on an experimental work.* Journal of Materials Processing Technology, 2007. 191(1): p. 174-177.

109. S. Thipprakmas and S. Rojananan, *Investigation of spring-go phenomenon using finite element method.* Materials & Design, 2008. 29(8): p. 1526-1532.

110. U. Singh, S. Maiti, P. Date, and K. Narasimhan, *Numerical simulation of the influence of air bending tool geometry on product quality.* Journal of Materials Processing Technology, 2004. 145(3): p. 269-275.

111. S. Panthi, N. Ramakrishnan, M. Ahmed, S. S. Singh, and M. Goel, *Finite Element Analysis of sheet metal bending process to predict the springback.* Materials & Design, 2010. 31(2): p. 657-662.

112. H. Lu, D. Wei, Z. Jiang, X. Liu, and K. Manabe, *Modelling of size effects in microforming process with consideration of grained heterogeneity.* Computational Materials Science, 2013. 77: p. 44-52.

113. J.-S. Huang and L. Gibson, *Creep of open-cell Voronoi foams.* Materials Science and Engineering: A, 2003. 339(1): p. 220-226.

114. S. Ghosh, K. Lee, and S. Moorthy, *Two scale analysis of heterogeneous elastic-plastic materials with asymptotic homogenization and Voronoi cell finite*

element model. Computer Methods in Applied Mechanics and Engineering, 1996. 132(1): p. 63-116.

115. F. Fritzen, T. Böhlke, and E. Schnack, *Periodic three-dimensional mesh generation for crystalline aggregates based on Voronoi tessellations.* Computational Mechanics, 2009. 43(5): p. 701-713.

116. S. Ghosh, Z. Nowak, and K. Lee, *Quantitative characterization and modeling of composite microstructures by Voronoi cells.* Acta Materialia, 1997. 45(6): p. 2215-2234.

117. C. Tekoğlu and P. R. Onck, *Size effects in two-dimensional Voronoi foams: a comparison between generalized continua and discrete models.* Journal of the Mechanics and Physics of Solids, 2008. 56(12): p. 3541-3564.

118. G. Voronoï, *Nouvelles applications des paramètres continus à la théorie des formes quadratiques. Deuxième mémoire. Recherches sur les parallélloèdres primitifs.* Journal Fur Die Reine Und Angewandte Mathematik, 1908. 134: p. 198-287.

119. A. Okabe, B. Boots, K. Sugihara, and S. N. Chiu, *Spatial tessellations: concepts and applications of Voronoi diagrams*. Vol. 501. 2009: Wiley. com.

120. F. Aurenhammer, *Voronoi diagrams—a survey of a fundamental geometric data structure*. ACM Computing Surveys (CSUR), 1991. 23(3): p. 345-405.

121. W. Chan, M. Fu, and J. Lu, *The size effect on micro deformation behaviour in micro-scale plastic deformation.* Materials & Design, 2011. 32(1): p. 198-206.

122. M. Fu and W. Chan, *A review on the state-of-the-art microforming technologies.* The International Journal of Advanced Manufacturing Technology, 2013. 67(9-12): p. 2411-2437.

123. A. Diehl, U. Engel, and M. Geiger, *Influence of microstructure on the mechanical properties and the forming behaviour of very thin metal foils.* The International Journal of Advanced Manufacturing Technology, 2010. 47(1-4): p. 53-61.

124. W. Chan and M. Fu, *Studies of the interactive effect of specimen and grain sizes on the plastic deformation behavior in microforming.* The International Journal of Advanced Manufacturing Technology, 2012. 62(9-12): p. 989-1000.

125. W. Chan, M. Fu, and B. Yang, *Study of size effect in micro-extrusion process of pure copper.* Materials & Design, 2011. 32(7): p. 3772-3782.

126. J. Xu, B. Guo, and D. Shan, *Size effects in micro blanking of metal foil with miniaturization.* The International Journal of Advanced Manufacturing Technology, 2011. 56(5-8): p. 515-522.

127. F.-H. Yeh, C.-L. Li, and Y.-H. Lu, *Study of thickness and grain size effects on material behavior in micro-forming.* Journal Of Materials Processing Technology, 2008. 201(1): p. 237-241.

128. W. Chan and M. Fu, *Experimental studies and numerical modeling of the specimen and grain size effects on the flow stress of sheet metal in microforming.* Materials Science And Engineering: A, 2011. 528(25): p. 7674-7683.

129. J.-F. Michel and P. Picart, *Size effects on the constitutive behaviour for brass in sheet metal forming.* Journal Of Materials Processing Technology, 2003. 141(3): p. 439-446.

130. W. Yun, D. Peilong, X. Zhenying, Y. Hua, W. Jiangping, and W. Jingjing, *A constitutive model for thin sheet metal in micro-forming considering first order size effects.* Materials & Design, 2010. 31(2): p. 1010-1014.

131. L. Peng, F. Liu, J. Ni, and X. Lai, *Size effects in thin sheet metal forming and its elastic–plastic constitutive model.* Materials & Design, 2007. 28(5): p. 1731-1736.

132. L. Peng, X. Lai, H.-J. Lee, J.-H. Song, and J. Ni, *Analysis of micro/mesoscale sheet forming process with uniform size dependent material constitutive model.* Materials Science And Engineering: A, 2009. 526(1): p. 93-99.

133. H.-H. Fu, D. J. Benson, and M. A. Meyers, *Analytical and computational description of effect of grain size on yield stress of metals.* Acta Materialia, 2001. 49(13): p. 2567-2582.

134. M. A. Meyersm and E. Ashworth, *A model for the effect of grain size on the yield stress of metals.* Philosophical Magazine A, 1982. 46(5): p. 737-759.

135. J. Schiøtz, F. D. Di Tolla, and K. W. Jacobsen, *Softening of nanocrystalline metals at very small grain sizes.* Nature, 1998. 391(6667): p. 561-563.

136. X. Lai, L. Peng, P. Hu, S. Lan, and J. Ni, *Material behavior modelling in micro/meso-scale forming process with considering size/scale effects.* Computational Materials Science, 2008. 43(4): p. 1003-1009.

137. U. Kocks, *The relation between polycrystal deformation and single-crystal deformation.* Metallurgical and Materials Transactions, 1970. 1(5): p. 1121-1143.

138. J. P. Hirth, *The influence of grain boundaries on mechanical properties.* Metallurgical Transactions, 1972. 3(12): p. 3047-3067.

139. B. Peters, *The evolution of annealing textures in a heavily-deformed bronze.* Metallurgical Transactions, 1973. 4(3): p. 757-763.

140. J. Hirsch and K. Lücke, *Overview no. 76: Mechanism of deformation and development of rolling textures in polycrystalline fcc metals—I. Description of rolling texture development in homogeneous CuZn alloys.* Acta Metallurgica, 1988. 36(11): p. 2863-2882.

141. A. A. Saleh, E. V. Pereloma, and A. A. Gazder, *Texture evolution of cold rolled and annealed Fe–24Mn–3Al–2Si–1Ni–0.06 C TWIP steel.* Materials Science And Engineering: A, 2011. 528(13): p. 4537-4549.

142. W. Carrington and D. Mclean, *Slip nuclei in silicon-iron.* Acta Metallurgica, 1965. 13(5): p. 493-499.

143. R. Douthwaite and J. Evans, *Microstrain in polycrystalline aggregates.* Acta Metallurgica, 1973. 21(4): p. 525-530.

144. L. Murr, *Strain-induced dislocation emission from grain boundaries in stainless steel.* Materials Science and Engineering, 1981. 51(1): p. 71-79.

145. J. C. Li, *Petch relation and grain boundary sources.* Transactions of the Metallurgical Society of AIME, 1963. 227(1): p. 239-&.

146. J. Cao, W. Zhuang, S. Wang, and J. Lin, *Development of a VGRAIN system for CPFE analysis in micro-forming applications.* The International Journal of Advanced Manufacturing Technology, 2010. 47(9-12): p. 981-991.

147. R. Descartes, *Principles of philosophy*. Vol. 24. 1984: Springer.

148. H. Blum, *Biological shape and visual science (Part I).* Journal Of Theoretical Biology, 1973. 38(2): p. 205-287.

149. E. C. Sherbrooke, N. M. Patrikalakis, and E. Brisson, *An algorithm for the medial axis transform of 3D polyhedral solids.* Visualization and Computer Graphics, IEEE Transactions on, 1996. 2(1): p. 44-61.

150. J. C. Slater, *Quantum theory of molecules and solids*. Vol. 1. 1963: McGraw-Hill New York.

151. E. Yablonovitch, T. Gmitter, and K. Leung, *Photonic band structure: The face-centered-cubic case employing nonspherical atoms.* Physical Review Letters, 1991. 67(17): p. 2295.

152. J. Milnor. *Hilbert's problem 18: On crystallographic groups, fundamental domains, and on sphere packing*. in *Proc. Sympos. Pure Math*. 1976.

153. K. E. Brassel and D. Reif, *A procedure to generate Thiessen polygons.* Geographical Analysis, 1979. 11(3): p. 289-303.

154. F. R. Fiedler, *Simple, practical method for determining station weights using Thiessen polygons and isohyetal maps.* Journal of Hydrologic engineering, 2003. 8(4): p. 219-221.

155. G. L. Dirichlet, *Über die Reduction der positiven quadratischen Formen mit drei unbestimmten ganzen Zahlen.* Journal Fur Die Reine Und Angewandte Mathematik, 1850. 40: p. 209-227.

156. Hibbett, Karlsson, and Sorensen, *ABAQUS/standard: User's Manual*. Vol. 1. 2001: Hibbitt, Karlsson & Sorensen.

157. N. Hansen, *Polycrystalline strengthening.* Metallurgical Transactions A, 1985. 16(12): p. 2167-2190.

158. W. G. Cochran, *Errors of measurement in statistics.* Technometrics, 1968. 10(4): p. 637-666.

159. N. C. Barford, *Experimental measurements: precision, error and truth.* Chichester: Wiley, 1985, 2nd ed., 1985.

160. O. Diard, S. Leclercq, G. Rousselier, and G. Cailletaud, *Evaluation of finite element based analysis of 3D multicrystalline aggregates plasticity: Application to crystal plasticity model identification and the study of stress and strain fields near grain boundaries.* International Journal Of Plasticity, 2005. 21(4): p. 691-722.

161. Z. Fan, Y. Wu, X. Zhao, and Y. Lu, *Simulation of polycrystalline structure with Voronoi diagram in Laguerre geometry based on random closed packing of spheres.* Computational Materials Science, 2004. 29(3): p. 301-308.

162. I. Simonovski and L. Cizelj, *Automatic parallel generation of finite element meshes for complex spatial structures.* Computational Materials Science, 2011. 50(5): p. 1606-1618.

List of Publications during PhD Course

1. **Z. Fang**, Z. Y. Jiang, D. B. Wei and X. H. Liu: "Study of springback in micro V-bending with consideration of grain heterogeneity", *International Journal of Advanced Manufacturing Technology*, 2015, 78, pp. 1075-1085.

2. **Z. Fang**, Z. Y. Jiang, X. G. Wang, C. L. Zhou, D. B. Wei and X. H. Liu: "Grain size effect of thickness/average grain size on mechanical behaviour, fracture mechanism and constitutive model for phosphor bronze foil", *International Journal of Advanced Manufacturing Technology.* (DOI: 10.1007/s00170-015-6928-2, accepted on Feb 20, 2015).

3. **Z. Fang**, H. N. Lu, D. B. Wei, Z. Y. Jiang, X. M. Zhao, X. M. Zhang and D. Wu: "Numerical study on springback with size effect in micro V-bending", 11th International Conference on Technology of Plasticity, Nagoya, Japan. *Procedia Engineering*, 2014, 81, pp. 1011-1016.

4. **Z. Fang**, Z. Y. Jiang and D. B. Wei: "Modelling of grained heterogeneity with voronoi tessellation in microforming process", 1st Australasian Conference on Computational Mechanics, Sydney, Australia. *Applied Mechanics and Materials*, 2014, 553, pp. 66-70.

5. **Z. Fang**, Z. Y. Jiang, X. G. Wang, C. L. Zhou, X. M. Zhao, X. M. Zhang and D. Wu: "Grain size effect on texture evolution of annealed and micro V-bended phosphor bronze foil", *Metallurgical and Materials Transactions B.* (Submitted, E-TP-15-512-B)